

1998

Stability of quark-antiquark models of mesons: A study on the validity of the spectator, Dirac, and Salpeter equations

Michael Uzzo

College of William & Mary - Arts & Sciences

Follow this and additional works at: <https://scholarworks.wm.edu/etd>



Part of the [Physics Commons](#)

Recommended Citation

Uzzo, Michael, "Stability of quark-antiquark models of mesons: A study on the validity of the spectator, Dirac, and Salpeter equations" (1998). *Dissertations, Theses, and Masters Projects*. Paper 1539623942. <https://dx.doi.org/doi:10.21220/s2-jkcm-a386>

This Dissertation is brought to you for free and open access by the Theses, Dissertations, & Master Projects at W&M ScholarWorks. It has been accepted for inclusion in Dissertations, Theses, and Masters Projects by an authorized administrator of W&M ScholarWorks. For more information, please contact scholarworks@wm.edu.

INFORMATION TO USERS

This manuscript has been reproduced from the microfilm master. UMI films the text directly from the original or copy submitted. Thus, some thesis and dissertation copies are in typewriter face, while others may be from any type of computer printer.

The quality of this reproduction is dependent upon the quality of the copy submitted. Broken or indistinct print, colored or poor quality illustrations and photographs, print bleedthrough, substandard margins, and improper alignment can adversely affect reproduction.

In the unlikely event that the author did not send UMI a complete manuscript and there are missing pages, these will be noted. Also, if unauthorized copyright material had to be removed, a note will indicate the deletion.

Oversize materials (e.g., maps, drawings, charts) are reproduced by sectioning the original, beginning at the upper left-hand corner and continuing from left to right in equal sections with small overlaps. Each original is also photographed in one exposure and is included in reduced form at the back of the book.

Photographs included in the original manuscript have been reproduced xerographically in this copy. Higher quality 6" x 9" black and white photographic prints are available for any photographs or illustrations appearing in this copy for an additional charge. Contact UMI directly to order.

UMI[®]

Bell & Howell Information and Learning
300 North Zeeb Road, Ann Arbor, MI 48106-1346 USA
800-521-0600

STABILITY OF QUARK-ANTIQUARK MODELS OF
MESONS

A Study on the Validity of the Spectator, Dirac, and Salpeter Equations

A Dissertation

Presented to

The Faculty of the Department of Physics
The College of William and Mary in Virginia

In Partial Fulfillment
Of the Requirements for the Degree of
Doctor of Philosophy

by
Michael Uzzo

1998

UMI Number: 9936908

UMI Microform 9936908
Copyright 1999, by UMI Company. All rights reserved.


This microform edition is protected against unauthorized
copying under Title 17, United States Code.

UMI
300 North Zeeb Road
Ann Arbor, MI 48103

APPROVAL SHEET

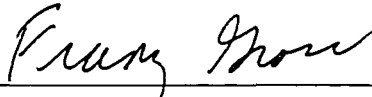
This dissertation is submitted in partial fulfillment of
the requirements for the degree of

Doctor of Philosophy

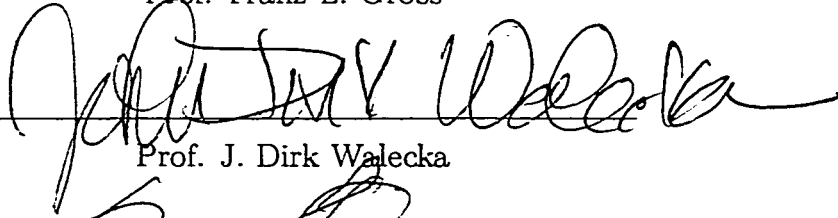


Michael Uzzo

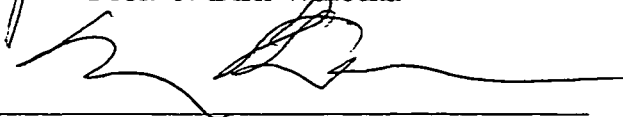
Approved, September 1998



Prof. Franz L. Gross



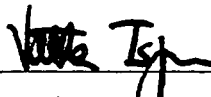
Prof. J. Dirk Walecka



Prof. Marc Sher



Prof. Keith Griffioen



Prof. Nathan Isgur

Thomas Jefferson National Accelerator Facility

I want to thank all of the people who helped me through the years, too numerous to be listed here but you know who you are. I should single out a few in particular. For starters my parents who were there from the very beginning and without whom none of this would be possible. Also Kelly Herbst, in whom I found the sister I never had. Finally Echo Simmons, the latest addition to my life and who means so very much to me. All my love.

TABLE OF CONTENTS

ACKNOWLEDGEMENTS	vii
LIST OF TABLES	vii
LIST OF FIGURES	xi
NOTATIONS AND CONVENTIONS	xx
ABSTRACT	xx
1 Introduction	2
1.1 Mesons and their quark structure	2
1.2 Definition of Stability	10
1.3 The Stability Conditions	15
1.4 Summary and Outline	19
2 The Dirac Equation	21

2.1	Derivation	21
2.2	The Equations	29
2.3	Stability Results	33
3	Single Channel Spectator Equation	40
3.1	Derivation	41
3.2	The Equations	50
3.3	Stability Results	52
4	The Salpeter Equation	75
4.1	Derivation	76
4.2	The Equations	77
4.3	Stability Analysis	78
5	Theoretical Analysis	95
5.1	Derivation of the general equations	96
5.2	Theoretical Analysis of the Dirac Equation	97
5.3	Theoretical Analysis of the 1CS Equation	102
6	Conclusions	114
A	Derivation of the Form of the Negative Energy Dirac Spinor	121
B	Spectator Equation in the Limit when $m_1 \rightarrow \infty$	123

C Definition of the Spline Function	126
D Momentum Space Wave Function Structures	132
REFERENCES	138
VITA	141

ACKNOWLEDGEMENTS

The author wishes to thank Prof. Franz Gross for all of the help he gave over the years, and especially for his contributions to the theoretical analysis technique. Many thanks to the faculty at the Physics Department of the College of William and Mary, especially to the members of his committee, which include Prof. J. D. Walecka, Prof. M. Sher, Prof. Keith Griffioen, and Nathan Isgur. Finally, the author expresses his gratitude to his friends and family for all their support.

LIST OF TABLES

2.1	Helicity spinors	22
2.2	First four positive and negative Dirac energy levels for $y=0.0$, 0.4, and 0.6 with spline ranks of 20, 16, and 12. The energies are in GeV. The bold face numbers are unstable states with energies <i>greater</i> than the stable ground state, as discussed in the text.	35
3.1	Θ_1 Term Identities for scalar and time-like vector	44
3.2	Θ_2 Term Identities for scalar and time-like vector	44
3.3	Results for $\chi^{\lambda_1 T} \sigma_i \chi^{\lambda_1'} \chi^{\lambda_2 T} \sigma_i \chi^{\lambda_2}$ where $\lambda_1 = \lambda_2$ and $\lambda_1' = \lambda_2'$	46
3.4	First four positive and negative 1CS $\kappa=5.0$, and 10.0 binding energy levels for $y=0.0$, and 0.4 with Spline ranks of 20, and 12. (Energy in GeV)	54

3.5	First four positive and negative 1CS $\kappa=1.0$ binding energy levels for $y=0.0$, and 0.4 with Spline ranks of 24, 20, 16, and 12. (Energy in GeV)	61
3.6	First four positive and negative binding energy levels for $y=0.4$ $\kappa=1.0, 2.0, 5.0$, and 10.0 with Spline ranks of 20, and 24 of the 1CS γ^μ systems (Energy in GeV).	66
4.1	First four bound state mass levels squared of the Salpeter Equation for $y=0.0$, and 0.4 with various Spline ranks. (Energy in GeV)	79
4.2	First Six bound state mass levels of the Salpeter Equation for $y=0.0$ with $m=0.85$ GeV and various Spline ranks. (Energy in GeV)	84
4.3	First Six bound state mass levels of the Salpeter Equation for $y=0.0$ with $m=1.625$ GeV and various Spline ranks. (Energy in GeV)	90
5.1	Comparison of the exact and estimated solutions for the Dirac and 1CS equations. All energies are in GeV, and the symbol - indicates that there is no stable solution.	106

6.1	Stability Results for scalar versus time-like vector mixed Lorentz structures (the table lists the region of stability or the first of the four tests that the system fails).	115
6.2	Stability Results for scalar versus full four vector mixed Lorentz structures (the table lists the region of stability or the first of the four tests that the system fails).	116

LIST OF FIGURES

1.1	Energy is applied to quark-antiquark bound state system (a), until pair production is achieved resulting in two new mesons (b).	8
1.2	Example of electroweak decay of the ρ^+ meson.	11
1.3	Example of strong decay of the ρ^+ meson.	11
1.4	Sketch of the solution to the Dirac equation for the scalar case, where $V_s > 0$ and $V_v = 0$	13
1.5	Sketch of the solution to the Dirac equation for the vector case, where $V_v > 0$ and $V_s = 0$	13
2.1	Dirac positive ground state solutions for three values of the vector strength y : $y = 0.0$, $E_1=0.976$ GeV (circles and squares); $y = 0.4$, $E_1=1.028$ GeV (solid and long dashed lines); and for $y = 0.6$, $E_1=1.065$ GeV (heavy short dashed and dotted lines).	37

2.2	Dirac positive first excited state solutions for $y = 0.0$, $E_2 = 1.394$ GeV (circles and squares), for $y = 0.4$, $E_2=1.456$ GeV (solid and long dashed lines), and for $y = 0.6$, $E_2=1.496$ GeV (heavy short dashed and dotted lines).	38
2.3	Dirac negative ground state solutions for $y = 0.0$, $E_{-1} = -1.249$ GeV (circles and squares), for $y = 0.4$, $E_{-1}=-0.660$ GeV (solid and long dashed lines), and for $y = 0.6$, $E_{-1} = 2.028$ GeV (heavy short dashed and dotted lines).	39
3.1	Feynman diagram for the meson bound state vertex function. The kernel, or potential, is denoted by V	43
3.2	This figure shows the position of the four poles associated with the four propagators G_i^p in the bound state equations.	47
3.3	Positive ground state solutions for the quasirelativistic 1CS equation with a pure scalar interaction. The solid and long dashed lines are for $\kappa=5.0$, $E_1=0.940$ GeV; the heavy short dashed and dotted lines are for $\kappa=10.0$, $E_1=0.964$ GeV. The scalar ground state Dirac solution for $E_1 = 0.976$ GeV is shown for comparison (circles and squares).	55

- 3.4 Positive first excited state solutions labeled as in the previous figure. Here the $\kappa = 5.0$ solution has an energy of $E_2 = 1.443$ GeV and the $\kappa = 10.0$ solution an energy of $E_2 = 1.435$ GeV compared to the Dirac energy of $E_2 = 1.394$ GeV. 56
- 3.5 Negative ground state solutions labeled as in the previous figure. Here the $\kappa = 5.0$ solution has an energy of $E_{-1} = -0.936$ GeV and the $\kappa = 10.0$ solution an energy of $E_{-1} = -1.091$ GeV compared to the Dirac energy of $E_{-1} = -1.249$ GeV. . 57
- 3.6 Positive ground state solutions of the quasirelativistic 1CS equation with a mixed scalar and vector interaction ($y = 0.40$) for two mass ratios κ . The solid and long dashed lines are for $\kappa = 5.0$, $E_1 = 0.992$ GeV, and the heavy short dashed and dotted lines are for $\kappa = 10.0$, $E_1 = 1.013$ GeV. The circles and squares show the solution for the Dirac equation with $E_1 = 1.028$ GeV. 59
- 3.7 Negative ground state solutions of the quasirelativistic 1CS equation for $y = 0.40$ labeled as in previous figure. Here $\kappa = 5.0$, $E_{-1} = -0.548$ GeV and $\kappa = 10.0$, $E_{-1} = -0.619$ GeV. The comparison Dirac level has energy $E_{-1} = 0.660$ GeV. . 60

- 3.8 Positive ground state solutions for the quasirelativistic 1CS equation with a pure scalar interaction. The solid and long dashed lines are for $\kappa=1.0$, $E_1=0.745$ GeV; the heavy short dashed and dotted lines are for $\kappa=2.0$, $E_1=0.857$ GeV. The scalar ground state Dirac solution for $E_1 = 0.976$ GeV is shown for comparison (circles and squares). 63
- 3.9 Negative ground state solutions labeled as in previous figure. Here the $\kappa = 1.0$ solution has an energy of $E_{-1} = -0.330$ GeV and the $\kappa = 2.0$ solution an energy of $E_{-1} = -0.607$ GeV compared to the Dirac energy of $E_{-1} = -1.249$ GeV. 64
- 3.10 Positive ground state solutions for the quasirelativistic 1CS equation with a four vector strength of $\gamma=0.4$. For $\kappa=5.0$ the energy is $E_1=0.992$ GeV with the circles and squares used. The solid and long dashed lines are for $\kappa=2.0$, $E_1=0.0.918$ GeV; the heavy short dashed and dotted lines are for $\kappa=1.0$, $E_1=0.828$ GeV. 67
- 3.11 Positive second excited states here are labeled as in the previous figure. The $\kappa = 5.0$ solution has an energy of $E_3=1.973$ GeV and the $\kappa = 2.0$ solution an energy of $E_3=2.055$ GeV. For the equal mass system the level is $E_3=2.071$ GeV. 68

- 3.12 Negative ground state solutions for the quasirelativistic 1CS equation with a four vector stength of $y=0.4$. For $\kappa=5.0$ the energy is $E_{-1}=-0.599$ GeV where the solid and long dashed lines are are used. The heavy short dashed and dotted lines are for $\kappa=2.0$, $E_{-1}=-0.480$ GeV. The Dirac system used as a comparison state is represented by circles and squares with $E_{-1}=-0.660$ GeV. 70
- 3.13 Negative second excited states here are labeled as in the previous figure. The $\kappa = 5.0$ solution has an energy of $E_{-3}=-0.774$ GeV and the $\kappa = 2.0$ solution an energy of $E_{-3}=-0.480$ GeV. For the Dirac system $E_{-3}=-0.879$ GeV. 71
- 3.14 Negative ground state solutions for the quasirelativistic 1CS equation with a four vector stength of $y=0.4$. For $\kappa=1.0$ the energy is $E_{-1}=-0.318$ GeV for both a spline rank of 30 (circles and squares) and 20 (solid and long dashed lines). 73
- 3.15 Negative second excited state solutions for the quasirelativistic 1CS equation with a four vector stength of $y=0.4$. For $\kappa=1.0$ the energy is $E_{-3}=-0.324$ GeV for both a spline rank of 30 (circles and squares) and 20 (solid and long dashed lines). 74

4.1	Positive and negative ground state solutions for the $y = 0.4$ quasirelativistic equal mass Salpeter equation, $\mu_1=1.157$ GeV (solid and long dashed lines) and $\mu_{-1}=-1.157$ GeV (heavy short dashed and dotted lines). The positive ground state Dirac solutions for $y=0.4$, $E_1=1.028$ GeV (circles and squares) are shown for comparison.	81
4.2	The positive second excited state solutions for the $y=0.4$ equal mass Salpeter equation, $\mu_3 = 2.094$ GeV (solid and long dashed lines) are compared to the second positive excited state Dirac solution for $y = 0.4$, $E_3=1.772$ GeV (circles and squares). . .	82
4.3	Positive second excited state solutions for the Salpeter equation for a variety of scalar/vector mixings: pure vector $y=1.0$, $\mu_3=2.565$ GeV (circles and squares); $y=0.6$, $\mu_3=2.284$ GeV (solid and long dashed lines); and $y=0.4$ $\mu_3=2.094$ GeV (heavy short dashed and dotted lines).	83
4.4	Positive ground state pure scalar solutions for the Salpeter equation $\mu_1=2.185$ GeV spline rank of 20 (circles and squares) and spline rank of 30 (solid and long dashed lines).	86

4.5	Positive fourth excited state pure scalar solutions for the Salpeter equation $\mu_5=3.354$ GeV spline rank of 20 (circles and squares) and spline rank of 30 $\mu_5=3.347$ GeV (solid and long dashed lines).	87
4.6	Positive fifth excited state pure scalar solutions for the Salpeter equation $\mu_6=3.482$ spline rank of 20 (circles and squares) and spline rank of 30 $\mu_6=3.375$ GeV (solid and long dashed lines).	88
4.7	Positive second excited state, $\gamma^\mu y=0.4$, solutions for the Salpeter equation $\mu_3=4.448$ GeV spline rank of 20 (circles and squares) and spline rank of 30 (solid and long dashed lines).	92
4.8	Positive third excited state, $\gamma^\mu y=0.4$, solutions for the Salpeter equation $\mu_4=4.508$ GeV with a spline rank of 30 (solid and heavy long dashed lines).	93
4.9	Salpeter equation, $\gamma^\mu y=0.4$, third excited state $\mu_4=4.686$ spline rank of 20 (circles and squares) and fourth excited state with a spline rank of 30 $\mu_5=4.687$ GeV (solid and long dashed lines).	94
5.1	The Dirac energy $E = E_B$ as a function of the variational parameter γ for different mass ratios $y = 0$ (solid line), $y = 0.4$ (dot-dashed), $y = 0.6$ (dashed), and $y = 1.0$ (dotted).	101

5.2	The trial wave functions $f(x)$ and $g(x)$ as a function of $x = \gamma r$. The different tails are for the cases $\omega/\gamma = 0.1$ (biggest tail), 0.5, and 2.0 (smallest tail), as discussed in the text.	104
5.3	Energies $E = E_B$ as a function of the variational parameter γ for the Dirac equation (solid line) and the 1CS equation with $m_1 = 10m_2$ (dashed line). In both cases, $y = 0$	109
5.4	The 1CS energy $E = E_B$ as a function of the variational pa- rameter γ for different mass ratios $\kappa = m_1/m_2 = 10$ (solid line), $\kappa = 5$ (dot-dashed), $\kappa = 2$ (dashed), and $\kappa = 1$ (dot- ted). In all cases, $y = 0$	110
5.5	The 1CS energy $E = E_B$ as a function of the variational pa- rameter γ for different mixing ratios $y = 0$ (solid line), $y = 0.4$ (dot-dashed), $y = 0.6$ (dashed), and $y = 1.0$ (dotted). In all cases $m_1/m_2 = 10$	112
5.6	The 1CS energy $E = E_B$ as a function of the variational pa- rameter γ for different mixing ratios $y = 0$ (solid line), $y = 0.4$ (dot-dashed), $y = 0.6$ (dashed), and $y = 1.0$ (dotted). In all cases $m_1/m_2 = 1$	113
C.1	Spline Rank 4 Curves (Index 1 Solid, 2 Long Dash, 3 Short Dash, and 4 Dot).	130

C.2	Spline Rank 4 Curves (Index 1 Solid, 2 Long Dash, 3 Short Dash, and 4 Dot) with Momentum Argument.	131
D.1	Non-Relativistic linear potential ground state wave functions, Airy solution $E_1=6.483$ GeV (Solid Line), Spline Rank 20 $E_1=6.485$ GeV (Circle), Spline Rank 16 $E_1=6.486$ (Square).	135
D.2	Non-Relativistic linear potential first excited state wave functions, Airy solution $E_2=11.337$ GeV (Solid Line), Spline Rank 20 $E_2=11.356$ GeV (Circle), Spline Rank 16 $E_2=11.355$ (Square).	136
D.3	Non-Relativistic linear potential second excited state wave functions, Airy solution $E_3=15.309$ GeV (Solid Line), Spline Rank 20 $E_3=15.464$ GeV (Circle), Spline Rank 16 $E_3=15.341$ (Square).	137

NOTATIONS AND CONVENTIONS

At this time it is appropriate to introduce some of the conventions used throughout this dissertation. Any vector variables written in **bold face** are three-vectors, while those in plain text are four-vectors. The mass of the light antiquark is set to 0.325 GeV, the rest mass of the up quark, while the mass of the quark can vary from 0.325 GeV to infinity. This was done to facilitate comparisons between systems. The usual convention that repeated indices are summed over will be used here. All energy values are in units of GeV. The figures presented here have a set of two wave functions for each individual system. The captions declare what the energy level of each state is and how each of the two wave functions of that state are represented. The first identification always represents the ψ_{1a} wave function. The second representation of the set is for the ψ_{1b} for the Dirac and one-channel spectator, or ψ_{2a} for the Salpeter systems.

ABSTRACT

Mesons are made of quark-antiquark pairs held together by the strong force. The one channel spectator, Dirac, and Salpeter equations can each be used to model this pairing. We look at cases where the relativistic kernel of these equations corresponds to a linear combination of scalar exchange and vector exchange. The vector exchange will be either the time-like component or the full four vector. The systems covered here are referred to as quasirelativistic, which means retardation, regularization, and form factors are not included. Since the model used in this paper describes mesons which cannot decay physically, the equations must describe stable states. We find that this requirement is not always satisfied, and give a complete discussion of the conditions under which the various equations give unphysical, unstable solutions.

STABILITY OF QUARK-ANTIQUARK MODELS OF
MESONS

A Study on the Validity of the Spectator, Dirac, and Salpeter Equations

Chapter 1

Introduction

1.1 Mesons and their quark structure

In the simplest models, mesons are bound states of a valence quark-antiquark pair confined by the strong force. Even for such a simple case, a covariant model is needed when the mesons are composed of light quarks with high momentum components. However, covariant models require knowledge of the Lorentz structure of the confining interaction, and it turns out that some choices of Lorentz structure for some equations will produce mesons which decay. When no mechanism for decay has been included in the model, which will be the situation for the cases discussed in this paper, this is a sign that the solutions are unstable due to mathematical inconsistency. For this reason

such a case will be rejected. In this research we studied confining potentials with scalar and either time-like or four vector exchanges, and found that the stability of such interactions depends on the kind of relativistic equation used for the description of the interaction.

Our knowledge of mesons in both experiment and theory have grown greatly since the concept was first developed by Yukawa in 1935 [1]. This first theory on mesons was developed as a means to explain the properties of nuclear forces. The concept was inspired by the model for the Coulomb force acting between two charged particles. The nucleon constantly emits particles with a finite rest mass, which are now referred to as pions. However, the production of these pions alters the rest mass of the nucleon which is a violation of the mass-energy conservation law. The way around this dilemma is supplied by the Heisenberg uncertainty principle. The pion in question can only exist for a short period of time before being absorbed by the nucleon. Such a pion is referred to as a virtual particle.

Suppose that two nucleons are close enough so that the virtual pion can travel the distance between them. There will then be a transfer of momentum carried by the pion from the parent nucleon to the second. This results in the same effect as a force acting between the two nucleons. When Yukawa developed his theory, mesons had yet to be detected. However, by observing

the range of the nuclear force phenomena he was able to determine the pion rest mass.

The experimental confirmation of the existence of pions as real particles would have to wait until 1947 [2]. Lattes, Occhialini, and Powell discovered that an abundant particle in cosmic rays, the muon or μ , is actually a decay product of the pion [3]. They also confirmed that the pion, or π meson, does interact with nucleons through the strong force.

It did not take long for the number of new mesons detected to grow tremendously. A new unifying principle had to exist to explain all of these different yet similar particles. Perhaps some underlying structure would enable the mesons to be broken down into a grouping not unlike the periodic table for grouping atoms. The most popular explanation is the theory of quarks. By this theory all particles can be divided into three groups: gauge bosons, leptons, and hadrons. Gauge bosons are the particles which convey the fundamental forces, such as the photon. Leptons include the electron, muon, and tau along with each of their neutrinos, like the electron neutrino. These six fundamental particles each have their own antiparticle. Leptons do not interact via the strong force, but do experience the electroweak force. Hadrons on the other hand are not elementary particles. They are composed of constituent particles called quarks. Hadrons are then divided into two

families, baryons and mesons. Baryons, which include protons and neutrons, are made up of a triplet of quarks or antiquarks. These particles have half-integral spin. Mesons are made out of a quark-antiquark pair and have integer spin.

This is the proper time to review some of the unique properties of quarks and their bound state systems. Quarks have spin $\frac{1}{2}$ with the fractional charges $\pm\frac{2}{3}$ and $\pm\frac{1}{3}$. The six flavors of quarks are up, down, charmed, strange, top, and bottom along with their six antiquark counterparts. The exact properties of quarks can be found in most current textbooks, such as Ref. [4]. The fact that they possess non-integer charges, a phenomenon not observed in nature, is not a problem since an isolated quark cannot occur. The reason for this will be covered shortly.

The triplet of quarks for the baryon and the quark-antiquark pair of the meson are referred to as valence quarks. These quarks determine the properties, such as spin and charge, of the bound state particle. The particle of force which binds the quarks together is the gluon, which has spin 1, and no charge or mass. In nature, the picture of these bound states is not this simple. In addition to the valence quarks there is also a sea of virtual quark-antiquark pairs and gluons. To make matters more complex, gluons can interact with one another to produce glueballs. The existence of this sea

of virtual quarks and glue interactions will be ignored in this research. The systems studied here will also be isolated from the outside environment.

There is another feature of the quark model which must be addressed. Consider the Δ^{++} baryon which is composed of three up quarks in identical states. The resulting system is a symmetric state. From Fermi statistics we know that the bound state must instead be antisymmetric. The solution to this dilemma is provided by QCD in the new property of color. There are three colors, which are sometimes called red, green, and blue, along with their anti-colors. Of course the term color does not refer to any form of pigmentation. Each of the three up quarks has one of these colors with no duplications. The resulting combination of all three colors is referred to as a white or color neutral bound state. When this principle of quantum number is applied, the system gains a new antisymmetric property. This results in the bound state system being antisymmetric. This new color property therefore provides the satisfaction of Fermi statistics.

When the system is an anti-baryon, then the three anti-colors would be utilized. For mesons the quark has one color and the antiquark has the corresponding anti-color, thus producing a neutral color bound state. The gluons must also have color in order to convey the strong force which keeps not only the quarks bound together, but the nucleons as well. For gluons

however, the property is a bicolor in which the particle has one color and a different anti-color. An example is a gluon possessing color $G\bar{R}$, or green and anti-red.

A method of numerically solving QCD is lattice gauge theory. In fact, from such numerical simulations the force between quarks was determined to be produced by a linear potential. However, lattice techniques require a great deal of computer power to accomplish their predictions. This in turn has limited their applications.

It is believed that an isolated quark can not exist, which is also due to the linear confining potential. The $q\bar{q}$ pair of a meson may be forced apart by dumping energy into the system. The farther apart a quark and antiquark become the stronger the confinement. When energy of at least twice the rest mass of a quark has been applied to the bound state the quark-antiquark pair splits. However, the energy applied to the system causes a new $q\bar{q}$ pair to be produced. The result is the production of two separate mesons from the original, as illustrated in Fig. 1.1.

The currently accepted potential of QCD, the one gluon exchange plus linear confinement, has been utilized in several studies such as Ref. [5]. Such studies have shown very encouraging results for the quark model in predicting such hadron properties as the mass spectra. In our research the one

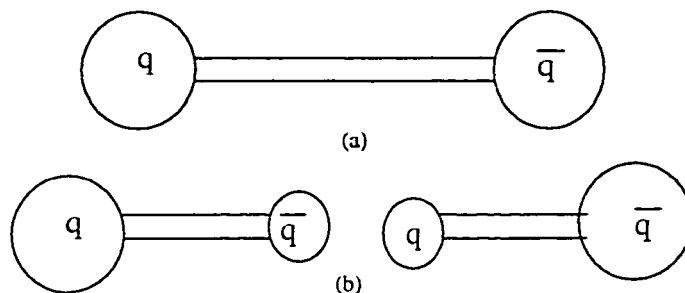


Figure 1.1: Energy is applied to quark-antiquark bound state system (a), until pair production is achieved resulting in two new mesons (b).

gluon exchange component has been dropped from the potential in order to simplify the models. However, the same stability criteria presented here can be applied to any form of the potential so long as the linear confinement is present.

This is not the first time that the stability of covariant models of confinement has been addressed. Several papers have been written on this topic, some with contradictory conclusions. Two examples which illustrate this are papers titled *An exact argument against an effective vector exchange for the confining quark-antiquark potential* [6], and *Evidence against a scalar confining potential in QCD* [7]. If both papers are correct, this would indicate that, at best, the Lorentz structure for the potential is more complex than a simple scalar or vector exchange.

Our research into the question of stability was motivated by a previous paper on the subject [8]. In this paper Parramore and Piekarewicz based their stability condition on whether the eigenvalues were real, and then confirmed the results based on the wave function structures. They found that the Salpeter equation was stable when the vector strength $y \geq 0.5$ regardless of the quark masses. The basis functions used to model their solutions were non-relativistic harmonic oscillators.

A second group, Ref. [9], also found the Salpeter equation with a scalar Lorentz structure to be unstable. They too cite the existence of imaginary eigenvalues as proof of their conclusions. In addition, they also point out that the time-like vector confinement has several problems of its own, including the fact that its one body limit is unstable. To solve their numerical systems Wallace and his group utilized cubic spline functions.

However, a third group found that the Salpeter equation was stable with a pure scalar system for a large quark mass and a weak linear confinement coefficient [10]. All other time-like vector strengths are also stable so long as the appropriate quark masses are used. Münz and his colleagues solved their numerical systems using the variational principle based on Laguerre polynomials. In the paper they identify two criteria for physically acceptable solutions. First, the norm of the solution cannot be zero, which automatically

implies that the bound state mass M is real. Second, the eigenvalue bound state mass and the norm have to be positive to fulfill the normalization condition $\langle \psi | \psi \rangle = (2\pi)^2 2M$. As a result of their second condition they are forced to neglect the negative mass eigenvalues.

1.2 Definition of Stability

Before beginning the discussion on the stability results we must first be clear about what kind of instabilities we are talking about. Mesons have a finite lifetime, and can decay either through the strong interaction or the electroweak interaction. For example, the ρ^+ can decay into a photon and π^+ through the electroweak interaction shown in Fig. 1.2. It can also decay into a π^+ and π^0 via the strong interaction, as shown in Fig. 1.3. According to QCD, mesons are made of a valence quark-antiquark pair and a sea of gluons and quark-antiquark pairs. The interactions occur via strong and electroweak forces. In the model considered here, the presence of the sea will be ignored and the system will be totally isolated, so no interactions with the external environment are possible. This means that we will ignore the electroweak interactions, which eliminates the first of the decay mechanisms described above from the model. Furthermore, we will not include any mechanism for quark-antiquark pair production, thus eliminating the strong decay modes

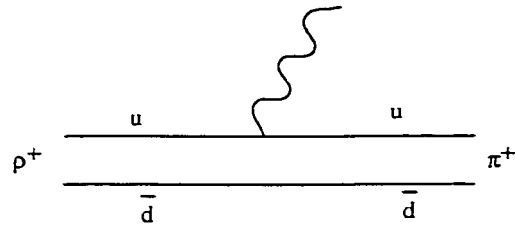


Figure 1.2: Example of electroweak decay of the ρ^+ meson.

as well. The result is a meson which cannot decay. This means that the presence of decay in the equations for the meson will imply a mathematical instability, and not the existence of some physical decay process.

The next question to be addressed is how to examine these equations of state for this mathematical instability. The easiest way to do this is by examining a well-known stable and unstable system, the simple Dirac system

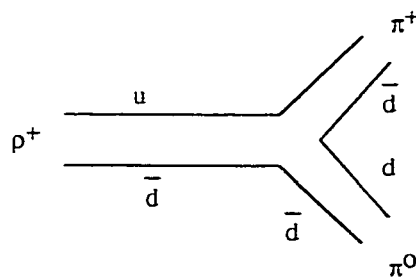


Figure 1.3: Example of strong decay of the ρ^+ meson.

for a scalar and vector linear potential. Let us start by considering the Dirac equation

$$E_B \gamma^0 \phi(r) = (m + V + \gamma \cdot \nabla) \phi(r) \quad (1.1)$$

where $V = V_s r + V_v r \gamma^0$, and the scalar and vector coefficients, V_s and V_v , are both constants. The solutions of this equation have both positive and negative binding energy eigenvalues E_B . If the system described by this equation could interact with the outside world (e.g. absorb or emit photons), the positive energy states could decay to negative energy states (unless all of the negative energy states were occupied and we were to invoke the Pauli principle, as in hole theory). However, we have assumed that there is no coupling to the outside world, and hence this equation will be assumed to describe a stable system as long as all the binding energy eigenvalues are real. The reason for this particular stability condition will be explained shortly, however it is **not** the only stability condition which must be satisfied. Even with all of these simplifications, it is well known that the Dirac equation does not give stable solutions for all forms of the potential, and as an introduction to the analysis methods used in this research, we review this result now.

The nature of the solutions to the Dirac equation can be studied by looking at the expectation value of $U = m + V$. The form of this expectation

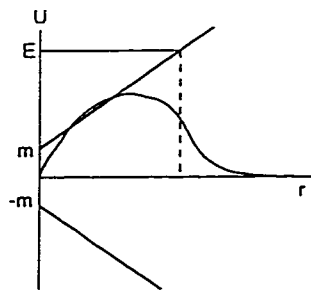


Figure 1.4: Sketch of the solution to the Dirac equation for the scalar case, where $V_s > 0$ and $V_v = 0$.

value, which describes how the wave function behaves, is

$$\langle U \rangle_{\pm} = \pm(m + V_s r) + V_v r, \quad (1.2)$$

where the upper sign is for the positive energy states, described by u -type positive energy spinors, and the lower is for the negative energy states, described

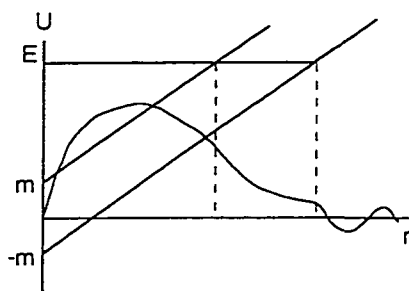


Figure 1.5: Sketch of the solution to the Dirac equation for the vector case, where $V_v > 0$ and $V_s = 0$.

by v -type negative energy spinors, and $\langle U \rangle_+ = \bar{u}Uu$, and $\langle U \rangle_- = \bar{v}Uv$. The signs come from the matrix elements

$$\begin{aligned}\bar{u}u &= 1 &= -\bar{v}v \\ \bar{u}\gamma^0u &= 1 &= \bar{v}\gamma^0v,\end{aligned}\tag{1.3}$$

which hold when the total momentum $p = 0$. When Eq. (1.2) is sketched for pure scalar or vector cases, Fig. 1.4 and Fig. 1.5 are produced, respectively. The resulting wave functions for a particle with energy E are sketched on the figures, along with the form of $\langle U \rangle$ which produces it.

To understand these results, first neglect the coupling between positive and negative energy states. Then the positive energy states move under the influence of the potential $\langle U \rangle_+$ and the negative energy states under the influence of $\langle U \rangle_-$. For the scalar case, the choice $V_s > 0$ produces confinement for both positive and negative energy states. Coupling the two solutions does not change this picture significantly, and the exact solution is a total wave function which drops to zero at large distances. This means that both positive and negative energy solutions describe particles permanently confined around the point $r = 0$.

Next look at the vector case, and begin again by neglecting the coupling between the positive and negative energy states. In this case, however, either

the positive or negative energy state is always unconfined. For the example shown in Fig. 1.5, $V_v > 0$ and the positive energy states are confined and the negative energy states are not. Including coupling between the positive and negative energy states mixes the two states, and the wave function for the exact positive energy solution acquires a component with a “tail” which oscillates to infinity, signaling deconfinement. The effect of the coupling is to produce an effective potential composed of two regions separated by a finite potential barrier through which the quark can tunnel. Once it is free of the potential barrier it can propagate endlessly through space, thus becoming a free quark. In this case, the exact coupled solutions do not confine either the positive or negative energy states, and the bound state is unstable. This example, known as the Klein paradox [11], is one of the unphysical instabilities we are trying to avoid.

1.3 The Stability Conditions

Now that we have illustrated the stability and instability of the simple Dirac equation with a scalar and vector Lorentz structure respectively, we can make the connection to the first stability technique to be used in this paper. It was mentioned earlier that the binding energy must be real for the system to have a chance at being stable. This first stability test is based on a technique

used in a previous paper on this subject [8]. It utilizes the principle that the eigenstate wave function which describes a meson in momentum space, $\psi(\mathbf{p}, t)$, can be written as

$$\psi(\mathbf{p}, t) = \phi(\mathbf{p})e^{-iEt}, \quad (1.4)$$

where $E = \sqrt{\mu^2 + \mathbf{P}_B^2}$. To simplify the discussion the particle will be chosen to be at rest, $\mathbf{P}_B = 0$, and the bound state mass, μ , is just the binding energy E_B for the Dirac system. If the binding energy of the meson is complex, $E_B = E_0 \pm i\Gamma/2$, the absolute square of the meson wave function is

$$|\psi(p, t)|^2 = |\phi(p)|^2 e^{\pm\Gamma t}. \quad (1.5)$$

As time increases, this goes exponentially either to zero or to infinity, showing that the meson is unstable if its bound state mass is complex. This means that if the total energy of the meson (the bound state mass or binding energy depending on the equation used) is real then the time component of the system is stable.

The next three stability tests turn out to be even more critical than the first one. As in the previous example, where even after assuming the binding energy is real the vector case still turned out to be unstable, most of the cases examined pass the first but not the remaining tests. It turns out that

the three additional stability requirements are essential and must be satisfied for the system to be stable.

The three different relativistic equations will be solved numerically using spline functions to model the wave functions in momentum space. A description of the properties of the spline functions is given in Appendix C. The validity of using spline functions to model the solutions to these systems is shown in Appendix D. So long as enough spline functions are used to model the system, the lower eigenvalues will not vary much as the spline rank is changed for a stable system. This means that the lower positive and negative eigenvalues must agree for different spline ranks, which will be the second stability condition. If the eigenvalues vary with the spline rank, it is an indication that the system has a continuous spectrum of energies and is thus unstable.

It was found that for some systems the positive energy states were stable but the negative states were not. The unstable negative states were in fact completely isolated from the positive states. The only system that this feature was observed in was the one channel spectator, referred to as 1CS. The validity of utilizing a system where only the positive energy states are stable is still under investigation. Such a partially stable system may prove useful in cases where the negative energy states can be rejected for phenomenological

reasons. The third stability requirement is therefore introduced. For a system to be stable when the negative states are unstable, the positive ground state energy levels must always be greater than any negative state. It will be shown in the numerical analysis that the unstable negative states can possess positive eigenvalues which can grow with the spline rank until their value is greater than the positive ground state.

The final stability condition is that a system is stable only if it possesses the correct wave function structure for each specific state. When the state in question is among the most excited, there are not enough spline functions to define it, and therefore it can be discarded. The magnitude and the locations of the wave function nodes does not matter, however the basic structure and the number of nodes does. To determine the proper structure of the wave functions in question the scalar Dirac wave functions are utilized as a comparison since this has already been proven to be a stable system. As an additional check, Appendix D illustrates the momentum space wave functions for the one-dimensional *Schrödinger* equation. The position space solutions for this equation are Airy functions, and the resulting momentum space wave functions display the same characteristics expected for those particular energy levels. Only the positive energy states can be examined this

way, however, using the first three energy level wave functions as an example, one can easily predict the structure for all other positive states.

It will be shown that any stable system will fulfill all four conditions mentioned above.

1.4 Summary and Outline

For a system to be stable these four conditions must be met;

- (1) the binding energy, or the bound state mass for the 1CS and Salpeter equations, must be real;
- (2) the energy eigenvalues must be independent of the numerical approximations used to obtain them;
- (3) if there are any unphysical solutions they must be confined to an identifiable part of the spectrum which is clearly separated from the physical solutions; and
- (4) the resulting wave functions must have the correct structure.

In Chapter 2 the Dirac equation is derived, modified to be solved numerically utilizing spline functions, and the stability analysis conducted. These same three steps are repeated for the one channel spectator equation in Chap-

ter 3, and the Salpeter equation in Chapter 4. Then in Chapter 5 these three equations are studied using an approximation technique which gives insight into the origin of the instabilities. The estimated binding energies or bound state masses of stable states from this approximation technique are also provided with their exact numerical counterparts. Finally, the conclusions of this research are given in Chapter 6.

The derivation of the negative energy Dirac spinor is provided in Appendix A. The Dirac equation can be derived from the 1CS equation by taking the $m_1 \rightarrow \infty$ limit, which is presented in Appendix B. The defining equations and properties of the spline functions can be found in Appendix C. Appendix D confirms that spline functions are capable of correctly modeling the confining potential systems. It also demonstrates the structure a stable wave function must have for any positive energy level.

Chapter 2

The Dirac Equation

In this chapter the Dirac equation for an *antiquark* moving under the influence of a confining field generated by a fixed source with spin 1/2 is explored. This fixed source is a heavy quark, so the Dirac equation will model a $Q\bar{q}$ system, such as a D meson.

2.1 Derivation

In the usual applications the Dirac equation describes the motion of a *particle* under the influence of a potential generated by a spin zero source. It can be obtained by taking the $m_1 \rightarrow \infty$ limit of the relativistic two-body spectator equation which describes the motion of a spin 1/2 particle with mass m_2 and a spin zero particle with mass m_1 , where the heavy spin zero particle is

Table 2.1: Helicity spinors

external quarks	internal quarks
$\lambda_i = \frac{1}{2} \begin{pmatrix} 1 \\ 0 \end{pmatrix}$	$\lambda'_i = \frac{1}{2} \begin{pmatrix} \cos \frac{\theta}{2} \\ \sin \frac{\theta}{2} \end{pmatrix}$
$\lambda_i = -\frac{1}{2} \begin{pmatrix} 0 \\ 1 \end{pmatrix}$	$\lambda'_i = -\frac{1}{2} \begin{pmatrix} -\sin \frac{\theta}{2} \\ \cos \frac{\theta}{2} \end{pmatrix}$

restricted to its mass-shell. A discussion of how the Dirac equation emerges when $m_1 \rightarrow \infty$ is presented in Appendix B. Since the field is generated by a heavy quark (a spin 1/2 particle) the source of the confining potential has helicity $\pm \frac{1}{2}$. This helicity will affect the solutions. The only features of the heavy quark that can be seen by the antiquark are the strong force and the effect of the quark helicity.

We begin by defining the helicity form of the Dirac spinors, since all of the work will be done in helicity space. In spin space the u spinor, defined

in Ref. [13], is

$$u(\mathbf{p}, s_j) = (E_p + m)^{\frac{1}{2}} \begin{pmatrix} 1 \\ \frac{\boldsymbol{\sigma} \cdot \mathbf{p}}{E_p + m} \end{pmatrix} \chi^{s_j}; \quad (2.1)$$

which contains the vector operator $\boldsymbol{\sigma} \cdot \mathbf{p}$. In helicity space $\boldsymbol{\sigma} \cdot \mathbf{p} \chi^\lambda = 2\lambda|\mathbf{p}|\chi^\lambda$, giving an eigenvalue times the helicity spinor χ^λ . The u spinor in helicity space is therefore

$$u(\mathbf{p}, \lambda_j) = N_{p_j} \begin{pmatrix} 1 \\ 2\lambda_j \tilde{p}_j \end{pmatrix} \chi^{\lambda_j}, \quad (2.2)$$

where

$$N_{p_j} = (E_{p_j} + m_j)^{\frac{1}{2}} \quad \tilde{p}_j = \frac{|\mathbf{p}|}{N_{p_j}^2} \quad (2.3)$$

and the index j denotes a quark ($j = 1$) or antiquark ($j = 2$). The values of \tilde{p} range from 0 to 1. The helicity spinors are defined in Table 2.1 for cases when the momentum is along the z axis (external quarks), and when the momentum is in the xz plane at an angle θ with respect to the z axis. We will use a prime to distinguish the latter from the former. These definitions

are consistent with those used in Ref. [14]. The v spinor used in this paper,

$$v(-\mathbf{p}, \lambda_j) = N_{p_j} \begin{pmatrix} -2\lambda_j \tilde{p}_j \\ \\ \\ 1 \end{pmatrix} \chi^{\lambda_j}, \quad (2.4)$$

is derived in Appendix A. It is convenient to use the helicity representation because helicity is invariant under rotations, and because the vector operator $\sigma \cdot \mathbf{p}$ is replaced by scalar eigenvalues, thus simplifying the algebra.

The Dirac equation for a spin 1/2 source is

$$-i\gamma^0 \frac{\partial}{\partial t} \psi_{\lambda_1}(\mathbf{r}, t) = \sum_{\lambda'_1} [-i\gamma^j \frac{\partial}{\partial r^j} + m + V_{\lambda_1 \lambda'_1}(\mathbf{r})] \psi_{\lambda'_1}(\mathbf{r}, t) \quad (2.5)$$

where the λ_1 and λ'_1 are the helicities of the source, and $m_2 = m$, the mass of the lighter particle. Recalling that the time dependence of the antiquark eigenfunctions is $e^{iE_B t}$, and transforming the equation to momentum space yields

$$(-E_B \gamma^0 - \boldsymbol{\gamma} \cdot \mathbf{p} - m) \phi_{\lambda_1}(\mathbf{p}) = \sum_{\lambda'_1} \int \frac{d\mathbf{k}}{(2\pi)^3} V_{\lambda_1 \lambda'_1}(\mathbf{p} - \mathbf{k}) \phi_{\lambda'_1}(\mathbf{k}). \quad (2.6)$$

Using the notation $p'_B = (E_B, -\mathbf{p})$, we obtain

$$\begin{aligned} (\not{p}'_B + m) \phi_{\lambda_1}(\mathbf{p}) &= (\gamma^0 E_B + \mathbf{p} \cdot \boldsymbol{\gamma} + m) \phi_{\lambda_1}(\mathbf{p}) \\ &= - \sum_{\lambda'_1} \int \frac{d\mathbf{k}}{(2\pi)^3} V_{\lambda_1 \lambda'_1}(\mathbf{p} - \mathbf{k}) \phi_{\lambda'_1}(\mathbf{k}), \end{aligned} \quad (2.7)$$

where

$$V_{\lambda_1 \lambda'_1}(\mathbf{r}) = \begin{cases} \bar{V}(\mathbf{r}) \langle \lambda_1 | \lambda'_1(\theta) \rangle & \text{for a scalar vertex} \\ -\gamma^0 \bar{V}(\mathbf{r}) \langle \lambda_1 | \lambda'_1(\theta) \rangle & \text{for a vector vertex.} \end{cases} \quad (2.8)$$

It should be noted that for the Dirac equation the potential vertex with a four vector Lorentz structure is the same as the time-like case. Equation (2.8) displays the fact that the helicity dependence of the potential is due exclusively to the helicity dependence of the source, expressed through the matrix elements of the helicity spinors given in Table 2.1. These matrix elements are

$$\begin{aligned} \langle \frac{1}{2} | \frac{1}{2}(\theta) \rangle &= \langle -\frac{1}{2} | -\frac{1}{2}(\theta) \rangle = \cos^2 \frac{\theta}{2} \\ -\langle \frac{1}{2} | -\frac{1}{2}(\theta) \rangle &= \langle -\frac{1}{2} | \frac{1}{2}(\theta) \rangle = \sin^2 \frac{\theta}{2}. \end{aligned} \quad (2.9)$$

To reduce the equation, we first expand the wave function in terms of the u and v spinors

$$\phi_{\lambda_1}(\mathbf{p}) = \sum_{\lambda_2} \left\{ \phi_+^{\lambda_1 \lambda_2}(\mathbf{p}) u(\mathbf{p}, \lambda_2) + \phi_-^{\lambda_1 \lambda_2}(\mathbf{p}) v(-\mathbf{p}, \lambda_2) \right\}. \quad (2.10)$$

We will limit our discussion to the ground state of a spin zero system at rest, in which case the antiquark and the source of the potential (quark) are traveling in opposite directions with their spins also pointing in opposite directions. Hence their helicities must be equal, $\lambda_1 = \lambda_2$. Imposing this

restriction, Eq. (2.10) reduces to

$$\phi_{\lambda_1}(\mathbf{p}) = \psi_+^{\lambda_1} u(\mathbf{p}, \lambda_1) + \psi_-^{\lambda_1} v(-\mathbf{p}, \lambda_1), \quad (2.11)$$

where $\psi^{\lambda_1} = \phi^{\lambda_1 \lambda_1}$. Introducing the notation $p_B = (E_B, \mathbf{p})$, $p = (E_p, \mathbf{p})$, and $p' = (E_p, -\mathbf{p})$, and using the relations

$$(\not{p} - m)u(\mathbf{p}) = (\not{p}' + m)v(-\mathbf{p}) = 0, \quad (2.12)$$

gives

$$\begin{aligned} (\not{p}'_B + m)v(-\mathbf{p}) &= (E_B - E_p)\gamma^0 v(-\mathbf{p}) \\ (\not{p}'_B + m)u(\mathbf{p}) &= (E_B + E_p)\gamma^0 u(\mathbf{p}). \end{aligned} \quad (2.13)$$

Taking Eq. (2.11), inserting it into Eq. (2.7), and using Eq. (2.13) gives

$$\begin{aligned} &\psi_+^{\lambda_1} (E_B + E_p)\gamma^0 u(\mathbf{p}, \lambda_1) + \psi_-^{\lambda_1} (E_B - E_p)\gamma^0 v(-\mathbf{p}, \lambda_1) \\ &= - \sum_{\lambda'_1} \int \frac{d\mathbf{k}}{(2\pi)^3} V_{\lambda_1 \lambda'_1} [\psi_+^{\lambda'_1} u(\mathbf{k}, \lambda'_1) + \psi_-^{\lambda'_1} v(-\mathbf{k}, \lambda'_1)]. \end{aligned} \quad (2.14)$$

The ψ_+ and ψ_- components on the left side of Eq. (2.14) can be separated out by multiplying by \bar{u} and \bar{v} , and using the fact that

$$v^\dagger(-\mathbf{p}, \lambda_1)u(\mathbf{p}, \lambda_2) = u^\dagger(\mathbf{p}, \lambda_1)v(-\mathbf{p}, \lambda_2) = 0. \quad (2.15)$$

Using the notation

$$a_{\mp} = (1 \mp \tilde{p}\tilde{k}) \quad c_{\pm} = (\tilde{p} \pm \tilde{k}) \quad \int_{\mathbf{k}} = \int \frac{d\mathbf{k}}{(2\pi)^3}, \quad (2.16)$$

and substituting Eqns. (2.8) and (2.9), gives the following set of coupled equations:

$$\begin{aligned}
-2E_p(E_B + E_p)\psi_+^{\frac{1}{2}} &= \int_{\mathbf{k}} \bar{V} N_p N_k [a_{\mp} \cos^2(\theta/2)\psi_+^{\frac{1}{2}} + a_{\pm} \sin^2(\theta/2)\psi_+^{-\frac{1}{2}} \\
&\quad \mp c_{\pm} \cos^2(\theta/2)\psi_-^{\frac{1}{2}} \mp c_{\mp} \sin^2(\theta/2)\psi_-^{-\frac{1}{2}}] \\
-2E_p(E_B + E_p)\psi_+^{-\frac{1}{2}} &= \int_{\mathbf{k}} \bar{V} N_p N_k [a_{\pm} \sin^2(\theta/2)\psi_+^{\frac{1}{2}} + a_{\mp} \cos^2(\theta/2)\psi_+^{-\frac{1}{2}} \\
&\quad \pm c_{\mp} \sin^2(\theta/2)\psi_-^{\frac{1}{2}} \pm c_{\pm} \cos^2(\theta/2)\psi_-^{-\frac{1}{2}}] \\
-2E_p(E_B - E_p)\psi_-^{\frac{1}{2}} &= \int_{\mathbf{k}} \bar{V} N_p N_k [-c_{\pm} \cos^2(\theta/2)\psi_+^{\frac{1}{2}} - c_{\mp} \sin^2(\theta/2)\psi_+^{-\frac{1}{2}} \\
&\quad \mp a_{\mp} \cos^2(\theta/2)\psi_-^{\frac{1}{2}} \mp a_{\pm} \sin^2(\theta/2)\psi_-^{-\frac{1}{2}}] \\
-2E_p(E_B - E_p)\psi_-^{-\frac{1}{2}} &= \int_{\mathbf{k}} \bar{V} N_p N_k [c_{\mp} \sin^2(\theta/2)\psi_+^{\frac{1}{2}} + c_{\pm} \cos^2(\theta/2)\psi_+^{-\frac{1}{2}} \\
&\quad \mp a_{\pm} \sin^2(\theta/2)\psi_-^{\frac{1}{2}} \mp a_{\mp} \cos^2(\theta/2)\psi_-^{-\frac{1}{2}}], \quad (2.17)
\end{aligned}$$

where the upper sign refers to the scalar case and the lower one to the vector case. As will be discussed later in the paper, this Dirac equation is identical to the equation derived from the $m_1 \rightarrow \infty$ limit of the spectator equation (the details are given in Appendix B).

The spin zero components of the wave function can be separated from Eq. (2.17) by taking the combinations

$$\psi_+ = \frac{1}{\sqrt{2}}(\psi_+^{\frac{1}{2}} - \psi_+^{-\frac{1}{2}}) \quad \psi_- = \frac{1}{\sqrt{2}}(\psi_-^{\frac{1}{2}} + \psi_-^{-\frac{1}{2}}). \quad (2.18)$$

This gives:

$$\begin{aligned} -2E_p(E_B + E_p)\psi_+(p) &= \int_{\bar{k}} \bar{V} N_p N_k \{ [a_{\mp} \cos^2(\theta/2) - a_{\pm} \sin^2(\theta/2)] \psi_+(k) \\ &\quad \mp [c_{\pm} \cos^2(\theta/2) + c_{\mp} \sin^2(\theta/2)] \psi_-(k) \} \\ -2E_p(E_B - E_p)\psi_-(p) &= \int_{\bar{k}} \bar{V} N_p N_k \{ [-c_{\pm} \cos^2(\theta/2) + c_{\mp} \sin^2(\theta/2)] \psi_+(k) \\ &\quad \mp [a_{\mp} \cos^2(\theta/2) + a_{\pm} \sin^2(\theta/2)] \psi_-(k) \}. \end{aligned} \quad (2.19)$$

At this time it would be prudent to adjust Eq. (2.19) to facilitate the numerical solution derivation and the comparison to the 1CS and Salpeter equations. First, the wave functions will absorb a square root of the kinetic energy factor, $\sqrt{E_p}\psi(p) \rightarrow \psi(p)$. Second, using trigonometric relations the cosine and sine terms will be combined. Finally, the equations will be rearranged and the substitution $\psi_- \rightarrow \psi_{1a}$ and $\psi_+ \rightarrow \psi_{1b}$ made. The system then becomes

$$\begin{pmatrix} (E_B - E_p) \\ (E_B + E_p) \end{pmatrix} \begin{pmatrix} \psi_{1a}(p) \\ \psi_{1b}(p) \end{pmatrix} = - \int_{\bar{k}} \frac{\bar{V} N_p N_k}{2\sqrt{E_p E_k}} \begin{pmatrix} \mp 1 + \bar{p}\bar{k} \cos \theta & \mp \bar{k} - \bar{p} \cos \theta \\ \mp \bar{p} - \bar{k} \cos \theta & \mp \bar{p}\bar{k} + \cos \theta \end{pmatrix} \begin{pmatrix} \psi_{1a}(k) \\ \psi_{1b}(k) \end{pmatrix}. \quad (2.20)$$

2.2 The Equations

We are now ready to conduct the stability analysis of the Dirac Equation, utilizing the stability conditions outlined in the Introduction. The system described by Eq. (2.20) is for either a scalar or vector confining potential. In order to create a mixed state, one with a percentage of scalar versus vector structure, we introduce a quantity called the vector mixing factor, y . By taking a linear combination of the scalar component of Eq. (2.20), multiplied by the factor $(1 - y)$, and the vector component, multiplied by $-y$, we generate the mixed state sought. The minus sign for the vector term is due to the nature of the u and v spinors as outlined in Eq. (1.3). In the nonrelativistic limit, the Dirac equation reduces to a Schrödinger equation for the upper component, and we will choose the sign of our potential so that it confines the positive energy solution in the nonrelativistic limit. Hence, in order to obtain a nonrelativistic confining potential equal to σr , dependent on the mixing parameter y , the operator form \mathcal{O} of a mixed kernel must be

$$\mathcal{O} = (1 - y) 1 \otimes 1 - y \gamma^0 \otimes \gamma^0. \quad (2.21)$$

When the linear combination is constructed and the system is algebraically reduced it becomes

$$\begin{pmatrix} (E_B - E_p) \\ (E_B + E_p) \end{pmatrix} \begin{pmatrix} \psi_{1a}(p) \\ \psi_{1b}(p) \end{pmatrix} = - \int_{\bar{k}} \frac{\bar{V} N_p N_k}{2\sqrt{E_p E_k}} \begin{pmatrix} d_1 & d_2 \\ d_3 & d_4 \end{pmatrix} \begin{pmatrix} \psi_{1a}(k) \\ \psi_{1b}(k) \end{pmatrix}, \quad (2.22)$$

where $d_i = a_i + b_i \cos \theta$ and

$$\begin{aligned} a_1 &= -1 & b_1 &= (1 - 2y)\bar{k}\bar{p} \\ a_2 &= -\bar{k} & b_2 &= -(1 - 2y)\bar{p} \\ a_3 &= -\bar{p} & b_3 &= -(1 - 2y)\bar{k} \\ a_4 &= -\bar{k}\bar{p} & b_4 &= (1 - 2y) \end{aligned} \quad (2.23)$$

When $y = 0$ it is the pure scalar case, and $y = 1$ is the pure vector case.

There are still two more steps required before we can numerically solve this system. The first is the definition of the confining potential \bar{V} . Starting with a simple linear potential in position space [15],

$$V(r) = \sigma r = \lim_{\epsilon \rightarrow 0} \sigma r e^{-\epsilon r} = \lim_{\epsilon \rightarrow 0} \sigma \frac{d^2}{d\epsilon^2} \frac{e^{-\epsilon r}}{r}. \quad (2.24)$$

In momentum space this potential is

$$V(\mathbf{q}) = 8\pi\sigma \lim_{\epsilon \rightarrow 0} \left(-\frac{1}{(\mathbf{q}^2 + \epsilon^2)^2} + \frac{4\epsilon^2}{(\mathbf{q}^2 + \epsilon^2)^3} \right). \quad (2.25)$$

The limit can not be taken at this time for two reasons; the potential \mathbf{q}^{-4} is singular at $\mathbf{q} = 0$ and when Fourier transformed to position space the result is not the original linear potential. Instead, an alternative potential will be used which is finite for all momenta and reproduces the linear confining potential.

$$V(\mathbf{q}) = -\frac{8\pi\sigma}{\mathbf{q}^4} + 8\pi\sigma\delta^3(\mathbf{q}) \int \frac{d^3q'}{\mathbf{q}'^4} \quad (2.26)$$

where $\mathbf{q} = \mathbf{p} - \mathbf{k}$ and $\mathbf{q}' = \mathbf{p} - \mathbf{k}'$. $V(\mathbf{q})$ defined in Eq. (2.26) is then substituted for \bar{V} in Eq. (2.22). A more detailed explanation can be found in Ref. [15].

The system as it stands now is not a scalar eigensystem, it is still a function of the momentum variable p . This brings us to the second step which involves a substitution for the wave function ψ and the integration of p out of the system. As stated earlier we shall use splines to model the wave functions, defined in Appendix C,

$$\psi(p) = \sum_j \alpha_j \beta_j(p). \quad (2.27)$$

where α_j is the eigenvector and β_j is the spline function. Since this is a spherically symmetric potential the wave function depends only on the momentum magnitude p . Once Eq. (2.27) is substituted in for ψ_{1a} and ψ_{1b} , then

both sides of Eq. (2.22) are operated on by the integral operator

$$\int p^2 \beta_i(p) dp. \quad (2.28)$$

Once all of the algebra and angular integration is completed the system becomes a $2 \times SN$ by $2 \times SN$ eigensystem, where SN stands for the number of spline functions used to model the system. This eigensystem has the form

$$\int p^2 \beta_i(p) \beta_j(p) \begin{pmatrix} (E_B - E_p) \\ (E_B + E_p) \end{pmatrix} dp = \int dp dk \begin{pmatrix} \eta_{1lj} & \eta_{2lj} \\ \eta_{3lj} & \eta_{4lj} \end{pmatrix}, \quad (2.29)$$

where $\eta_{ilj} = PT_i(PT1_{ij} + PT2_{ij} + PT3_{ij})$. The rest of the identities are

$$e = p^2 + k^2$$

$$f = -2|p||k|$$

$$W_j = \frac{N_p N_k}{\sqrt{E_p E_k}} \beta_j(k)$$

$$W'_j = W_j(k = p)$$

$$a'_i = a_i(k = p)$$

$$b'_i = b_i(k = p)$$

$$PT_i = \beta_i(p) \frac{\sigma}{4\pi}$$

$$PT1_{ij} = 2f^2 \frac{W_j a_i - W'_j (a'_i + b'_i)}{e^2 - f^2}$$

$$\begin{aligned}
PT2'_{ij} &= -\frac{2feW_jb_i}{e^2 - f^2} \\
PT3'_{ij} &= W_jb_i \ln\left(\frac{e+f}{e-f}\right),
\end{aligned}
\tag{2.30}$$

with the primes representing the original function with $k = p$.

2.3 Stability Results

Finally, all of the pieces are in place. The system described by Eq. (2.29) and Eq. (2.30) can be solved numerically on a PC in a reasonable amount of time. The value for the antiquark mass will be set at $m=0.325$ GeV. The light antiquark mass will not change, even for the LCS cases, in order to maintain consistence between models. Rather than examine the Dirac system for many values of the vector strength, we shall look at a few important cases. The systems examined here will be $y=0.0$ (pure scalar), 0.4, 0.6, and 1.0 (pure vector) cases. The first four positive and negative binding energy levels for the $y=0.0$, 0.4, and 0.6 systems are given in Table 2.2 below with spline ranks of 20, 16, and 12. Only the first four positive and negative levels are listed but all are considered in the analysis.

It was found that the pure vector case had similiar properties as the $y=0.6$, which is why it was omitted here. The eigenvalues are all real, therefore they pass the first stability conditions. Out of the four cases the pure vector and

.

$y=0.6$ cases fail both the second and third conditions. This is due to the fact that the negative levels vary with the spline rank, and these states continue to increase with the spline rank until they surpass the positive levels. The reasons why the negative states eventually become greater than the positive eigenvalues, which are shown in bold face in Table 2.2, will be discussed in the chapter on the approximate theoretical solutions. This is enough to declare it an unstable system, but we will examine the wave functions anyway.

This leaves us with only stability condition four, the structure of the wave functions, to consider. As mentioned in the Notations and Conventions, for the figures the first wave function mentioned in each set of two represents ψ_{1a} , while the second is for ψ_{1b} . The positive ground state Fig. 2.1, and first excited state Fig. 2.2, in addition to the negative ground state Fig. 2.3 will be examined for $y = 0.0, 0.4$ and 0.6 . The pure scalar wave functions are used as our accepted structures since it has been well established that this state is stable. In fact, the structure of the wave functions in momentum space matches exactly to what one would expect the position space structure to be for corresponding levels. By comparing these three systems, as well as others not shown here, we come to the conclusion that the Dirac system is stable when the vector mixing is $y < 0.5$. While the positive levels have the correct structure, the negative unstable state of $y=0.6$ does not. It can therefore

Table 2.2: First four positive and negative Dirac energy levels for $y=0.0, 0.4,$ and 0.6 with spline ranks of 20, 16, and 12. The energies are in GeV. The bold face numbers are unstable states with energies *greater* than the stable ground state, as discussed in the text.

Level	$y = 0.0$			$y = 0.4$			$y = 0.6$		
	SN=20	SN=16	SN=12	SN=20	SN=16	SN=12	SN=20	SN=16	SN12
4	1.945	1.945	1.946	2.035	2.035	2.035	2.092	2.092	2.093
3	1.695	1.695	1.695	1.772	1.772	1.772	1.821	1.821	1.821
2	1.394	1.393	1.393	1.456	1.455	1.455	1.496	1.496	1.496
1	0.976	0.976	0.976	1.028	1.028	1.028	1.065	1.065	1.065
-1	-1.249	-1.249	-1.248	-0.660	-0.660	-0.660	2.028	1.576	1.120
-2	-1.575	-1.575	-1.574	-0.781	-0.781	-0.780	1.190	0.861	0.525
-3	-1.839	-1.839	-1.838	-0.879	-0.878	-0.879	0.899	0.590	0.278
-4	-2.067	-2.067	-2.078	-0.963	-0.963	-0.964	0.692	0.396	0.090

be concluded that the fourth stability condition largely reinforces the conclusions we have already drawn. however, it is less reliable than the other three. The stability of a *single* state cannot easily be determined by tracking (with changing spline number) its behavior. A reliable conclusion requires the examination of the entire spectrum, including the negative energy states, with particular attention to condition 3.

The positive ground states and first excited states have almost identical wave function structures. Although at first glance the pure scalar and $y = 0.4$ cases do not look similiar for the negative ground state, they are. The magnitude, value of the momentum at which the wave function drops to zero, and location of any nodes may vary from case to case. It is the number of nodes and basic structure which determines if the wave function represented is stable.

Another conclusion can be drawn from Fig. 2.3. The wave functions of the pure scalar system extend further into momentum space before dropping to zero than the $y = 0.4$ case. This means that in position space the opposite is true, the $y = 0.4$ system travels further from the origin than the $y = 0.0$ system. Thus, the pure scalar system is more tightly bound than when a vector strength of 0.4 is present.

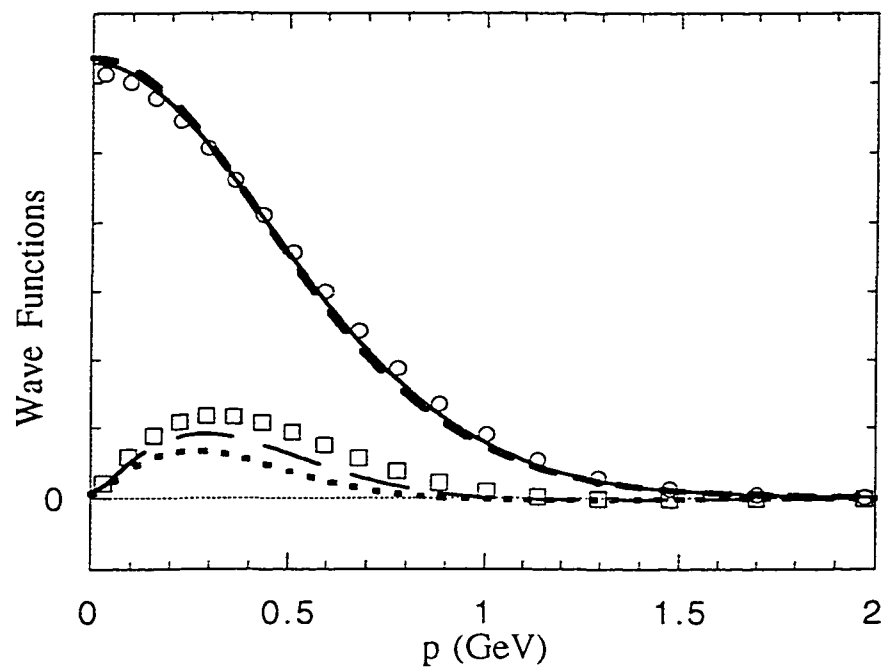


Figure 2.1: Dirac positive ground state solutions for three values of the vector strength y : $y = 0.0$, $E_1 = 0.976$ GeV (circles and squares); $y = 0.4$, $E_1 = 1.028$ GeV (solid and long dashed lines); and for $y = 0.6$, $E_1 = 1.065$ GeV (heavy short dashed and dotted lines).

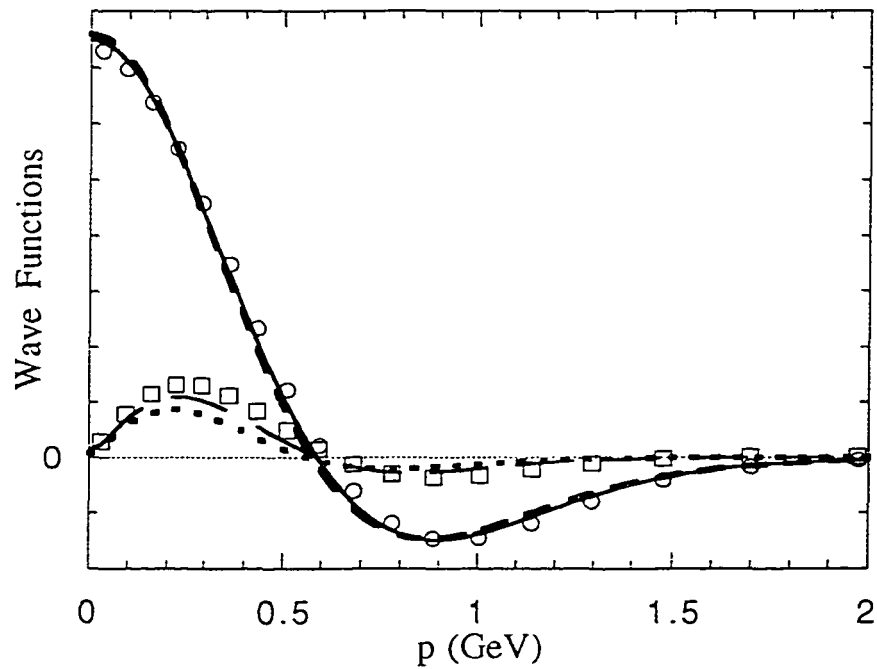


Figure 2.2: Dirac positive first excited state solutions for $y = 0.0$, $E_2 = 1.394$ GeV (circles and squares), for $y = 0.4$, $E_2 = 1.456$ GeV (solid and long dashed lines), and for $y = 0.6$, $E_2 = 1.496$ GeV (heavy short dashed and dotted lines).

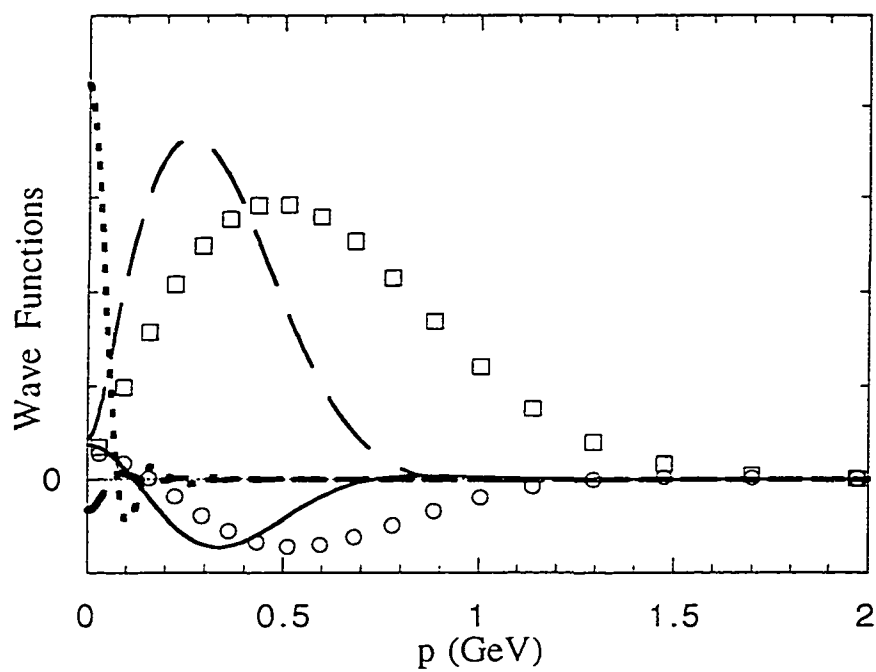


Figure 2.3: Dirac negative ground state solutions for $y = 0.0$, $E_{-1} = -1.249$ GeV (circles and squares), for $y = 0.4$, $E_{-1} = -0.660$ GeV (solid and long dashed lines), and for $y = 0.6$, $E_{-1} = 2.028$ GeV (heavy short dashed and dotted lines).

Chapter 3

Single Channel Spectator

Equation

In this chapter we examine the spectator equation with one channel defined by confining particle 1 to its positive energy mass shell, fixing the k_0 integration, and thus producing two coupled equations. The derivation of these equations utilizes the helicity spinors from the Dirac equation as well as many of the same concepts. In this research what will be referred to as a Quasi-relativistic system is examined. This means that the equation is relativistic except for the potential. The potential does not contain such features as form factors, a regularization term, or retardation. The stability of these equations is then determined and compared with the results found for the

Dirac equation. Examination of a fully relativistic system will be the subject of future research.

3.1 Derivation

The Feynman diagram for the bound state meson vertex is shown in Fig. 3.1. Particle 1 represents the quark, particle 2 the antiquark, and Θ is the potential vertex function. This vertex function can be one of two possible linear combinations. The first is a mixed Lorentz structure of a scalar and the time component of a four-vector, γ^0 . The second is the scalar and full four vector mixture, as shown below.

$$\mathcal{O} = (1 - y) 1 \otimes 1 - y \gamma^0 \otimes \gamma^0 \quad (3.1)$$

The full four vector is defined as

$$\gamma^\mu = (\gamma^0, \vec{\gamma}) \quad (3.2)$$

where

$$\gamma^i = \begin{pmatrix} 0 & \sigma_i \\ -\sigma_i & 0 \end{pmatrix}. \quad (3.3)$$

and σ_i is just the i^{th} Pauli matrix.

The kernel V represents the confining potential. The equations are derived in the center of mass rest frame, $P = (\mu, 0)$. Later, the quark will

be placed on shell, thus producing the single channel equation. The four momenta used in the diagram are

$$\begin{aligned}
p_1 &= p + \frac{1}{2}P & p_2 &= p - \frac{1}{2}P \\
k_1 &= k + \frac{1}{2}P & k_2 &= k - \frac{1}{2}P \\
p &= \frac{1}{2}(p_1 + p_2) & P &= p_1 - p_2.
\end{aligned} \tag{3.4}$$

The vector k is the average internal momentum, and vector p is the average external momenta of the quark-antiquark pair. With this notation, the Bethe-Salpeter equation [12] for the bound state vertex function for the meson is

$$\Gamma(p) = i \int \frac{d^4k}{(2\pi)^4} V \Theta \frac{m_1 + \not{k}_1}{m_1^2 - k_1^2} \Gamma(k) \frac{m_2 + \not{k}_2}{m_2^2 - k_2^2} \Theta. \tag{3.5}$$

Decomposing the propagators into u ($\rho = +1$) and v ($\rho = -1$) spin contributions [13],

$$\frac{(m_i + \not{k}_i)}{m_i^2 - k_i^2} = \frac{1}{(2E_{k_i})} \sum_{\lambda'} \left[\frac{u(\mathbf{k}, \lambda') \bar{u}(\mathbf{k}, \lambda')}{E_{k_i} - k_{i0} - i\epsilon} - \frac{v(-\mathbf{k}, \lambda') \bar{v}(-\mathbf{k}, \lambda')}{E_{k_i} + k_{i0} - i\epsilon} \right], \tag{3.6}$$

and operating on the left and right sides of Eq. (3.5) by u and v -spinors, so that all four possible combinations of spinors are present, gives the ρ -spin decomposition of the bound state vertex equation

$$\Gamma^{\rho_1 \rho_2}(p) = i \int \frac{d^4k}{(2\pi)^4 4E_{k_1} E_{k_2}} V \sum_{\rho'_1 \rho'_2} \sum_{\lambda'_1 \lambda'_2} \Theta_1^{\rho_1 \rho'_1} G_1^{\rho'_1} \Gamma^{\rho'_1 \rho'_2}(k) G_2^{\rho'_2} \Theta_2^{\rho'_2 \rho_2}. \tag{3.7}$$

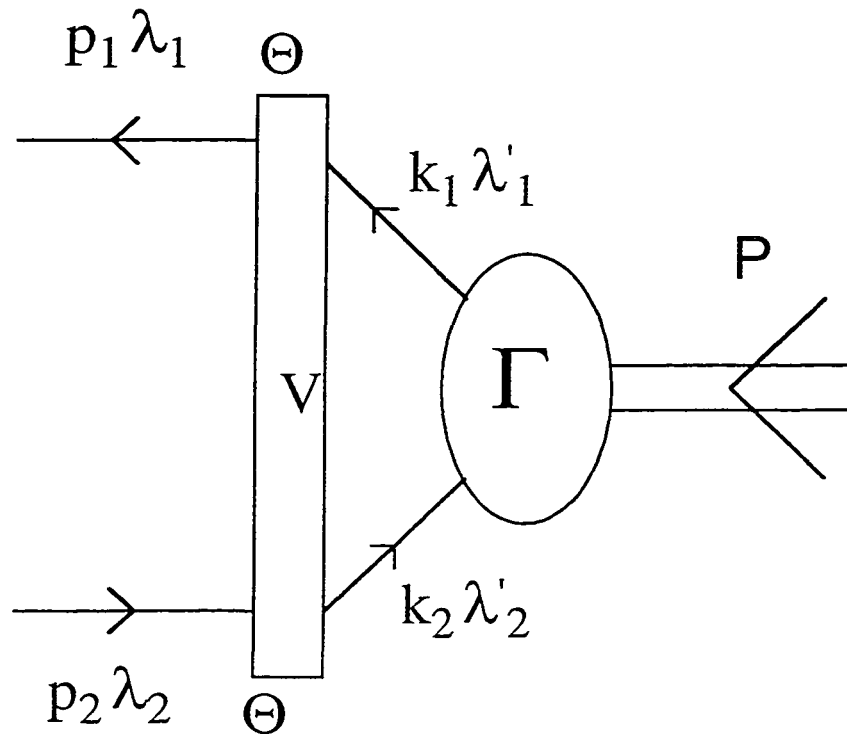


Figure 3.1: Feynman diagram for the meson bound state vertex function.

The kernel, or potential, is denoted by V .

The dependences of Θ and Γ on the helicities λ'_1 and λ'_2 in the equation above have been suppressed.

The terms Θ_i represent the potential vertex of particle i . They are constructed by combinations of u and v spinors, determined by the index ρ , operating on either side of the confining potential Lorentz structure. The identities of these Θ terms are derived, with the results shown in Table 3.1

and Table 3.2 when the vector component is time-like. The identities of the Cs and Sn terms are $\cos(\frac{1}{2}\theta)$ and $\sin(\frac{1}{2}\theta)$ respectively.

Table 3.1: Θ_1 Term Identities for scalar and time-like vector

	$\lambda_1 = \frac{1}{2}$	$\lambda_1 = \frac{1}{2}$	$\lambda_1 = -\frac{1}{2}$	$\lambda_1 = -\frac{1}{2}$
	$\lambda'_1 = \frac{1}{2}$	$\lambda'_1 = -\frac{1}{2}$	$\lambda'_1 = \frac{1}{2}$	$\lambda'_1 = -\frac{1}{2}$
Θ_1^{++}	$a_1^\mp Cs$	$-a_1^\pm Sn$	$a_1^\pm Sn$	$a_1^\mp Cs$
Θ_1^{+-}	$\mp c_1^\pm Cs$	$\pm c_1^\mp Sn$	$\pm c_1^\mp Sn$	$\pm c_1^\pm Cs$
Θ_1^{-+}	$-c_1^\pm Cs$	$c_1^\mp Sn$	$c_1^\mp Sn$	$c_1^\pm Cs$
Θ_1^{--}	$\mp a_1^\mp Cs$	$\pm a_1^\pm Sn$	$\mp a_1^\pm Sn$	$\mp a_1^\mp Cs$

Table 3.2: Θ_2 Term Identities for scalar and time-like vector

	$\lambda_2 = \frac{1}{2}$	$\lambda_2 = \frac{1}{2}$	$\lambda_2 = -\frac{1}{2}$	$\lambda_2 = -\frac{1}{2}$
	$\lambda'_2 = \frac{1}{2}$	$\lambda'_2 = -\frac{1}{2}$	$\lambda'_2 = \frac{1}{2}$	$\lambda'_2 = -\frac{1}{2}$
Θ_2^{++}	$a_2^\mp Cs$	$-a_2^\pm Sn$	$a_2^\pm Sn$	$a_2^\mp Cs$
Θ_2^{+-}	$-c_2^\pm Cs$	$c_2^\mp Sn$	$c_2^\mp Sn$	$c_2^\pm Cs$
Θ_2^{-+}	$\mp c_2^\pm Cs$	$\pm c_2^\mp Sn$	$\pm c_2^\mp Sn$	$\pm c_2^\pm Cs$
Θ_2^{--}	$\mp a_2^\mp Cs$	$\pm a_2^\pm Sn$	$\mp a_2^\pm Sn$	$\mp a_2^\mp Cs$

When the vector component is γ^μ the algebra is even more complex. The set of equations below is used to define the Θ terms with j defining particle 1 or 2, and i determining which three vector component is considered.

$$\begin{aligned}
\Theta_{ji}^{++} &= N_{p_j} N_{k_j} \chi^{\lambda_j T} \sigma_i \chi^{\lambda_j'} (2\lambda_j \tilde{p}_j + 2\lambda_j' \tilde{k}_j) \\
\Theta_{ji}^{+-} &= N_{p_j} N_{k_j} \chi^{\lambda_j T} \sigma_i \chi^{\lambda_j'} (1 - 4\lambda_j \tilde{p}_j \lambda_j' \tilde{k}_j) \\
\Theta_{ji}^{-+} &= N_{p_j} N_{k_j} \chi^{\lambda_j T} \sigma_i \chi^{\lambda_j'} (1 - 4\lambda_j \tilde{p}_j \lambda_j' \tilde{k}_j) \\
\Theta_{ji}^{--} &= -N_{p_j} N_{k_j} \chi^{\lambda_j T} \sigma_i \chi^{\lambda_j'} (2\lambda_j \tilde{p}_j + 2\lambda_j' \tilde{k}_j)
\end{aligned} \tag{3.8}$$

The equations above are set up for particle 1, for particle 2 the primed indices of χ must be unprimed and vice-versa. To condense the information on the results from the Pauli-spinor matrix products to one table a particular property will be utilized. Later in this section it will be shown that only when $\lambda_1 = \lambda_2$ and $\lambda_1' = \lambda_2'$ does a nonzero result for the bound state vertex functions occur. When this principle is applied to the expression $\chi^{\lambda_1 T} \sigma_i \chi^{\lambda_1'} \chi^{\lambda_2 T} \sigma_i \chi^{\lambda_2}$ the result is Table 3.3. These results are used in conjunction with Eq. (3.8) in order to produce the gamma functions as was done in the γ^0 case.

The components G_j^ρ are the ρ -spin propagators

$$G_1^\pm = \frac{\pm 1}{E_{k_1} \mp (k_0 + \frac{1}{2}\mu) - i\epsilon}$$

Table 3.3: Results for $\chi^{\lambda_1 T} \sigma_i \chi^{\lambda_1'} \chi^{\lambda_2 T} \sigma_i \chi^{\lambda_2}$ where $\lambda_1 = \lambda_2$ and $\lambda_1' = \lambda_2'$

	σ_1	σ_1	σ_2	σ_2	σ_3	σ_3
	$\lambda = \frac{1}{2}$	$\lambda = -\frac{1}{2}$	$\lambda = \frac{1}{2}$	$\lambda = -\frac{1}{2}$	$\lambda = \frac{1}{2}$	$\lambda = -\frac{1}{2}$
$\lambda' = \frac{1}{2}$	Sn^2	Cs^2	Sn^2	Cs^2	Cs^2	Sn^2
$\lambda' = -\frac{1}{2}$	Cs^2	Sn^2	Cs^2	Sn^2	Sn^2	Cs^2

$$G_2^\pm = \frac{\pm 1}{E_{k_1} \mp (k_0 - \frac{1}{2}\mu) - i\epsilon}. \quad (3.9)$$

The first ρ of each term in Eq. (3.7) tells which spinor appears to the left and the second indicates which is on the right. The location of the poles produced by G_j^\pm are shown in Fig. 3.2 and listed below.

$$\begin{aligned}
\text{pole 1} \quad & (G_1^+)^{-1} = E_{k_1} - (k_0 + \frac{1}{2}\mu) - i\epsilon = 0 & k_0 = E_{k_1} - \frac{1}{2}\mu - i\epsilon \\
\text{pole 3} \quad & (G_1^-)^{-1} = E_{k_1} + (k_0 + \frac{1}{2}\mu) - i\epsilon = 0 & k_0 = -E_{k_1} - \frac{1}{2}\mu + i\epsilon \\
\text{pole 2} \quad & (G_2^+)^{-1} = E_{k_2} - (k_0 - \frac{1}{2}\mu) - i\epsilon = 0 & k_0 = E_{k_2} + \frac{1}{2}\mu - i\epsilon \\
\text{pole 4} \quad & (G_2^-)^{-1} = E_{k_2} + (k_0 - \frac{1}{2}\mu) - i\epsilon = 0 & k_0 = -E_{k_2} + \frac{1}{2}\mu + i\epsilon
\end{aligned} \quad (3.10)$$

To place particle 1 on the positive energy mass shell, only the contribution from pole 1 is retained. This automatically fixes $\rho_1' = +$. To close the set of equations we also restrict the external particle to its mass shell, fixing $\rho_1 = +$. This gives

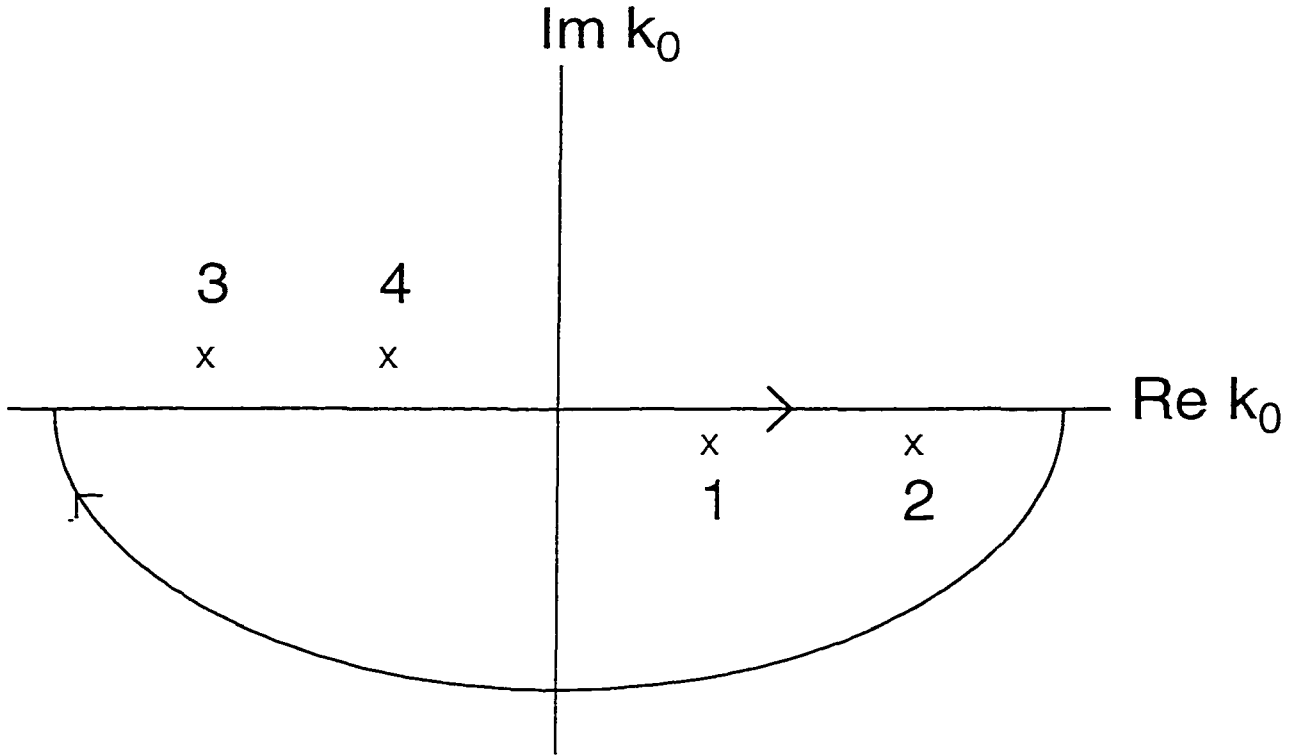


Figure 3.2: This figure shows the position of the four poles associated with the four propagators G_i^p in the bound state equations.

$$\Gamma_1^{+\rho_2}(p) = \int \frac{d^3 k}{(2\pi)^3} V'_{11} \sum_{\rho'_2} \sum_{\lambda'_1 \lambda'_2} \Theta_1^{++} \Gamma_1^{+\rho'_2} G_2^{\rho'_2} \Theta_2^{\rho'_2 p_2}. \quad (3.11)$$

where $V'_{11} = -V_{11}/(4E_{k_1} E_{k_2})$. The subscript 1 on V_{11} and Γ_1 indicates that the value at pole 1 has been substituted in for both k_0 and p_0 , and, since the quark (particle 1) is on its positive mass shell, it is described by its positive energy spinor only.

To further reduce Eq.(3.11) we will assume that the states are either pure scalar or pseudoscalar. The most general form for the bound state vertex function Γ in these two cases is

$$\Gamma_1 = a + b \left(\frac{m_2 - k_2}{2m_2} + \frac{m_1 - k_1}{2m_1} \right) + c \frac{(m_2 - k_2)(m_1 - k_1)}{4m_2m_1} \quad (3.12)$$

and

$$\Gamma_{\gamma^5} = a\gamma^5 + b \left(\gamma^5 \frac{m_2 - k_2}{2m_2} + \frac{m_1 - k_1}{2m_1} \gamma^5 \right) + c \frac{(m_2 - k_2)\gamma^5(m_1 - k_1)}{4m_2m_1}. \quad (3.13)$$

Using these forms we can show that for both the scalar and pseudoscalar cases, the only non zero helicity matrix elements occur when $\lambda_1 = \lambda_2$ for all possible $\Gamma^{\rho_1\rho_2}$. Furthermore, the only possible combination of helicity states with spin zero which are not identically zero are

$$\begin{aligned} \Gamma_1^{++} &= \frac{1}{\sqrt{2}} \left[\Gamma_{\frac{1}{2}\frac{1}{2}}^{++} + \Gamma_{-\frac{1}{2}-\frac{1}{2}}^{++} \right] & \Gamma_{\gamma^5}^{++} &= \frac{1}{\sqrt{2}} \left[\Gamma_{\frac{1}{2}\frac{1}{2}}^{++} - \Gamma_{-\frac{1}{2}-\frac{1}{2}}^{++} \right] \\ \Gamma_1^{+-} &= \frac{1}{\sqrt{2}} \left[\Gamma_{\frac{1}{2}\frac{1}{2}}^{+-} - \Gamma_{-\frac{1}{2}-\frac{1}{2}}^{+-} \right] & \Gamma_{\gamma^5}^{+-} &= \frac{1}{\sqrt{2}} \left[\Gamma_{\frac{1}{2}\frac{1}{2}}^{+-} + \Gamma_{-\frac{1}{2}-\frac{1}{2}}^{+-} \right]. \end{aligned} \quad (3.14)$$

In this work we shall restrict ourselves to the pseudoscalar bound state which means a pseudoscalar meson. The reason for this is consistency since the pseudoscalar 1CS system reduces to the s-state Dirac system in the $m_1 \rightarrow \infty$ limit as shown in Appendix B. The connection between the bound state vertex functions and the wave functions are the relations

$$\psi_{1a} = -\frac{\Gamma_1^{+-}}{E_{k_2} + E_{k_1} - \mu} \quad \psi_{1b} = \frac{\Gamma_1^{++}}{E_{k_2} - E_{k_1} + \mu}, \quad (3.15)$$

where μ is the mass eigenvalue of the meson. Bringing all of these elements together generates the single channel spectator equation

$$\begin{pmatrix} (\mu - E_{p_2} - E_{p_1})\psi_{1a}(p) \\ (\mu + E_{p_2} - E_{p_1})\psi_{1b}(p) \end{pmatrix} = \int_{\vec{k}} \bar{V}_{11} \begin{pmatrix} d_1 & d_2 \\ d_3 & d_4 \end{pmatrix} \begin{pmatrix} \psi_{1a}(k) \\ \psi_{1b}(k) \end{pmatrix}, \quad (3.16)$$

where the upper sign holds for scalar confinement and the lower for vector confinement, and

$$\begin{aligned} a_1 &= \mp Q & b_1 &= R \\ a_2 &= \mp T_2 & b_2 &= -S_2 \\ a_3 &= \mp S_2 & b_3 &= -T_2 \\ a_4 &= \mp R & b_4 &= Q \\ Q &= 1 + \bar{p}_1 \bar{p}_2 \bar{k}_1 \bar{k}_2 & R &= \bar{p}_1 \bar{k}_1 + \bar{p}_2 \bar{k}_2 \\ S_j &= \bar{p}_j - \bar{k}_1 \bar{k}_2 \bar{p}_{j'} & T_j &= \bar{k}_j - \bar{p}_1 \bar{p}_2 \bar{k}_{j'}, \end{aligned} \quad (3.17)$$

with $j' \neq j$ and

$$\bar{V}_{11} = V'_{11} N_{p_1} N_{p_2} N_{k_1} N_{k_2}. \quad (3.18)$$

When the full four vector Lorentz structure is used for the potential vertex the matrix elements for the vector components alone are

$$\begin{aligned} a_1 &= Q + 3W & b_1 &= R - X \\ a_2 &= T_2 - 3T_1 & b_2 &= S_1 - S_2 \\ a_3 &= S_2 - 3S_1 & b_3 &= T_1 - T_2 \\ a_4 &= R - 3X & b_4 &= Q + W. \end{aligned} \quad (3.19)$$

3.2 The Equations

Now that the general 1-channel spectator equation has been generated for a pseudoscalar bound state with either a scalar or vector potential interaction, we are ready to specify the potential. The potential used here should have the same properties as the one used in the Dirac system. However, there will be a slight difference between the potential used here and that of the Dirac system, Eq. (2.26). The delta term of the potential, required to eliminate the pole at $\mathbf{k} = \mathbf{p}$, possess an energy ratio of the on-shell-mass m_1

$$V(\mathbf{q}) = -\frac{8\pi\sigma}{\mathbf{q}^4} + E_{k_1} 8\pi\sigma\delta^3(\mathbf{q}) \int \frac{d^3q'}{E_{k'_1} \mathbf{q}'^4}. \quad (3.20)$$

The energy ratio is required because the quark was placed on its mass shell.

The identity of the wave function Eq. (2.27), and the integration operation Eq. (2.28) is then applied to Eq. (3.17) with the potential Eq. (3.20) substituted in. The two separate mixed states of vector and scalar Lorentz structure is utilized here. At this time the system could be listed, and in fact it would be a perfectly applicable matrix equation, however one more step remains. In order to directly compare to the Dirac system, the wave function for the ICS equation will be redefined. A factor of one over the square root of the energy of the antiquark will be absorbed into the wave functions on both sides of the equation, $\frac{1}{\sqrt{E_{k_2}}}\psi_{1a}(k) \rightarrow \psi_{1a}(k)$. This will

also facilitate the observation that the ICS equation reduces to the Dirac equation when $m_1 \rightarrow \infty$. The equation solved for by the computer after the angular integration is completed is

$$\int p^2 \beta_l(p) \beta_j(p) \begin{pmatrix} (\mu - E_{p_2} - E_{p_1}) \\ (\mu + E_{p_2} - E_{p_1}) \end{pmatrix} dp = \int dp dk \begin{pmatrix} \eta_{1lj} & \eta_{2lj} \\ \eta_{3lj} & \eta_{4lj} \end{pmatrix}, \quad (3.21)$$

where η_{ilj} , e , and f are the same as the Dirac case. The *primes* once again indicate the original identity with $|\mathbf{k}| = |\mathbf{p}|$. Let $N_p^2 = N_{p_1} N_{p_2}$, then the new terms needed to define Eq. (3.21) are

$$\begin{aligned} PT_l &= \frac{\sigma \beta_l(p)}{8\pi E_{k_1}} \\ PT_{1ij} &= \frac{2f^2 a_i \beta_j(k) N_p^2 N_k^2}{\sqrt{E_{p_2} E_{k_2}} (e^2 - f^2)} \\ PT_{2ij} &= -\frac{2f^2 N_{p_1}^2 N_{p_2}^2 \beta_j(p) (a'_i + b'_i)}{E_{p_2} (e^2 - f^2)} \\ PT_{3ij} &= \frac{b_i \beta_j(k) N_p^2 N_k^2}{\sqrt{E_{p_2} E_{k_2}}} \left(\frac{-2ef}{e^2 - f^2} + \ln \left(\frac{e+f}{e-f} \right) \right). \end{aligned} \quad (3.22)$$

When the linear combination of scalar and vector structures of Eq. (3.17) and Eq. (3.19) are taken we calculate the identities of d_i for the γ^0 , Eq. (3.23),

and γ^μ , Eq. (3.24) systems.

$$\begin{aligned}
a_1 &= -Q & b_1 &= (1 - 2y)R \\
a_2 &= -T_2 & b_2 &= -(1 - 2y)S_2 \\
a_3 &= -S_2 & b_3 &= -(1 - 2y)T_2 \\
a_4 &= -R & b_4 &= (1 - 2y)Q.
\end{aligned} \tag{3.23}$$

$$\begin{aligned}
a_1 &= -Q - 3yW & b_1 &= (1 - 2y)R + yX \\
a_2 &= -T_2 + 3yT_1 & b_2 &= -(1 - 2y)S_2 - yS_1 \\
a_3 &= -S_2 + 3S_1 & b_3 &= -(1 - 2y)T_2 - yT_1 \\
a_4 &= -R + 3yX & b_4 &= (1 - 2y)Q - yW.
\end{aligned} \tag{3.24}$$

This concludes the discussion on preparing the equations for the numerical analysis of stability. Next, the results of this examination are explored.

3.3 . Stability Results

3.3.1 1CS with scalar versus time-like vector structure

We begin the analysis with a system containing a mixed linear Lorentz structure of scalar versus time-like vector. As mentioned in the Dirac case the antiquark mass will be set at $m_2 = 0.325$ GeV and only the quark mass shall vary by a mass factor κ , $m_1 = \kappa m_2$. This is done to avoid unnecessary

complications when comparing results. Four mass ratios will be examined here, $\kappa = 1.0, 2.0, 5.0,$ and 10.0 . In order to make a direct comparison to the Dirac equation we note the approximate relation between the bound state mass and the binding energy below.

$$\mu \approx E_B + m_1 \quad (3.25)$$

This relation holds for when m_1 is large, such as $\kappa=10.0$ or even 5.0 . The eigenvalue spectra given in Tables 3.4 and 3.5 are the corresponding binding energies for those systems. Although it does not truly apply to the case when $\kappa=1.0$ it will be utilized anyway for consistency. This is not a problem since the 1CS equation is not designed for an equal mass system and was only included as a comparison with the other systems. When the bound state is made up of equal mass particles then the equation must be symmetrized in order to obey the Pauli principle. The system must also be symmetrized in order to insure charge conjugation invariance. For an equal mass system the Salpeter equation or the two channel spectator equation, not covered here [18], must be used.

All cases pass condition 1, however only systems with a vector strength of 0.0 and 0.4 pass condition 2. For expediency those cases which fail the first two stability conditions will not be listed in the following eigenvalue tables. First the five and ten-to-one mass ratios will be considered since it was found

Table 3.4: First four positive and negative 1CS $\kappa=5.0$, and 10.0 binding energy levels for $y=0.0$, and 0.4 with Spline ranks of 20, and 12. (Energy in GeV)

Level	$y = 0.0 \kappa = 5.0$		$y = 0.0 \kappa = 10.0$		$y = 0.4 \kappa = 5.0$		$y = 0.4 \kappa = 10.0$	
	SN=20	SN=12	SN=20	SN=12	SN=20	SN=12	SN=20	SN=12
4	2.109	2.113	2.073	2.078	2.225	2.227	2.165	2.168
3	1.808	1.808	1.783	1.783	1.898	1.899	1.858	1.858
2	1.443	1.443	1.435	1.435	1.509	1.509	1.495	1.494
1	0.940	0.939	0.964	0.964	0.992	0.992	1.013	1.013
-1	-0.936	-0.936	-1.091	-1.090	-0.548	-0.569	-0.619	-0.619
-2	-1.084	-1.084	-1.333	-1.332	-0.570	-0.607	-0.715	-0.715
-3	-1.173	-1.170	-1.511	-1.515	-0.600	-0.637	-0.786	-0.785
-4	-1.233	-1.259	-1.650	-1.642	-0.630	-0.675	-0.841	-0.848

that they were closely related to the Dirac systems. By examining Table 3.4 it can be seen that all four cases, $\kappa=5.0$ and 10.0 with $y=0.0$ and 0.4, all pass condition 3. So now we turn our attention to the structure of the individual wave functions.

In Fig. 3.3 through Fig. 3.5 the wave functions show that for a pure scalar Lorentz potential the structures of the 1CS models match those of the corre-

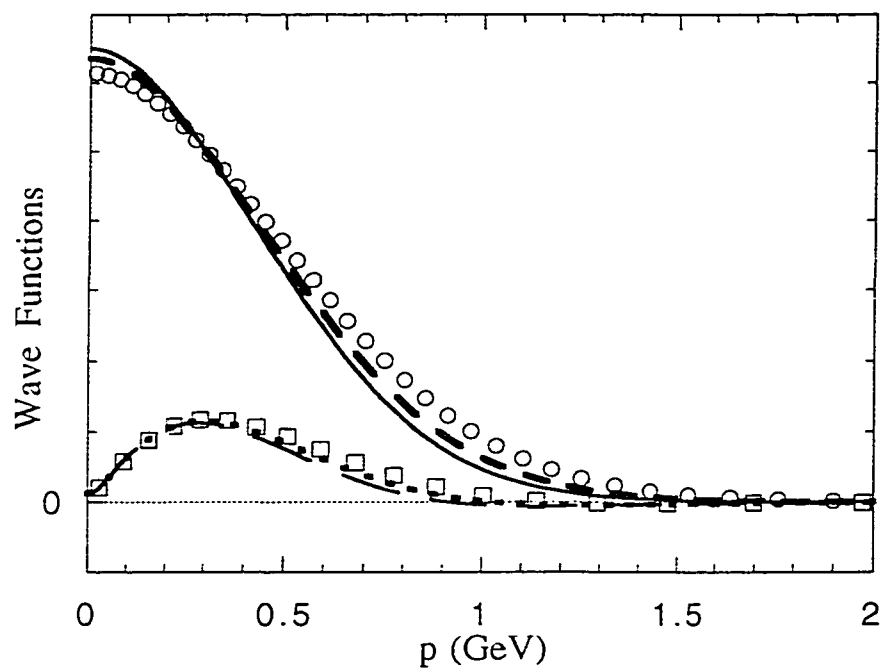


Figure 3.3: Positive ground state solutions for the quasirelativistic 1CS equation with a pure scalar interaction. The solid and long dashed lines are for $\kappa=5.0$, $E_1=0.940$ GeV; the heavy short dashed and dotted lines are for $\kappa=10.0$, $E_1=0.964$ GeV. The scalar ground state Dirac solution for $E_1 = 0.976$ GeV is shown for comparison (circles and squares).

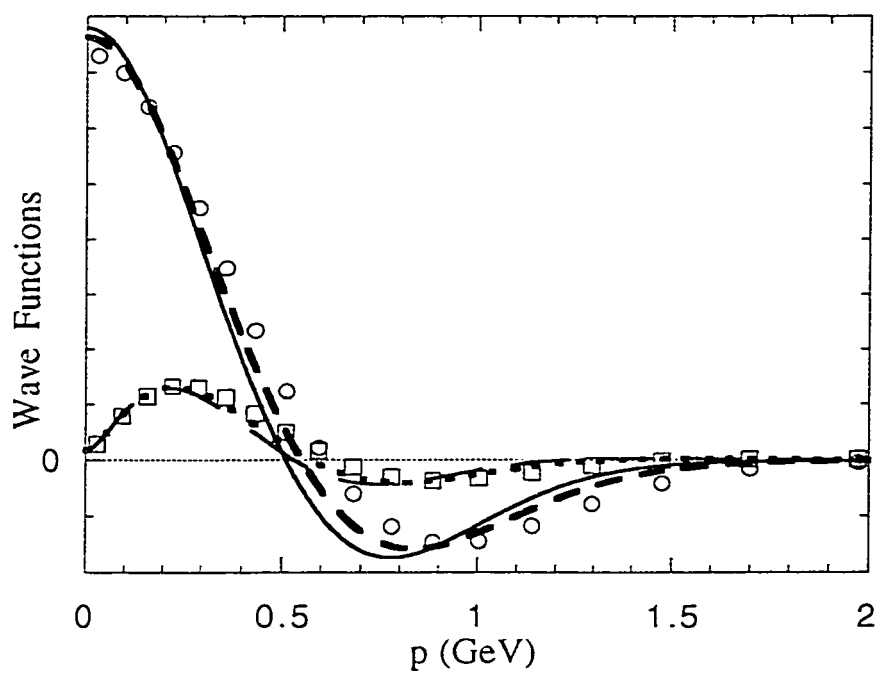


Figure 3.4: Positive first excited state solutions labeled as in the previous figure. Here the $\kappa = 5.0$ solution has an energy of $E_2 = 1.443$ GeV and the $\kappa = 10.0$ solution an energy of $E_2 = 1.435$ GeV compared to the Dirac energy of $E_2 = 1.394$ GeV.

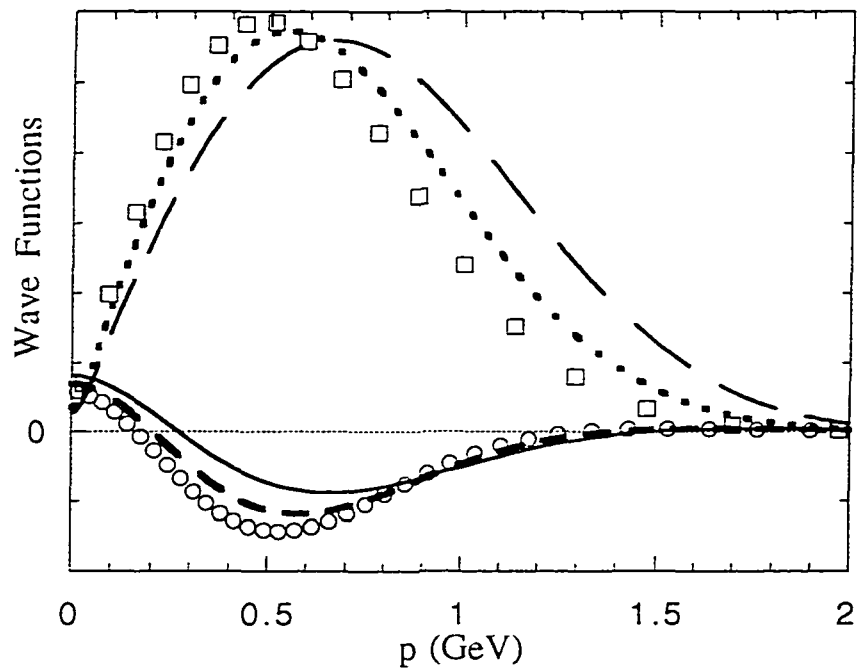


Figure 3.5: Negative ground state solutions labeled as in the previous figure. Here the $\kappa = 5.0$ solution has an energy of $E_{-1} = -0.936$ GeV and the $\kappa = 10.0$ solution an energy of $E_{-1} = -1.091$ GeV compared to the Dirac energy of $E_{-1} = -1.249$ GeV.

sponding Dirac systems. Therefore these two systems are completely stable, both positive and negative states. We can also observe how the 1CS binding energies approach the Dirac values as κ is increased in Table 3.4 and how the wave functions increasingly overlap those of the Dirac system. In addition, the negative ground states demonstrate a greater lack of overlapping structures than the two positive states do.

When the vector strength of $y = 0.4$ is examined in Fig. 3.6 and Fig. 3.7, a slightly different result is found. For $\kappa=10.0$ the system is once again totally stable, while for $\kappa=5.0$ only the positive states are stable. This causes some concern, although stability condition 3 is maintained the ramifications of this feature on the usefulness of this system are as of yet unclear.

The $\kappa = 2.0$ system will be skipped and the equal mass case will be examined now. It was found that the $\kappa = 2.0$ analysis finds the same results as the $\kappa = 1.0$. By examining Table 3.5 it can be seen that condition 3 is violated for $y=0.4$ as demonstrated by the negative state binding energy in bold face when the spline rank is 24. As a result, only the pure scalar systems for $\kappa=1.0$ and 2.0 remain.

The positive and negative ground states for $\kappa = 1.0$ and 2.0 are examined in Fig. 3.8 and Fig. 3.9. From these figures it can be determined that the positive states are stable while the negative ones are not. The conclusion

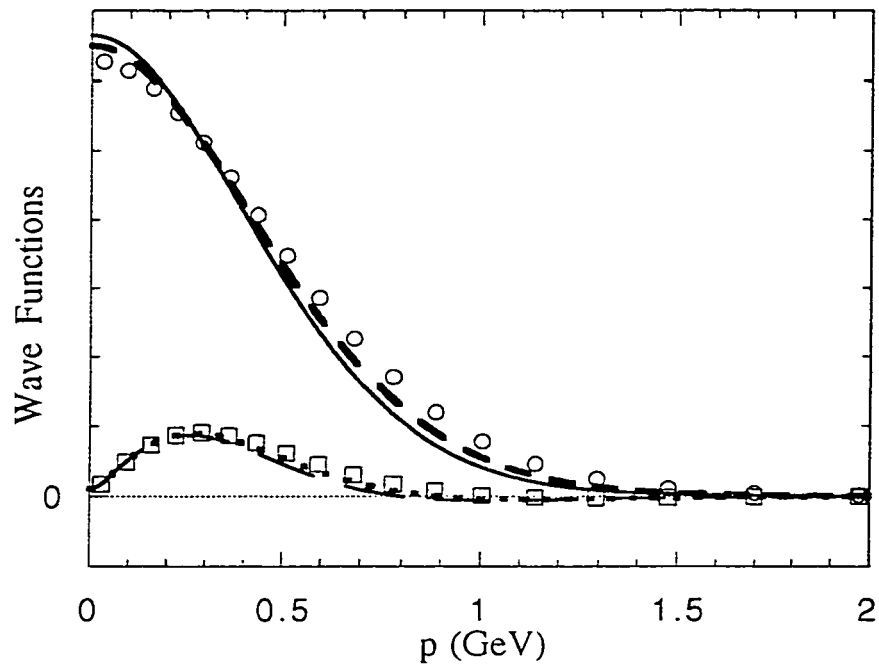


Figure 3.6: Positive ground state solutions of the quasirelativistic 1CS equation with a mixed scalar and vector interaction ($y = 0.40$) for two mass ratios κ . The solid and long dashed lines are for $\kappa = 5.0$, $E_1 = 0.992$ GeV, and the heavy short dashed and dotted lines are for $\kappa = 10.0$, $E_1 = 1.013$ GeV. The circles and squares show the solution for the Dirac equation with $E_1 = 1.028$ GeV.

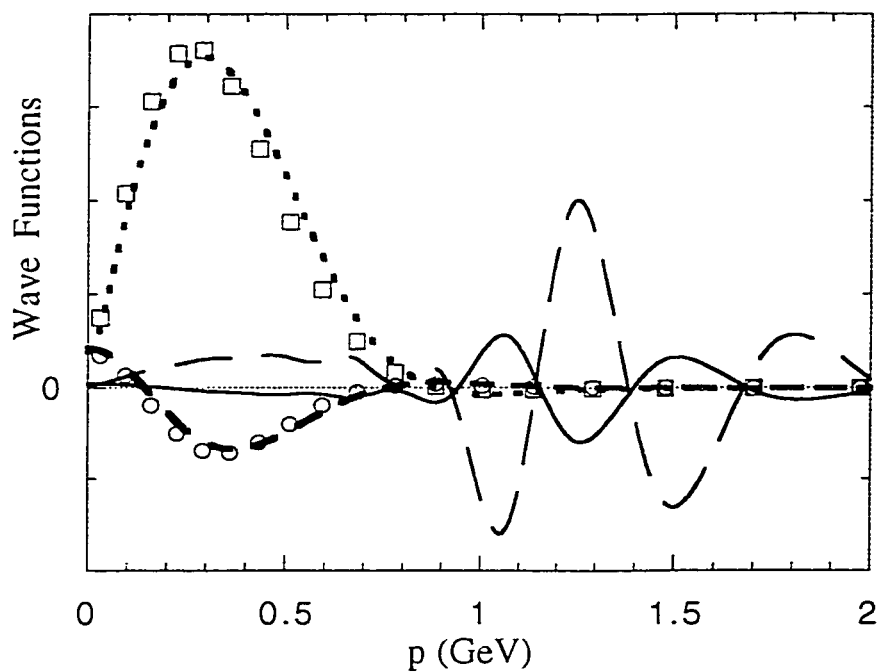


Figure 3.7: Negative ground state solutions of the quasirelativistic 1CS equation for $\gamma = 0.40$ labeled as in previous figure. Here $\kappa = 5.0$, $E_{-1} = -0.548$ GeV and $\kappa = 10.0$, $E_{-1} = -0.619$ GeV. The comparison Dirac level has energy $E_{-1} = 0.660$ GeV.

Table 3.5: First four positive and negative 1CS $\kappa=1.0$ binding energy levels for $y=0.0$, and 0.4 with Spline ranks of 24, 20, 16, and 12. (Energy in GeV)

Level	$y = 0.0$				$y = 0.4$			
	SN=24	SN=20	SN=16	SN=12	SN=24	SN=20	SN=16	SN12
4	1.881	1.881	1.881	1.881	2.222	2.222	2.222	2.223
3	1.630	1.630	1.630	1.632	1.884	1.884	1.884	1.884
2	1.294	1.293	1.293	1.293	1.461	1.461	1.461	1.461
1	0.745	0.745	0.745	0.745	0.853	0.853	0.853	0.853
-1	-0.329	-0.330	-0.331	-0.334	0.933	0.724	0.508	0.284
-2	-0.331	-0.332	-0.335	-0.341	0.727	0.527	0.326	0.122
-3	-0.334	-0.337	-0.342	-0.354	0.577	0.387	0.196	0.005
-4	-0.338	-0.343	-0.353	-0.379	0.454	0.272	0.091	-0.087

can therefore be made that the 1CS system *becomes more stable* as the γ^0 strength is decreased and the mass of the quark is increased. This can be seen by examining the Table 6.1 of the stability results in the conclusions chapter.

3.3.2 1CS with scalar versus four vector structure

The time has finally come to explore the stability results when the full four vector is used instead of just the γ^0 component. The same sets of values for the vector strength and mass ratio parameters are used here as before. It should be pointed out that the pure scalar systems here will of course match the $y=0.0$ systems in the previous analysis. The null vector strength was only considered here as a means to confirm the calculations and will therefore not be included. While all the systems are real, only the scalar-dominant cases for the 1CS equation can be stable. This is due to the fact that the vector-dominant half of the systems can be eliminated because they violate stability condition number two. These are the eight cases with a vector strength of $y=0.6$ or 1.0 and the four mass ratios. As a result, only the four cases where the vector strength is $y=0.4$ remain.

By examining Table 3.6 it can be seen that none of these systems violate the third stability condition. By comparing Table 3.6 with Table 3.4 and

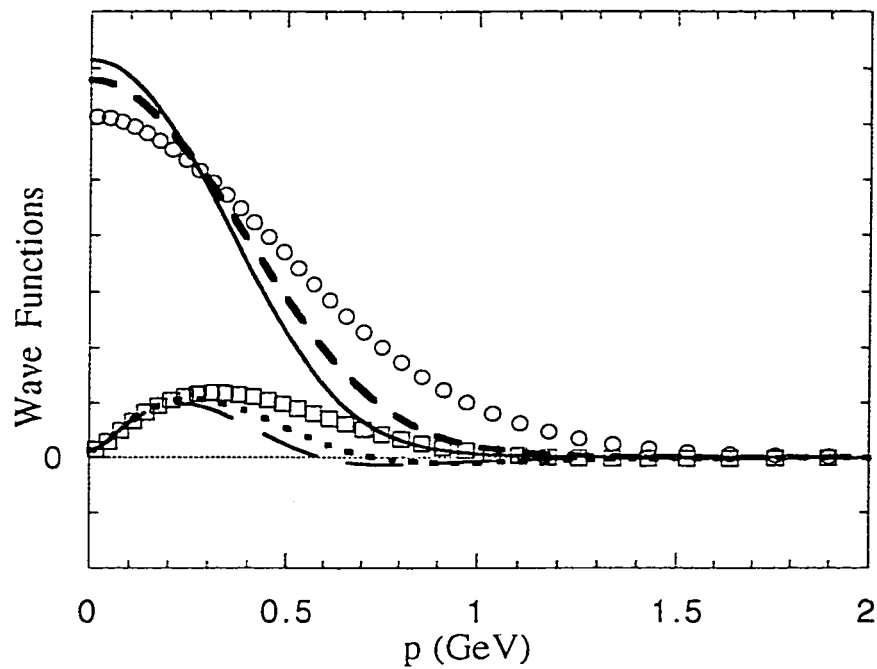


Figure-3.8: Positive ground state solutions for the quasirelativistic ICS equation with a pure scalar interaction. The solid and long dashed lines are for $\kappa=1.0$, $E_1=0.745$ GeV; the heavy short dashed and dotted lines are for $\kappa=2.0$, $E_1=0.857$ GeV. The scalar ground state Dirac solution for $E_1 = 0.976$ GeV is shown for comparison (circles and squares).

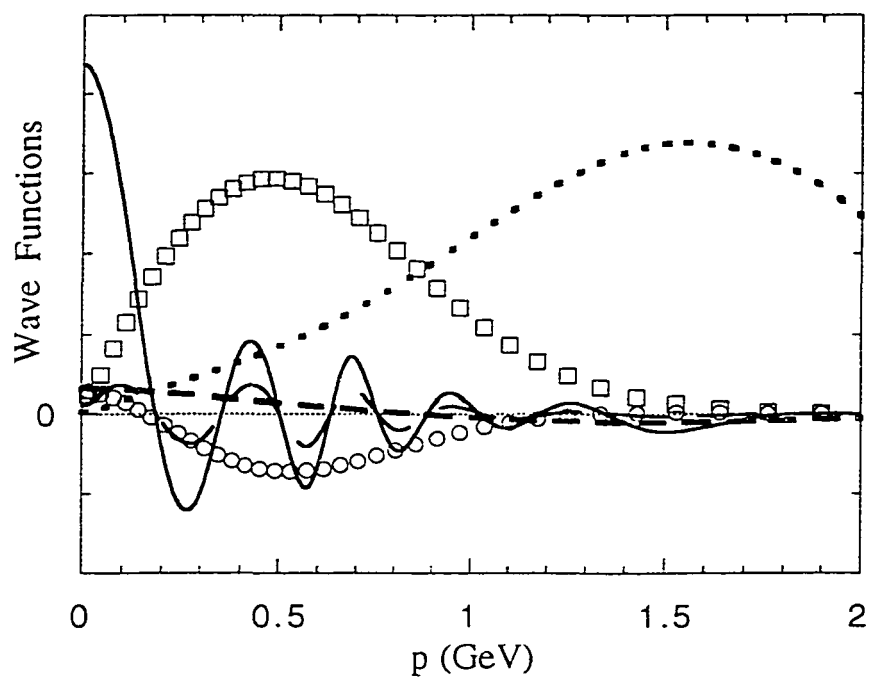


Figure 3.9: Negative ground state solutions labeled as in previous figure. Here the $\kappa = 1.0$ solution has an energy of $E_{-1} = -0.330$ GeV and the $\kappa = 2.0$ solution an energy of $E_{-1} = -0.607$ GeV compared to the Dirac energy of $E_{-1} = -1.249$ GeV.

Table 3.5 it can be observed that as κ increases the binding energy levels for the four vector system approaches the corresponding values for the time-like vector system. This in turn means that as the mass ratio increases, both $y=0.4$ systems approach the Dirac limit with identical vector strength.

Another interesting phenomenon to note from this table concerns the energy level separation as the mass ratio changes. For the positive levels the magnitude of the separation between adjoining states does not vary much for each system. On the other hand, as κ decreases the negative energy levels get closer together. As an example, consider the equal mass case where the difference between the negative ground and third excited states is approximately 0.006 GeV. Alternatively, when the mass ratio is 10.0 the difference between the same states is approximately 0.281 GeV. This would seem to indicate that the systems will start to grow unstable as the value of κ is decreased. In other words, the negative states become degenerate.

The mass ratios $\kappa=10.0$, 5.0, 2.0, and 1.0 now have only the fourth stability condition left to pass. Since both choices for the vector component converge to the Dirac limit, the $\kappa=10.0$ case will be declared completely stable, and skipped from further investigation. Now the wave function structure of the three remaining systems is examined for stability.

Table 3.6: First four positive and negative binding energy levels for $y=0.4$ $\kappa=1.0, 2.0, 5.0,$ and 10.0 with Spline ranks of 20, and 24 of the 1CS γ^μ systems (Energy in GeV).

Level	$\kappa = 1.0$		$\kappa = 2.0$		$\kappa = 5.0$		$\kappa = 10.0$	
	SN=20	SN=24	SN=20	SN=24	SN=20	SN=24	SN=20	SN=24
4	2.490	2.490	2.455	2.455	2.332	2.332	2.227	2.227
3	2.071	2.071	2.055	2.055	1.973	1.973	1.902	1.902
2	1.554	1.554	1.573	1.573	1.549	1.549	1.519	1.519
1	0.828	0.828	0.918	0.918	0.992	0.993	1.016	1.016
-1	-0.318	-0.318	-0.480	-0.480	-0.599	-0.599	-0.633	-0.633
-2	-0.323	-0.323	-0.526	-0.526	-0.699	-0.699	-0.746	-0.747
-3	-0.324	-0.324	-0.550	-0.550	-0.774	-0.774	-0.837	-0.837
-4	-0.324	-0.324	-0.565	-0.565	-0.834	-0.834	-0.914	-0.914

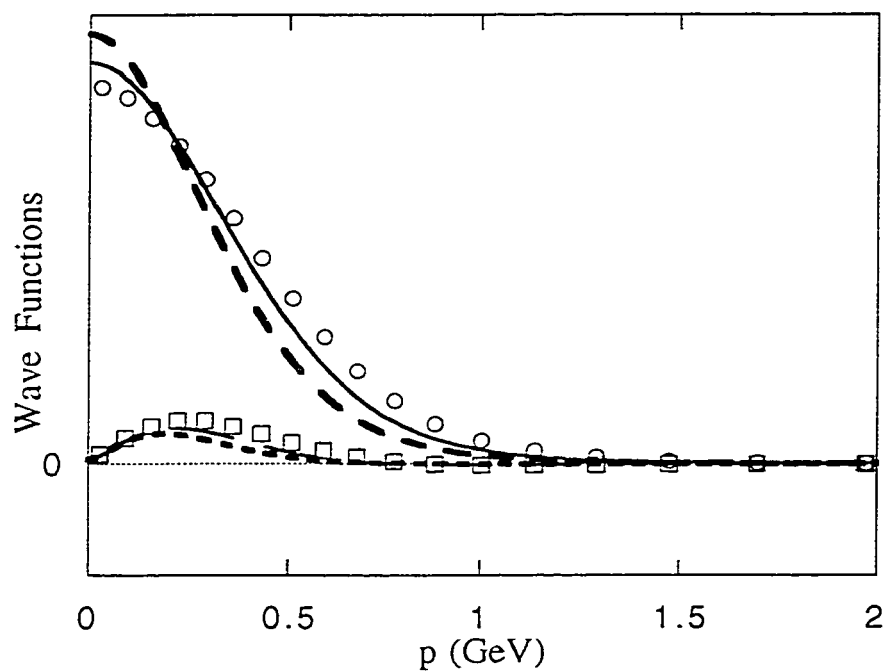


Figure 3.10: Positive ground state solutions for the quasirelativistic 1CS equation with a four vector strength of $\gamma=0.4$. For $\kappa=5.0$ the energy is $E_1=0.992$ GeV with the circles and squares used. The solid and long dashed lines are for $\kappa=2.0$, $E_1=0.0.918$ GeV; the heavy short dashed and dotted lines are for $\kappa=1.0$, $E_1=0.828$ GeV.

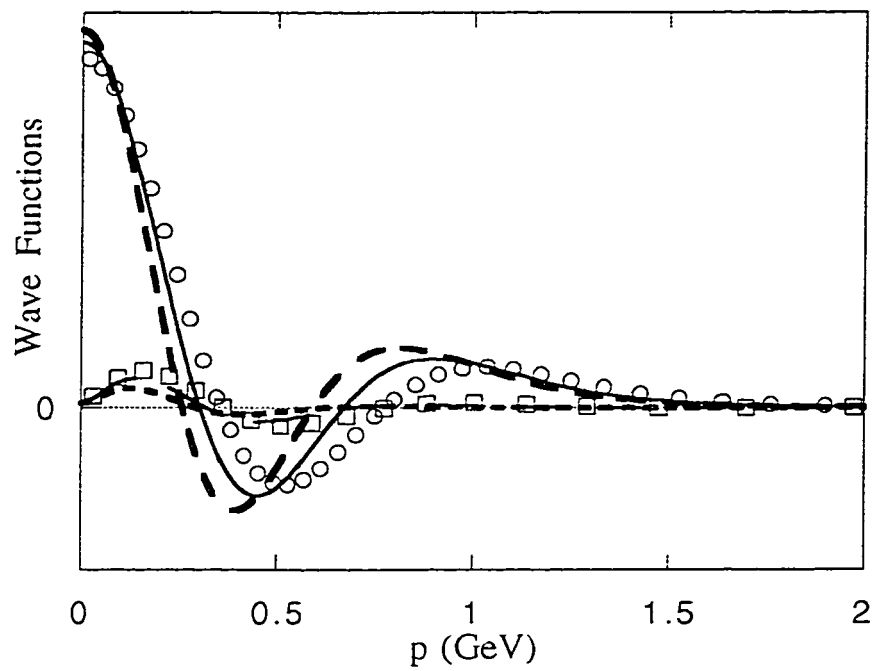


Figure 3.11: Positive second excited states here are labeled as in the previous figure. The $\kappa = 5.0$ solution has an energy of $E_3=1.973$ GeV and the $\kappa = 2.0$ solution an energy of $E_3=2.055$ GeV. For the equal mass system the level is $E_3=2.071$ GeV.

In Fig. 3.10 the positive ground states of $\kappa=5.0$, 2.0 and 1.0 are shown to all have the correct structures. This is also true for the positive second excited state depicted in Fig. 3.11. These results for the full four vector are contrary to those found when the time-like vector only was used. For those earlier γ^0 systems only the five-to-one mass ratio was stable for the positive energy levels and the rest were unstable. In fact when the negative ground, Fig. 3.12, and second excited states, Fig. 3.13, are examined the differences become greater. The $\kappa=5.0$ and 2.0 are compared to the corresponding Dirac levels and the structures indicate stability. The equal mass system was not shown on these two figures because of the momentum space scaling.

Examples of the equal mass system for the negative ground and second excited states are shown in Fig. 3.14 and Fig. 3.15 respectively. In these two cases the wave functions generated by a spline rank of 20 and 30 are shown together in order to confirm that the results are not a coincidence. The structures are correct but the momentum range extends out to approximately 8 GeV for the ground and 20 GeV for the second excited states. This is a significant change in the momentum range which would indicate that these negative states are more tightly confined around the position space origin than other systems examined thus far. This is unexpected given the fact that the negative energy levels are so close together. Such a condition would

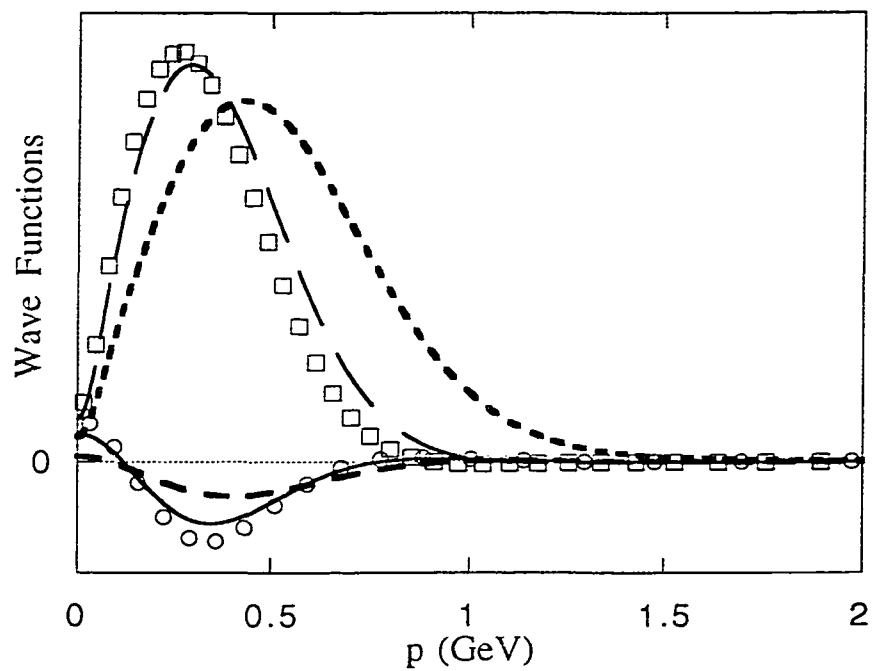


Figure 3.12: Negative ground state solutions for the quasirelativistic 1CS equation with a four vector strength of $\gamma=0.4$. For $\kappa=5.0$ the energy is $E_{-1}=-0.599$ GeV where the solid and long dashed lines are used. The heavy short dashed and dotted lines are for $\kappa=2.0$, $E_{-1}=-0.480$ GeV. The Dirac system used as a comparison state is represented by circles and squares with $E_{-1}=-0.660$ GeV.

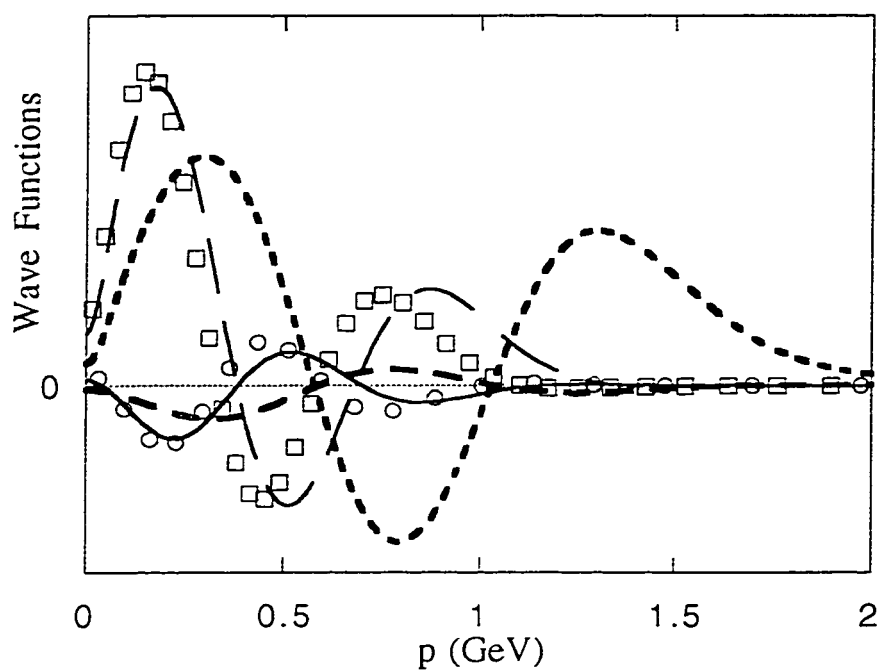


Figure 3.13: Negative second excited states here are labeled as in the previous figure. The $\kappa = 5.0$ solution has an energy of $E_{-3} = -0.774$ GeV and the $\kappa = 2.0$ solution an energy of $E_{-3} = -0.480$ GeV. For the Dirac system $E_{-3} = -0.879$ GeV.

imply that the negative states are degenerate, but one can see that they each have a distinct and proper structure. However, one must remember that the equal mass system is not a valid choice for the 1CS equation.

From this analysis we can conclude that the 1CS equation is stable when the four vector strength is $y=0.4$, and unstable for vector dominant systems. In fact, the $y=0.4$ system is stable for both positive and negative states as well as over all mass ratios. This is a considerable improvement over the γ^0 systems where only the *positive* pure scalar states were stable for all mass ratios. It is therefore of no surprise that the favored lorentz structure for the 1CS system is a scalar dominant mixed state with a four vector component greater than zero.

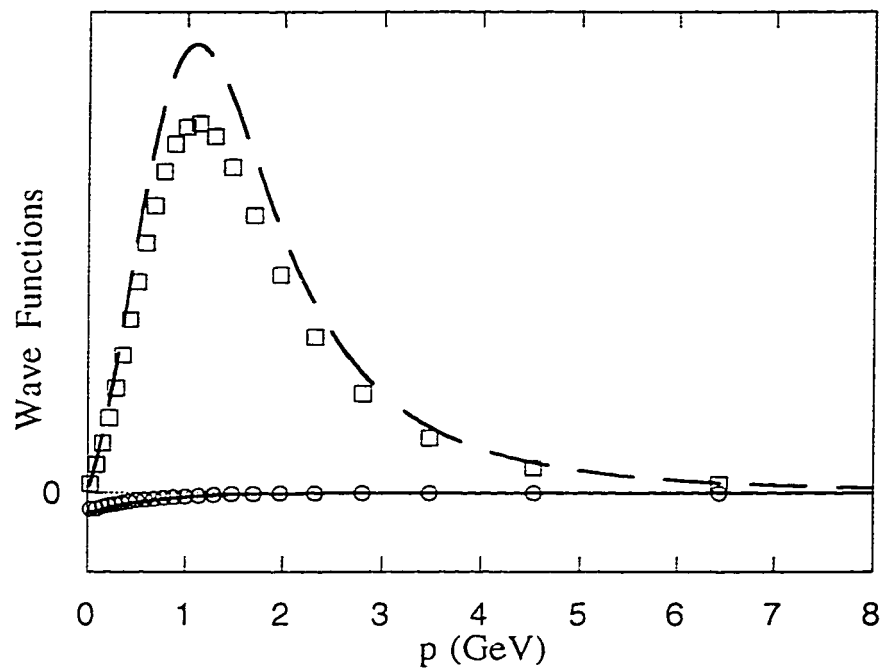


Figure 3.14: Negative ground state solutions for the quasirelativistic 1CS equation with a four vector strength of $y=0.4$. For $\kappa=1.0$ the energy is $E_{-1}=-0.318$ GeV for both a spline rank of 30 (circles and squares) and 20 (solid and long dashed lines).

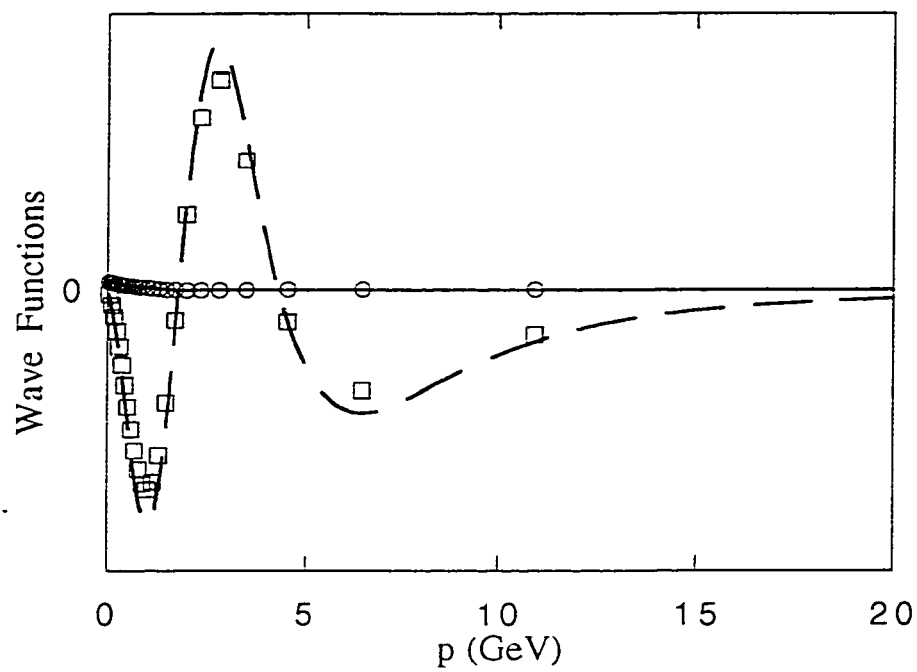


Figure 3.15: Negative second excited state solutions for the quasirelativistic 1CS equation with a four vector stength of $\gamma=0.4$. For $\kappa=1.0$ the energy is $E_{-3}=-0.324$ GeV for both a spline rank of 30 (circles and squares) and 20 (solid and long dashed lines).

Chapter 4

The Salpeter Equation

The Salpeter, or instantaneous Bethe-Salpeter equation, uses the approximation that the potential, or kernel, of the Bethe-Salpeter equation is independent of k_0 and p_0 . Therefore, in coordinate space the potentials and the wave functions are instantaneous, i.e. $t_1 = t_2$. At this time it should be stated that the Salpeter Equation has two undesirable features. First, neglecting the energy dependence of the kernel is unphysical. Second, there is no Dirac limit for this equation. When the mass of one of the particles is taken to infinity, the resulting equations do not reduce to a Dirac equation for the light quark moving in the field created by the heavy quark. Since the equal mass 1CS system is not a valid model and the Salpeter equation has

no Dirac limit, it was decided that only the equal mass limit $\kappa = 1.0$ system would be examined.

4.1 Derivation

The Salpeter equation uses the same steps as those for the 1CS equation, with one exception. In the derivation of the 1CS equation we placed particle 1 on shell, meaning that only pole one of Fig. 3.2 is included in the k_0 integration, thus producing Eq. (3.11). For the Salpeter equation pole 2, as defined in Eq. (3.10) must be included. When the fact that the potential, and thus the wave functions, are time independent is considered, the terms ψ_{1b} of pole 1 and ψ_{2b} of pole 2 are found to be equivalent and therefore cancel each other out.

When the equations are rederived utilizing these concepts the general equation is found to be

$$\Gamma_1^{\rho_1\rho_2}(p) = \int \frac{d^3k}{(2\pi)^3} V'_{11} \sum_{\rho'_1\rho'_2} \sum_{\lambda'_1\lambda'_2} \Theta_1^{\rho_1\rho'_1} \Gamma_1^{\rho'_1\rho'_2} G_2^{\rho'_2} \Theta_2^{\rho'_2\rho_2} \quad (4.1)$$

where $\rho_1 \neq \rho_2$ and $\rho'_1 \neq \rho'_2$. The second channel wave function, denoted ψ_{2a} , corresponds to propagation of the quark and antiquark in their negative energy state, and is equal to

$$\psi_{2a} = -\frac{\Gamma_1^{-+}}{E_{k_2} + E_{k_1} + \mu}. \quad (4.2)$$

The two wave functions, ψ_{1a} and ψ_{2a} satisfy the coupled equations

$$\begin{pmatrix} (\mu - 2E_p)\psi_{1a}(p) \\ (\mu + 2E_p)\psi_{2a}(p) \end{pmatrix} = \int_{\vec{k}} \bar{V} \begin{pmatrix} d_1 & d_5 \\ -d_5 & -d_1 \end{pmatrix} \begin{pmatrix} \psi_{1a}(k) \\ \psi_{1b}(k) \end{pmatrix}, \quad (4.3)$$

with

$$\begin{aligned} a_1 &= \mp Q & b_1 &= R \\ a_5 &= \pm W & b_5 &= X \\ Q &= 1 + \bar{p}^2 \bar{k}^2 & R &= 2\bar{p}\bar{k} \\ X &= 2\bar{p}\bar{k} & W &= \bar{p}_1^2 + \bar{k}^2, \end{aligned} \quad (4.4)$$

or for the four vector case the vector terms are

$$\begin{aligned} a_1 &= Q + 3W & b_1 &= R - X \\ a_5 &= -W - 3Q & b_5 &= X - R. \end{aligned} \quad (4.5)$$

All other terms have the same definitions as before.

4.2 The Equations

The same quasirelativistic potential used in the ICS system Eq. (3.20) is applied here . Utilizing the same steps as in corresponding sections the eigensystem used in the computer analysis is generated,

$$\int p^2 \beta_i(p) \beta_j(p) \begin{pmatrix} (\mu - 2E_p) \\ (\mu + 2E_p) \end{pmatrix} dp = \int dp dk \begin{pmatrix} \eta_{ij} & \eta_{5ij} \\ -\eta_{5ij} & -\eta_{ij} \end{pmatrix}, \quad (4.6)$$

where the same identities of Eq. (3.22) are used with $\eta_{ij} = PT_i(PT1_{ij} + PT2_{ij} + PT3_{ij})$. The alternate form of Eq. (4.4) and Eq. (4.5) containing the mixed Lorentz structure is

$$\begin{aligned} a_1 &= -Q & b_1 &= (1 - 2y)R \\ a_5 &= W & b_5 &= (1 - 2y)X \end{aligned} \tag{4.7}$$

and

$$\begin{aligned} a_1 &= -Q - 3yW & b_1 &= (1 - 2y)R + yX \\ a_5 &= W + 3yQ & b_5 &= (1 - 2y)X + yR \end{aligned} \tag{4.8}$$

respectively.

4.3 Stability Analysis

4.3.1 Salpeter with scalar versus time-like vector structure

As was the case in the ICS analysis, the γ^0 case is examined first. When the Salpeter equation is considered the pure scalar case proves to be the only system which fails stability condition 1 by possessing complex eigenvalues. Not only are imaginary bound state masses present, there is also no relation between the eigenvalues as the spline rank is varied. This is shown in Table 4.1 for the squared of the bound state masses. However, the remaining vector

Table 4.1: First four bound state mass levels squared of the Salpeter Equation for $y=0.0$, and 0.4 with various Spline ranks. (Energy in GeV)

Level	$y = 0.0$		$y = 0.4$		
	SN=20	SN=12	SN=20	SN=16	SN=12
± 4	0.685	2.173	5.632	5.632	5.674
± 3	-1.074	1.538	4.383	4.383	4.385
± 2	-3.869	0.931	2.977	2.977	2.976
± 1	-8.705	-0.051	1.339	1.339	1.339

strengths pass condition 2 and condition 3. Taking $y=0.4$ as an example, the spectra shows there is a positive and negative state of equal magnitude which do not vary with the spline rank. This symmetry is of no surprise when you consider the Salpeter matrix Eq. (4.3). This same symmetry is also evident in the wave functions, as illustrated in Fig. 4.1. The wave functions for the positive and negative ground states are a perfect match with the only difference being $\psi_{1a} \rightarrow \psi_{2a}$ and vice-versa.

The two figures, Fig. 4.1 (ground state) and Fig. 4.2 (second excited state), demonstrate that these Salpeter systems have the correct structure compared to their Dirac counterparts. In addition, Fig. 4.3 helps to illustrates

that $y=0.6$ and 1.0 are indeed stable by showing their correct structure for the second excited state. It was determined that only the pure scalar Salpeter equation is unstable.

While it is true that the scalar Salpeter equation is unstable for an equal quark-antiquark mass of 0.325 GeV, the question is what happens when the mass is increased. It turns out that increasing the mass of the components has a similar effect as decreasing the linear confining coefficient. It would seem reasonable to conclude that by decreasing the confining coefficient the system would not be as tightly bound and would therefore still produce unstable solutions for the pure scalar case. This is the opposite of what was found when the solutions for a mass of 0.85 GeV was explored. The $y=0.0$ Salpeter system was determined to be stable up to a point. This means that the system completely satisfies condition 1, and condition 3 is always met by virtue of the symmetry between the positive and negative states, however, the other two are another story.

The requirement that the system does not vary with the spline rank is a much more difficult concept. By examining Table 4.2 the point can be made clearly. The first six positive energy levels are listed for a spline rank of 30, 20, and 12. It can be observed that the ground state energy does not vary

.

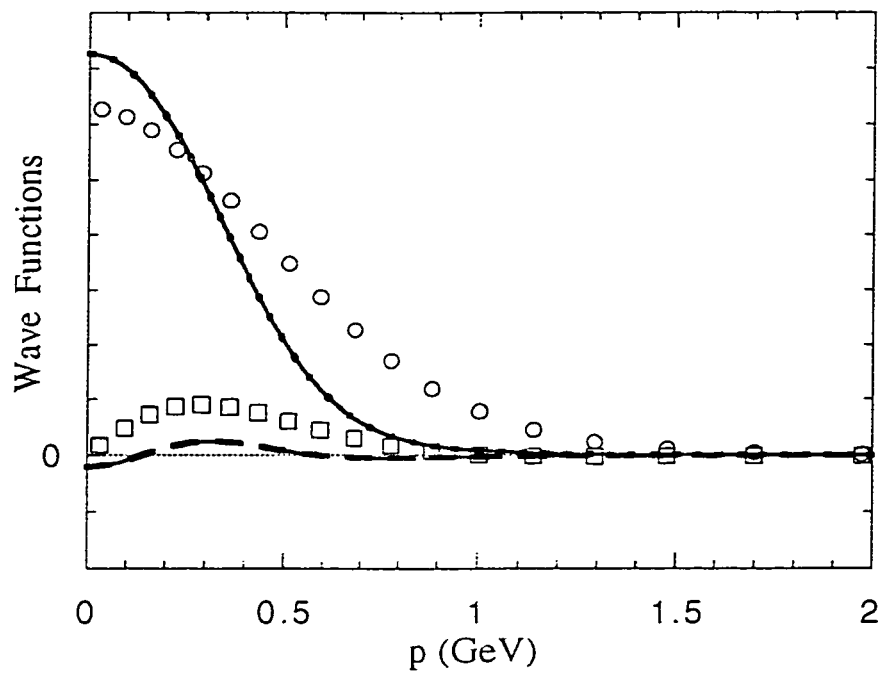


Figure 4.1: Positive and negative ground state solutions for the $y = 0.4$ quasirelativistic equal mass Salpeter equation, $\mu_1=1.157$ GeV (solid and long dashed lines) and $\mu_{-1}=-1.157$ GeV (heavy short dashed and dotted lines). The positive ground state Dirac solutions for $y=0.4$, $E_1=1.028$ GeV (circles and squares) are shown for comparison.

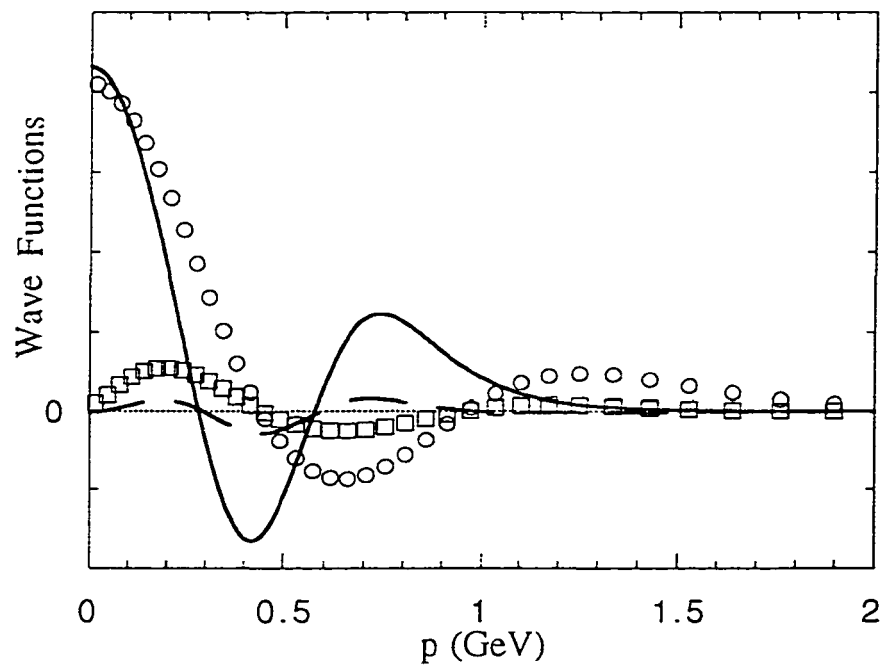


Figure-4.2: The positive second excited state solutions for the $y=0.4$ equal mass Salpeter equation, $\mu_3 = 2.094$ GeV (solid and long dashed lines) are compared to the second positive excited state Dirac solution for $y = 0.4$, $E_3=1.772$ GeV (circles and squares).

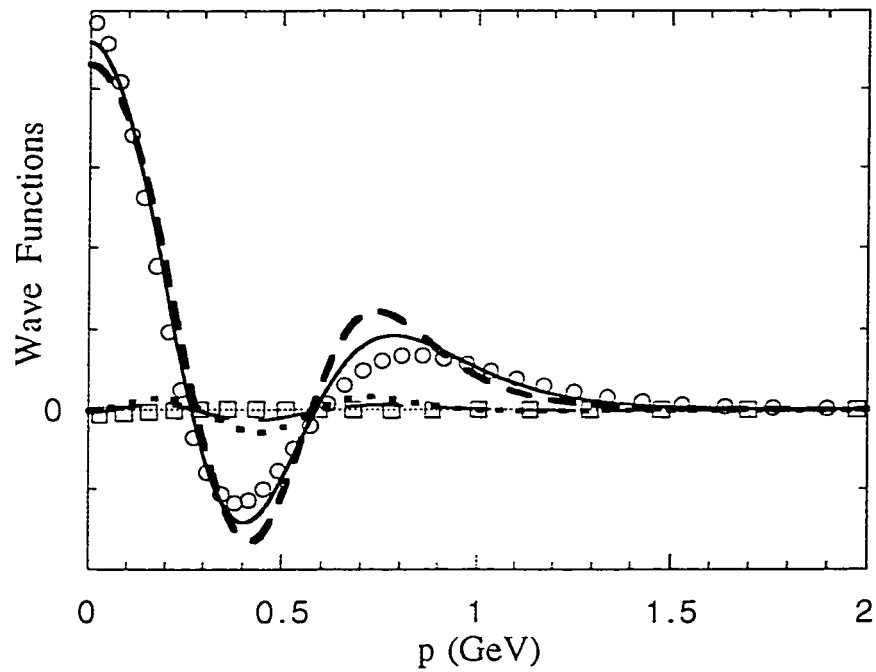


Figure 4.3: Positive second excited state solutions for the Salpeter equation for a variety of scalar/vector mixings: pure vector $y=1.0$, $\mu_3=2.565$ GeV (circles and squares); $y=0.6$, $\mu_3=2.284$ GeV (solid and long dashed lines); and $y=0.4$ $\mu_3=2.094$ GeV (heavy short dashed and dotted lines).

Table 4.2: First Six bound state mass levels of the Salpeter Equation for $y=0.0$ with $m=0.85$ GeV and various Spline ranks. (Energy in GeV)

Level	SN=30	SN=20	SN=12
6	3.375	3.482	3.655
5	3.347	3.354	3.434
4	3.194	3.195	3.202
3	2.974	2.974	2.977
2	2.665	2.664	2.665
1	2.185	2.185	2.185

much with the spline rank. The stability of this level is further demonstrated in Fig. 4.4 which plots the wave functions for a spline rank of 20 and 30.

When the fourth excited state is examined the magnitudes are still in agreement but something is wrong with their wave functions. In Fig. 4.5 we can see that the ψ_{1a} and ψ_{1b} wave functions agree by spline rank but their structures degrade from the accepted norm as the momentum increases. This degradation becomes more pronounced as the spline rank increases. This would seem to indicate that the problem lies in the asymptotic limit of the system. Note, as the spline rank is increased the structure of the wave

functions at higher momentum are more precisely defined. As such, any resulting instabilities become more pronounced as the spline rank increases. Finally, by the time the fifth excited state is reached both the energy levels and the wave functions, Fig. 4.6, no longer pass the two stability conditions.

However, this does not mean that the system is useless. In fact, even systems which have been found to be completely stable previously have their problems as well. Since more energy levels are defined as the spline rank increases it is natural that the highly excited states for that spline rank would be unstable. For instance, the fact that the 28th excited state does not exist for a spline rank of 20 but does for a rank of 30 would automatically violate condition number 2. In addition the wave functions for such a state would have very poor structure since there are not enough spline functions to define that highly structured state at large p . Another fact to remember is that this is a numerical calculation and as such it can only be as accurate as its integration and eigensystem solving tolerances. The point here is that these stable states do have a limit to their stability. The only difference is that their instability occurs at higher levels than the $y=0.0$ case considered here. Therefore, so long as the system is stable in the region of energy that you are interested in and for the tolerances you prescribe, it may be used as a stable system.

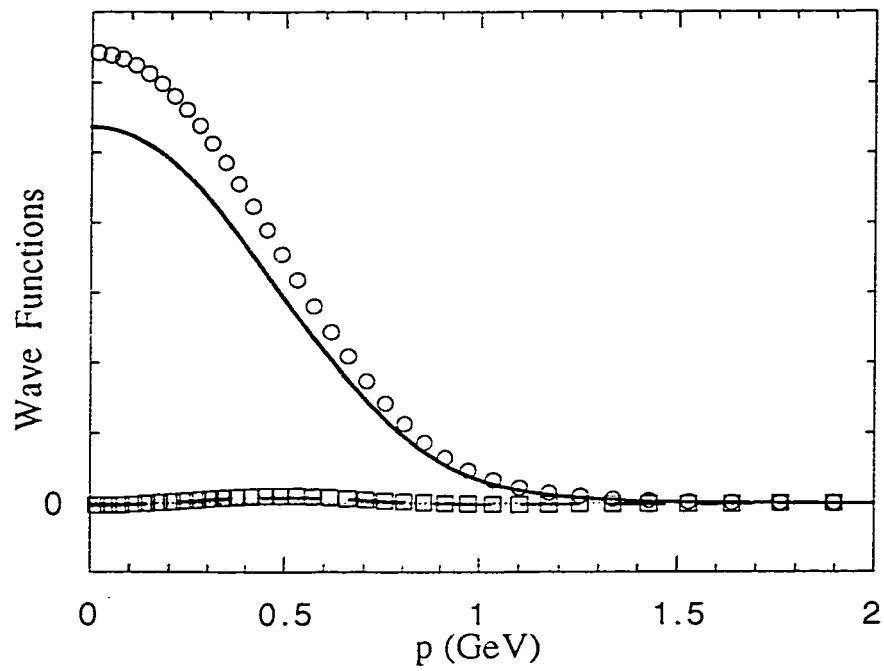


Figure 4.4: Positive ground state pure scalar solutions for the Salpeter equation $\mu_1=2.185$ GeV spline rank of 20 (circles and squares) and spline rank of 30 (solid and long dashed lines).

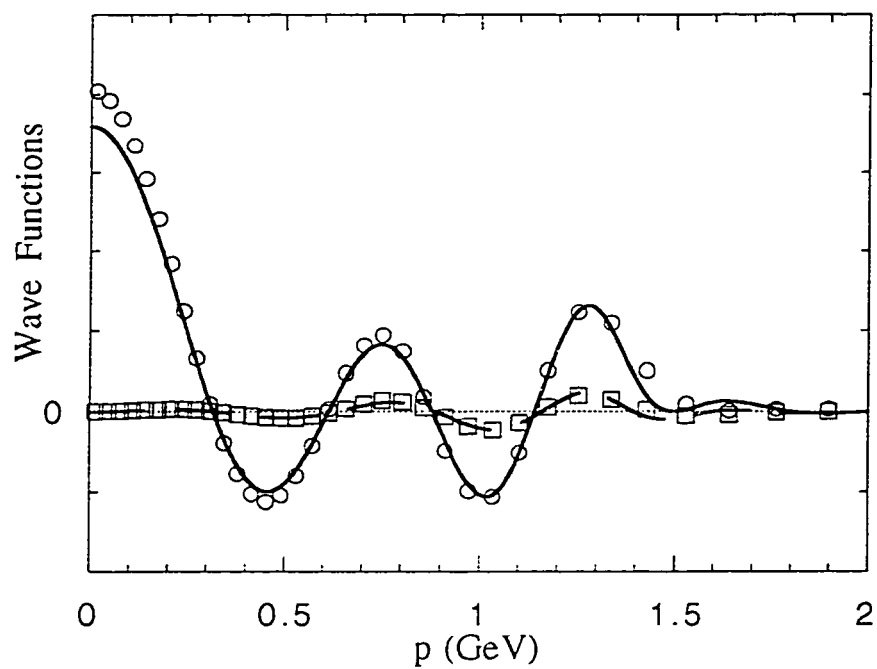


Figure 4.5: Positive fourth excited state pure scalar solutions for the Salpeter equation $\mu_5=3.354$ GeV spline rank of 20 (circles and squares) and spline rank of 30 $\mu_5=3.347$ GeV (solid and long dashed lines).

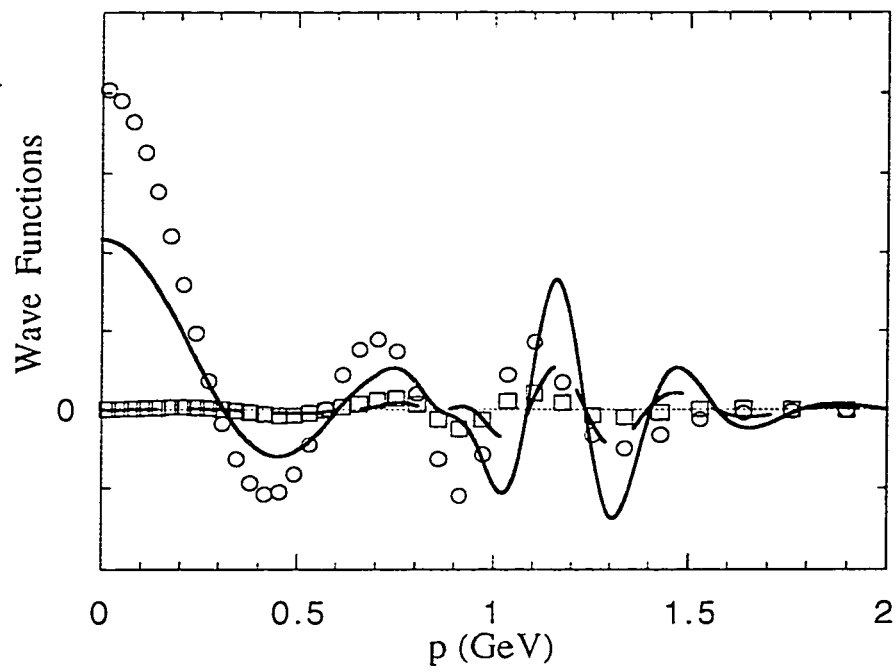


Figure 4.6: Positive fifth excited state pure scalar solutions for the Salpeter equation $\mu_6=3.482$ spline rank of 20 (circles and squares) and spline rank of 30 $\mu_6=3.375$ GeV (solid and long dashed lines).

4.3.2 Salpeter with scalar versus four vector structure

From the very beginning the results for this version of the Salpeter equation do not look good. It turns out that all eigenvalues for the vector strength are complex, which of course violates stability condition 1. This would be the end of a very short section if it was left at that. Instead, the masses of the quark and antiquark will be increased from 0.325 GeV until stability is found, if at all. To start, the masses were increased by a factor of ten for the three vector strengths, $y=1.0$, 0.6, and 0.4. The only system found not to have complex eigenvalues was $y=0.4$. As was the case for the 1CS equation, this was a dramatic change from the previous γ^0 results where the vector dominant systems were stable. Since it is reasonable to say that only the $y=0.4$ system might be stable, it will be the only one considered from here on.

The mass of the quark and antiquark will be set to five times the light quark mass, or $m=1.625$ GeV. Table 4.3 lists the bound state mass values for the first six positive levels with a spline rank of 30, 20, and 12. From the ground state to the second excited state the values for all three spline cases match up. This is also true for the wave functions as well, as shown in Fig. 4.7 which demonstrates the second excited state.

Table 4.3: First Six bound state mass levels of the Salpeter Equation for $y=0.0$ with $m=1.625$ GeV and various Spline ranks. (Energy in GeV)

Level	SN=30	SN=20	SN=12
6	4.885	5.054	5.065
5	4.687	4.885	4.887
4	4.508	4.686	4.687
3	4.448	4.448	4.448
2	4.150	4.150	4.150
1	3.735	3.735	3.735

The problem arises for the third excited state where the spline rank is 30, which is shown in bold face in Table 4.3. The bound state mass does not match the values from the other two cases. The structure of the wave functions illustrate its unstable nature, as seen in Fig. 4.8. In addition to its oscillatory nature, the visible structure is at very low momentum. This is the first time such a property has been observed and its significance is unclear at this time.

On the other hand the fourth excited state does have the correct energy for a third excited state. In fact the fifth excited state energy matches what the fourth energy should be. In addition, the structure of the fourth excited state's wave functions correspond to that of the third excited state given by the case where the spline rank is 20. Fig. 4.9. This indicates that the energy level in question is spontaneously generated and could be caused by either the physics of the system or a mathematical manifestation. Regardless, the lesson learned here is the same as that from the pure scalar Salpeter equation. Some systems have a limited stability which varies with the mass of the quark and antiquark. So long as you are aware of the range of the stability the system could be utilized.

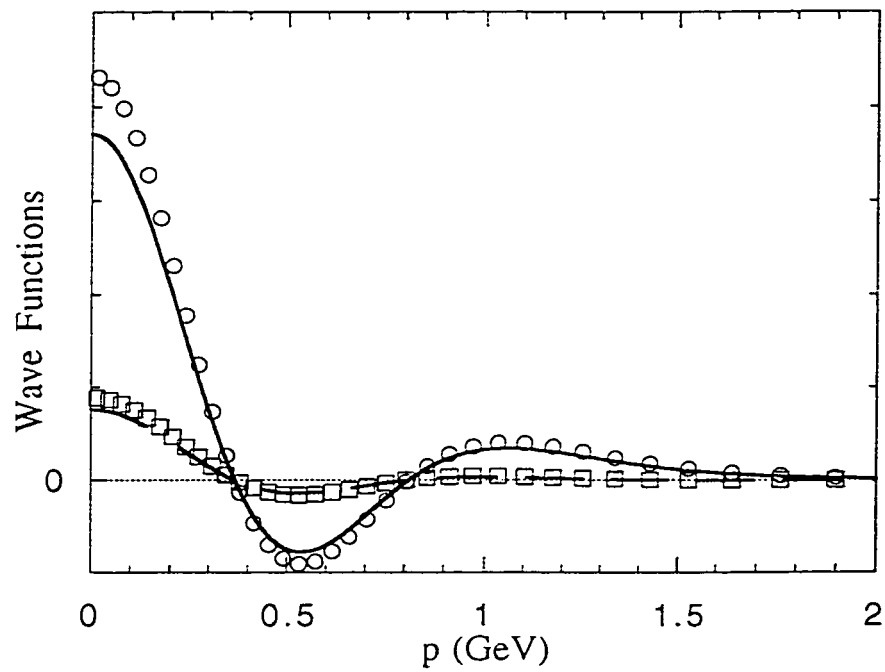


Figure 4.7: Positive second excited state. γ^{μ} $y=0.4$, solutions for the Salpeter equation $\mu_3=4.448$ GeV spline rank of 20 (circles and squares) and spline rank of 30 (solid and long dashed lines).

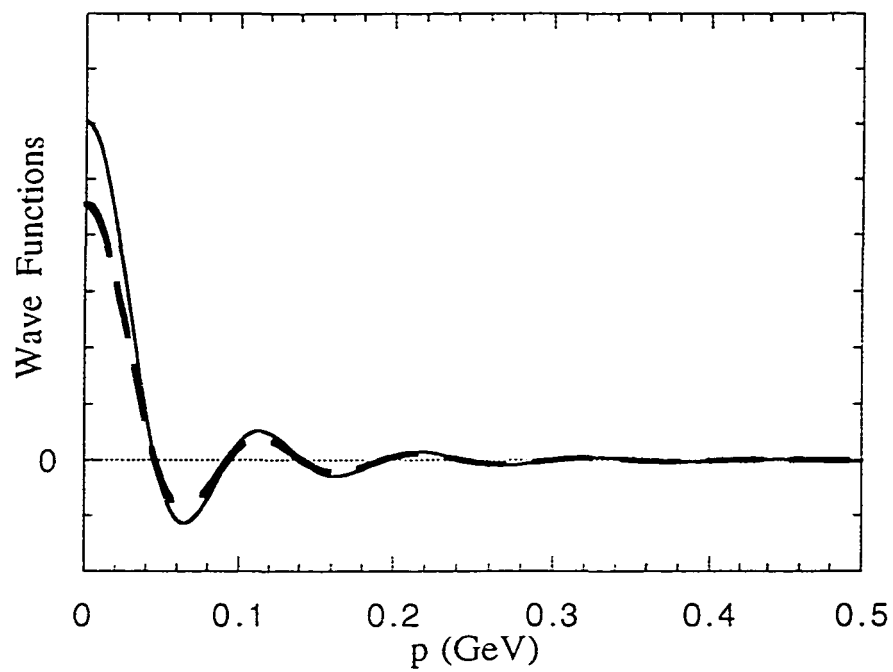


Figure 4.8: Positive third excited state, γ^4 $y=0.4$, solutions for the Salpeter equation $\mu_4=4.508$ GeV with a spline rank of 30 (solid and heavy long dashed lines).

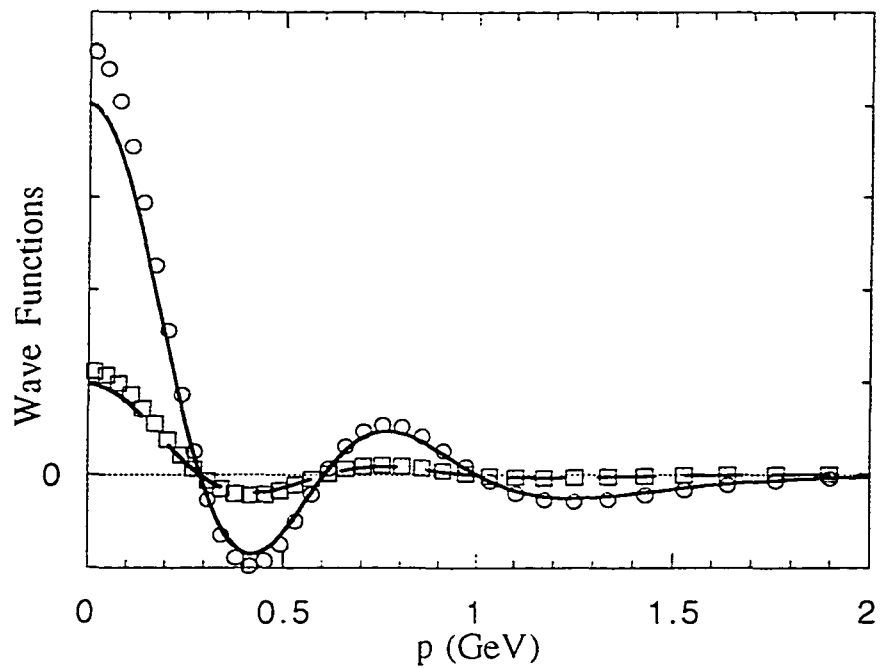


Figure 4.9: Salpeter equation, γ^t $y=0.4$, third excited state $\mu_4=4.686$ spline rank of 20 (circles and squares) and fourth excited state with a spline rank of 30 $\mu_5=4.687$ GeV (solid and long dashed lines).

Chapter 5

Theoretical Analysis

In this chapter the Dirac, and ICS equations will be investigated using approximation techniques to solve their coupled equations. This will be done using only the time-like structure for the vector component of the mixed Lorentz structure. The reason for this is simple, we are not trying to redo the stability analysis done already. Instead, the purpose is to gain insight into why the different systems exhibit certain characteristics.

Unfortunately, the approximation techniques used here for both systems require a different form of their defining equations than were generated in the chapters on their numerical solutions. In fact, it was found that the systems were easier to solve in position space. Rather than giving a complete outline of the calculations needed to derive these new equations, an abbreviated

version is shown instead. A more complete derivation of these systems is illustrated in a paper submitted for publication by Dr. Gross and myself [19].

5.1 Derivation of the general equations

Both equations can be derived from a simple general equation,

$$\begin{aligned} & \left(m_2 - \left[E_B + m_1 - \sqrt{m_1^2 - \nabla^2} \right] \gamma^0 + i \gamma^i \partial_i \right) \Phi(\mathbf{r}) \\ & = -\hat{\Theta} \left(\left[\sigma r - C(p^2) \right] (1 \mp \tilde{p}_1^2) \mp \frac{\sigma}{r} \frac{1}{(E_1 + m_1)^2} \right) \mathcal{N} \Phi(\mathbf{r}), \end{aligned} \quad (5.1)$$

where the upper sign once again stands for the scalar structure and the lower is the vector structure of the potential vertex. The derivation of this equation can be found in the aforementioned article, Ref. [19]. The term $C(p^2)$ is defined as

$$C(p^2) = \frac{2\sigma}{\pi m_1} \left\{ \frac{m_1}{E_{p_1}} + \frac{m_1^3}{p E_{p_1}^2} \log \left(\frac{E_{p_1} + p}{m_1} \right) \right\}, \quad (5.2)$$

$E_1 = \sqrt{m_1^2 - \nabla^2}$ and $\mathcal{N} = N_{p_1} N_{k_1} / \sqrt{4E_{p_1} E_{k_1}}$. The same mixed kernel used in the numerical derivations is applied here as well. A little hindsight will be applied here, thanks to the numerical results we can correctly assume a ground state solution of the form

$$\Phi(\mathbf{r}) = \begin{pmatrix} f(r) \\ -ig(r)\sigma \cdot \hat{\mathbf{r}} \end{pmatrix} \chi. \quad (5.3)$$

Applying both of these principles to Eq. (5.1) will result in its reduction to a set of coupled equations shown below for radial wave functions $f(r)$ and $g(r)$.

$$\begin{aligned}
& (E_B - m_2 - [E_1 - m_1]) f + \frac{dg}{dr} + \frac{2}{r}g \\
&= \left((\sigma r - C) [1 - \tilde{p}_1^2 (1 - 2y)] - \frac{\sigma}{r} \frac{(1 - 2y)}{(E_1 + m_1)^2} \right) \mathcal{N} f \\
& (E_B + m_2 - [E_1 - m_1]) g - \frac{df}{dr} \\
&= - \left((\sigma r - C) [(1 - 2y) - \tilde{p}_1^2] - \frac{\sigma}{r} \frac{1}{(E_1 + m_1)^2} \right) \mathcal{N} g. \quad (5.4)
\end{aligned}$$

5.2 Theoretical Analysis of the Dirac Equation

In order to derive the Dirac equation the limit $m_1 \rightarrow \infty$ is applied to Eq. (5.4). The result is

$$\begin{aligned}
E_B f &= (m_2 + \sigma r) f - \frac{dg}{dr} - \frac{2}{r}g \\
E_B g &= (-m_2 - \sigma r(1 - 2y)) g + \frac{df}{dr}, \quad (5.5)
\end{aligned}$$

which turns out to be the exact Dirac equation. When these coupled equations are take to large r they simplify to

$$\sigma r f - \frac{dg}{dr} = 0$$

$$-\sigma r(1 - 2y)g + \frac{df}{dr} = 0. \quad (5.6)$$

The solutions to Eq. (5.6) depend on the value for the vector strength. When $y < 1/2$ the two radial wave functions are

$$f(r) = N_f e^{-\sqrt{1-2y} \frac{1}{2}\sigma r^2} \quad g(r) = N_g e^{-\sqrt{1-2y} \frac{1}{2}\sigma r^2}, \quad (5.7)$$

where

$$N_f = -\sqrt{1-2y} N_g. \quad (5.8)$$

It should be noted that these equations approach zero as $r \rightarrow \infty$, and become less confined as $y \rightarrow 1/2$.

For $y > 1/2$ the solutions are a linear combination of the two independent solutions

$$\begin{aligned} f_1(r) &= N_{f_1} \sin\left(\sqrt{2y-1} \frac{1}{2}\sigma r^2\right) & g_1(r) &= N_{g_1} \cos\left(\sqrt{2y-1} \frac{1}{2}\sigma r^2\right) \\ f_2(r) &= N_{f_2} \cos\left(\sqrt{2y-1} \frac{1}{2}\sigma r^2\right) & g_2(r) &= N_{g_2} \sin\left(\sqrt{2y-1} \frac{1}{2}\sigma r^2\right), \end{aligned} \quad (5.9)$$

with

$$\begin{aligned} N_{f_1} &= -\sqrt{2y-1} N_{g_1} \\ N_{f_2} &= \sqrt{2y-1} N_{g_2}. \end{aligned} \quad (5.10)$$

These wave functions are oscillatory and escape to large r . Both the scalar and vector dominant solutions match the results shown in Fig. 1.4 (stability) and Fig. 1.5 (instability) respectively.

The Dirac system turned out to be the simplest case to solve, not surprisingly. The 1CS equation will require a more complex technique to solve it. The method chosen is a variational-like technique, which can also be applied to the Dirac equation. When this is accomplished the result is Fig. 5.1 which shows how the binding energy varies with the variational parameter γ . The variational parameter can be linked to the momentum of the system. The four vector strengths $y=0.0, 0.4, 0.6,$ and 1.0 have the same characteristics in the positive energy region. They drop down from infinity at $\gamma=0.0$ to some minimum value, which corresponds to that curves solution for the ground state energy. Then the curves continue on to infinity as $\gamma \rightarrow \infty$.

The negative states however are not so simple, and it is here that the stability of the system is determined. In Fig. 5.1 the scalar dominant curves come from negative infinity at $\gamma=0.0$, reach a maximum still in the negative region and proceed back to negative infinity as the variational parameter increases. The vector dominant curves however start at positive infinity at low γ and then drop to the negative energy region where they eventually mimic the same trajectory as the $y=0.0$ and 0.4 curves at high γ . The $y=0.6$ and 1.0 curves have no critical point resulting in a calculated maximum which would have been its negative ground state energy.

The significance of this feature is important, for here we can graphically see what is happening. Consider a positive or negative state for either of the vector-dominant cases. When trying to find its energy, either positive or negative, the state can begin on one curve and tunnel through to the other at the same energy level it started with. Due to the physics of quantum mechanics a state has a certain probability of quantum tunneling through a barrier, thus appearing on the other side. The probability of this event increases as the thickness of this barrier. The division between the positive and negative curves at the same energy. decreases.

As a result of this property the energy level of the state in question can be found anywhere the two curves cover, which is positive to negative infinity. This is exactly what is found from the numerical results. The energy levels of the vector-dominant systems vary with the spline rank used to calculate that case. This is a violation of stability condition 2. The application of this variational technique will be illustrated in the next section which deals with the 1CS system.

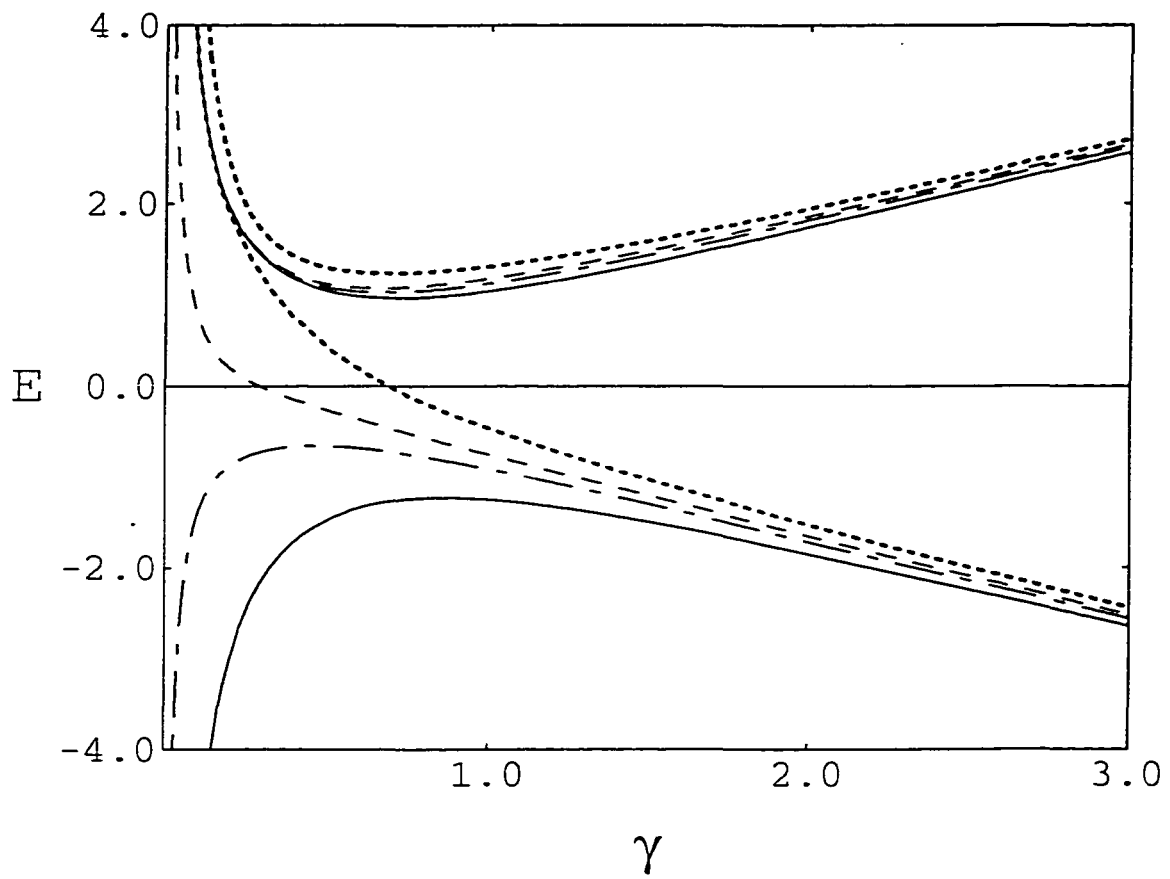


Figure 5.1: The Dirac energy $E = E_B$ as a function of the variational parameter γ for different mass ratios $y = 0$ (solid line), $y = 0.4$ (dot-dashed), $y = 0.6$ (dashed), and $y = 1.0$ (dotted).

5.3 Theoretical Analysis of the 1CS Equation

The difficulty in solving the 1CS equations is the presence of the operators $\sqrt{m_1^2 - \nabla^2}$ and \vec{p}_1^2 . The way to solve this problem is to reduce Eq. (5.4) to its simplest form and find the functions which will solve it. Then, parameters may be added to these functions which will be adjusted in order to solve the original coupled equations. This is the variational-like method utilized at the end of the Dirac section.

The first step is to set the linear potential coefficient, σ , to zero. The exact solutions to these equations for a pair of free particles are a set of spherical Bessel functions of order l ,

$$\begin{aligned} f(r\gamma) &= f_0 j_0(\gamma r) \\ g(r\gamma) &= g_0 j_1(\gamma r). \end{aligned} \quad (5.11)$$

Once again we have used the knowledge gained from the numerical analysis to choose the basic form of the solution functions. The energy of this system, which is a function of the parameter γ ,

$$E_B(\gamma) = \left[\sqrt{m_1^2 + \gamma^2} - m_1 \right] \pm \sqrt{m_2^2 + \gamma^2}. \quad (5.12)$$

Already the positive and negative energy regions can be observed as well as the Dirac limit where the energy is defined by $\sqrt{m_2^2 + \gamma^2}$.

When we set $\sigma \neq 0$ the system can no longer be solved analytically. Instead a matrix system based on Bessel functions rather than splines will be utilized in order to estimate the energies of the systems. These estimates will be optimized by adjusting the parameter γ . A plot of the functions $f(x)$ and $g(x)$ is illustrated as the heavy lines in Fig. 5.2 where $x = \gamma r$. It should be noted that the form of $f(x)$ represents a s-wave while $g(x)$ is a p-wave.

To improve the accuracy of the calculations a tail constructing function was added to the simple Bessel functions which makes them resemble the numerical wave functions. The spherical Bessel function $h_l(\omega r)$ was joined with $j_l(\gamma r)$ so that the new function and its first derivative are continuous. These new solutions are also depicted in Fig. 5.2 with three different tails. However, it was found that these tails did not improve the calculations significantly. Therefore they were dropped and the simple wave function was used instead which has the range

$$\begin{aligned}
 f(r) &= \begin{cases} f_o j_0(\gamma r) & \gamma r < \pi \\ 0 & \gamma r > \pi \end{cases} \\
 g(r) &= \begin{cases} g_o j_1(\gamma r) & \gamma r < n_1 \\ 0 & \gamma r > n_1 \end{cases} .
 \end{aligned} \tag{5.13}$$

The constant $n_1=4.493$ is the location of the zero for j_1 .

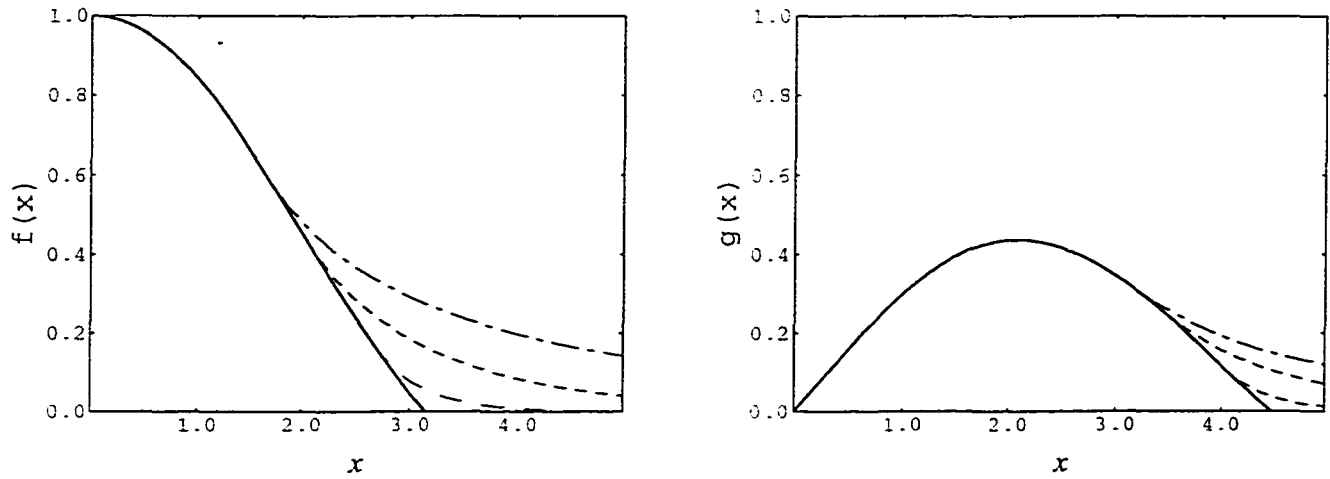


Figure 5.2: The trial wave functions $f(x)$ and $g(x)$ as a function of $x = \gamma r$. The different tails are for the cases $\omega/\gamma = 0.1$ (biggest tail), 0.5, and 2.0 (smallest tail), as discussed in the text.

The benefit of using Bessel functions is that they are eigenfunctions of ∇^2 , which allows for the calculation of the operators $\sqrt{m_1^2 - \nabla^2}$ and \tilde{p}_1^2 .

$$\begin{aligned}\nabla^2 f(r) &= \frac{1}{r} \frac{\partial^2}{\partial r^2} r f(r) = -\gamma^2 f(r) \\ \nabla^2 g(r) &= \left(\frac{1}{r} \frac{\partial^2}{\partial r^2} r - \frac{2}{r^2} \right) g(r) = -\gamma^2 g(r) .\end{aligned}\quad (5.14)$$

The functions f and g are substituted into Eq. (5.4), with the first equation multiplied by $j_0(\gamma r)$ and the second by $j_1(\gamma r)$. The coupled equations are then integrated over $d^3 r$ resulting in

$$\left(E_B - \left[\sqrt{m_1^2 + \gamma^2} - m_1 \right] - m_2 \right) f_o + \gamma g_o$$

$$\begin{aligned}
&= \left\{ \left(\frac{\sigma c_1}{\gamma} - C(\gamma^2) \right) (1 - \tilde{p}_1^2 (1 - 2y)) - \frac{\sigma c_2}{\gamma} \tilde{p}_1^2 (1 - 2y) \right\} \mathcal{N} f_o \equiv S_f f_o \\
&\left(E_B - \left[\sqrt{m_1^2 + \gamma^2} - m_1 \right] + m_2 \right) g_o - \gamma b f_o \\
&= - \left\{ \left(\frac{\sigma c_3}{\gamma} - C(\gamma^2) \right) (1 - 2y - \tilde{p}_1^2) - \frac{\sigma c_4}{\gamma} \tilde{p}_1^2 \right\} \mathcal{N} g_o \equiv -S_g g_o, \quad (5.15)
\end{aligned}$$

where

$$c_1 = \frac{\int_0^\pi x^3 dx j_0^2(x)}{\int_0^\pi x^2 dx j_0^2(x)} = 1.571 \quad c_3 = \frac{\int_0^{n_1} x^3 dx j_1^2(x)}{\int_0^{n_1} x^2 dx j_1^2(x)} = 2.659 \quad (5.16)$$

$$c_2 = \frac{\int_0^\pi x dx j_0^2(x)}{\int_0^\pi x^2 dx j_0^2(x)} = 0.776 \quad c_4 = \frac{\int_0^{n_1} x dx j_1^2(x)}{\int_0^{n_1} x^2 dx j_1^2(x)} = 0.412$$

and

$$b = \frac{\int_0^\pi x^2 dx j_1^2(x)}{\int_0^{n_1} x^2 dx j_1^2(x)} = 0.734. \quad (5.17)$$

When Eq. (5.15) is solved for the eigenvalues of the binding energies the result is a function of γ .

$$E_B = \sqrt{m_1^2 + \gamma^2} - m_1 + \frac{1}{2}(S_f - S_g) \pm \sqrt{\frac{1}{4}(2m_2 + S_f + S_g)^2 + \gamma^2 b}. \quad (5.18)$$

When the estimated eigenvalues are computed for the same group of systems as in the numerical analysis Table 5.1 is generated. The results shown in this comparison demonstrate the validity of this approximation technique.

The time has come to examine these results more closely. We start with the comparison between the Dirac and the 1CS with a $\kappa=10.0$, both are the

Table 5.1: Comparison of the exact and estimated solutions for the Dirac and 1CS equations. All energies are in GeV, and the symbol – indicates that there is no stable solution.

parameters		positive energy			negative energy		
		exact	estimate		exact	estimate	
m_1/m_2	y	E_1	E	γ	E_{-1}	E	γ
Dirac							
∞	0.0	0.976	0.950	0.715	-1.249	-1.226	0.859
	0.4	1.028	1.014	0.673	-0.660	-0.650	0.463
One Channel Spectator							
10	0.0	0.964	0.946	0.635	-1.091	-1.034	0.988
	0.4	1.013	1.007	0.603	-0.619	-0.598	0.505
5	0.0	0.940	0.926	0.579	-0.936	-0.828	1.272
	0.4	0.992	0.992	0.552	-0.548	-0.532	0.563
2	0.0	0.857	0.857	0.471	-0.607	–	–
	0.4	0.928	0.952	0.452	–	–	–
1	0.0	0.745	0.777	0.379	-0.330	–	–
	0.4	0.853	0.928	0.367	–	–	–

pure scalar systems. The energy curves explored in this chapter are given in units of GeV, and are functions of the parameter γ . The pure scalar case shown in Fig. 5.3 demonstrates how the positive energy is approximately the same for both the Dirac and $\kappa=10$ systems. The $\kappa=10$ positive curve goes to infinity more rapidly than the Dirac curve while the negative curve goes much slower to negative infinity than its counterpart. The important features of this figure is that the $\kappa=10$ system is stable and how it diverges from the Dirac case.

The question now is what happens when the mass ratio changes. To do this we turn our attention to Fig. 5.4 where the energy curves of the 1CS systems for the mass ratios 10, 5, 2, and 1 are plotted. The positive energy curves indicate that as κ decreases so does the ground state energy.

For the negative curves the $\kappa=1$ and 2 systems do not possess a critical point because they continue through the zero energy boundary and become positive at high γ . This would indicate that these states have negative energies which vary with the spline rank. However, this is not seen in the numerical analysis. Instead, the instability is due to the negative energy wave functions losing their proper structure. Two factors come into play here which might explain the lack of energy variance with the spline rank. First, this is only an approximate solution which means we lose much of the

finer points of the systems. Second, the barrier tunneling occurs at high γ instead of at the low end as was seen in the previous case. In addition, the distance to tunnel through the barrier is much greater. As a result, unreasonable wave functions may be exactly how this cause of instability manifests itself.

The $\kappa=5$ curve is too close to the border line to tell whether it behaves like the ten-to-one mass ratio system or the other two cases. Of course, we do know from the numerical analysis that it is completely stable.

To see the effects of a change in the vector strength we shall examine Fig. 5.5 and Fig. 5.6 for the $\kappa=10$ and 1 systems respectively. First note that for both mass ratios the $y=0.6$ and 1.0 negative curves depict the same feature which was linked earlier to energy variance with the spline rank. These four states fail their stability analysis for exactly that reason. Next, the $y=0.4$ with a $\kappa=10$ is stable just as the pure scalar example was.

Since the pure scalar equal mass case was already covered from Fig. 5.4, this leaves only the $y=0.4$ $m_1 = m_2$ system to handle. Here we see the first example of the negative states growing until they gain positive energy eigenvalues, as shown in the numerical analysis. The only difference here (as opposed to the pure scalar case with equal mass) is that the negative curve becomes positive at lower γ . Recall that the pure scalar case had isolated

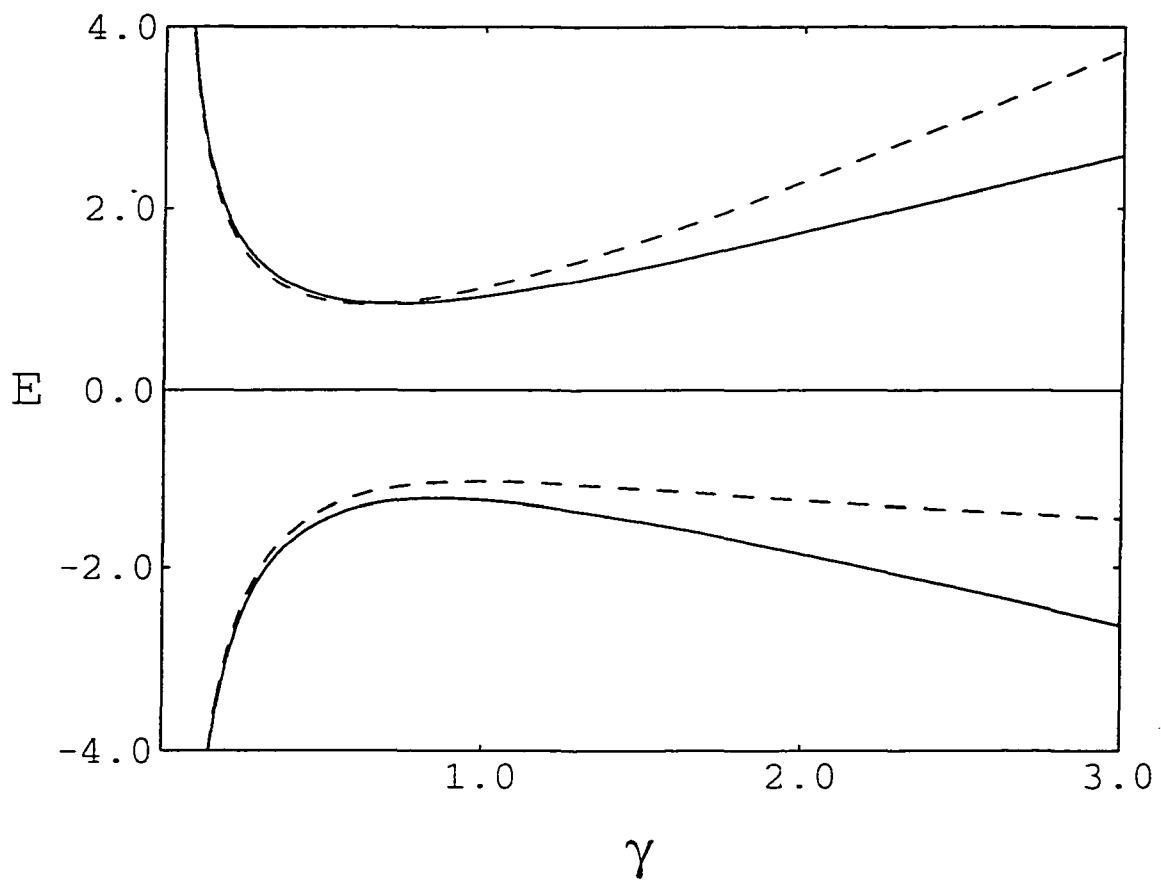


Figure 5.3: Energies $E = E_B$ as a function of the variational parameter γ for the Dirac equation (solid line) and the 1CS equation with $m_1 = 10m_2$ (dashed line). In both cases, $y = 0$.

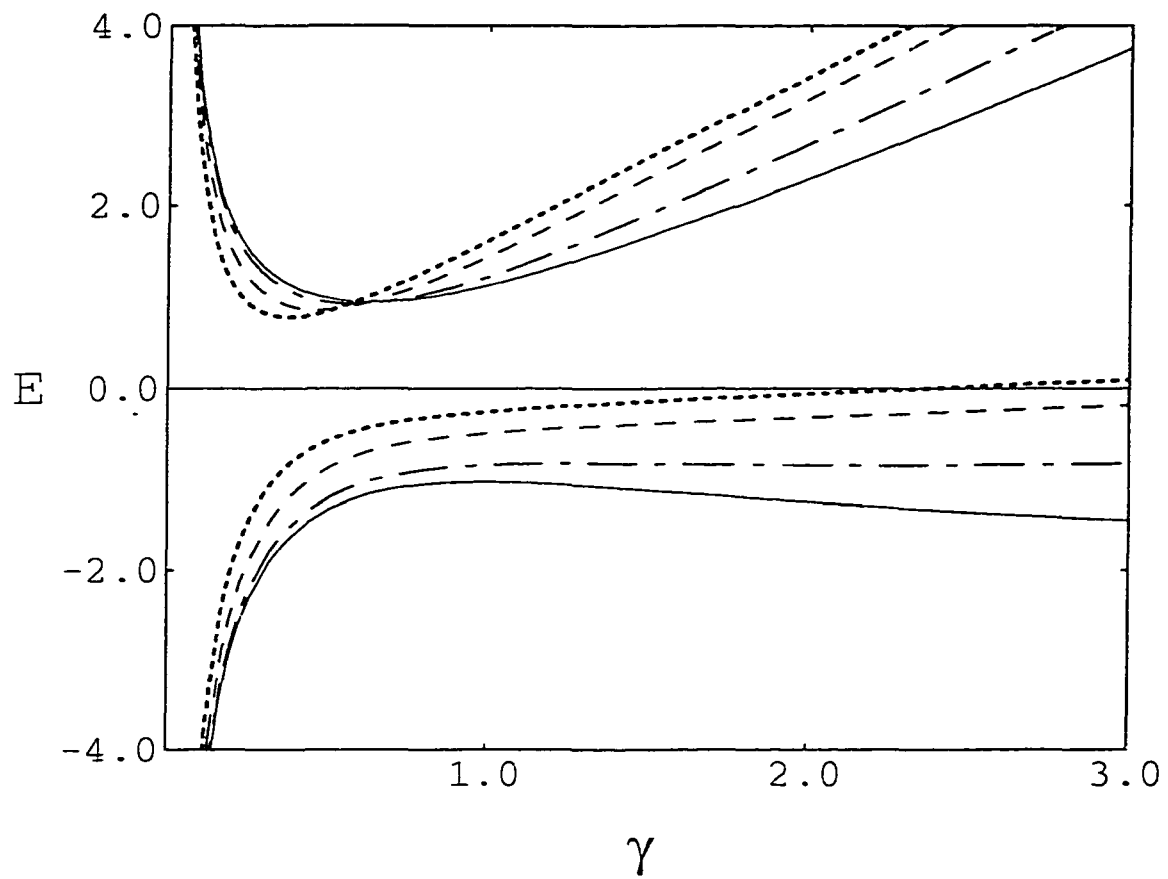


Figure 5.4: The 1CS energy $E = E_B$ as a function of the variational parameter γ for different mass ratios $\kappa = m_1/m_2 = 10$ (solid line), $\kappa = 5$ (dot-dashed), $\kappa = 2$ (dashed), and $\kappa = 1$ (dotted). In all cases, $y = 0$

stable positive states and negative unstable states due to their wave functions. Either the $y=0.4$ negative energy curves become positive early enough to allow a significantly greater amount of quantum tunneling to occur, which apparently has new consequences, or some critical feature of this curve is lost due to the technique employed to solve the system.

From the analysis of this chapter it can be concluded that the positive energy curves vary little compared to the negative curves as both the mass ratio and vector strength are varied. It is the structure of the negative curves which determines the question of stability for a system. The general conclusion from this analysis is that, when the time-like vector component is employed, the stability of a system increases as the mass ratio increases and the vector strength decreases. Which of course matches the findings from the numerical analysis. This variational-like technique does not give the accuracy of the eigenvalues, the certainty concerning stability, or the speed of analysis that the numerical analysis provides. However, it did give us a greater insight into the causes of instability.

.

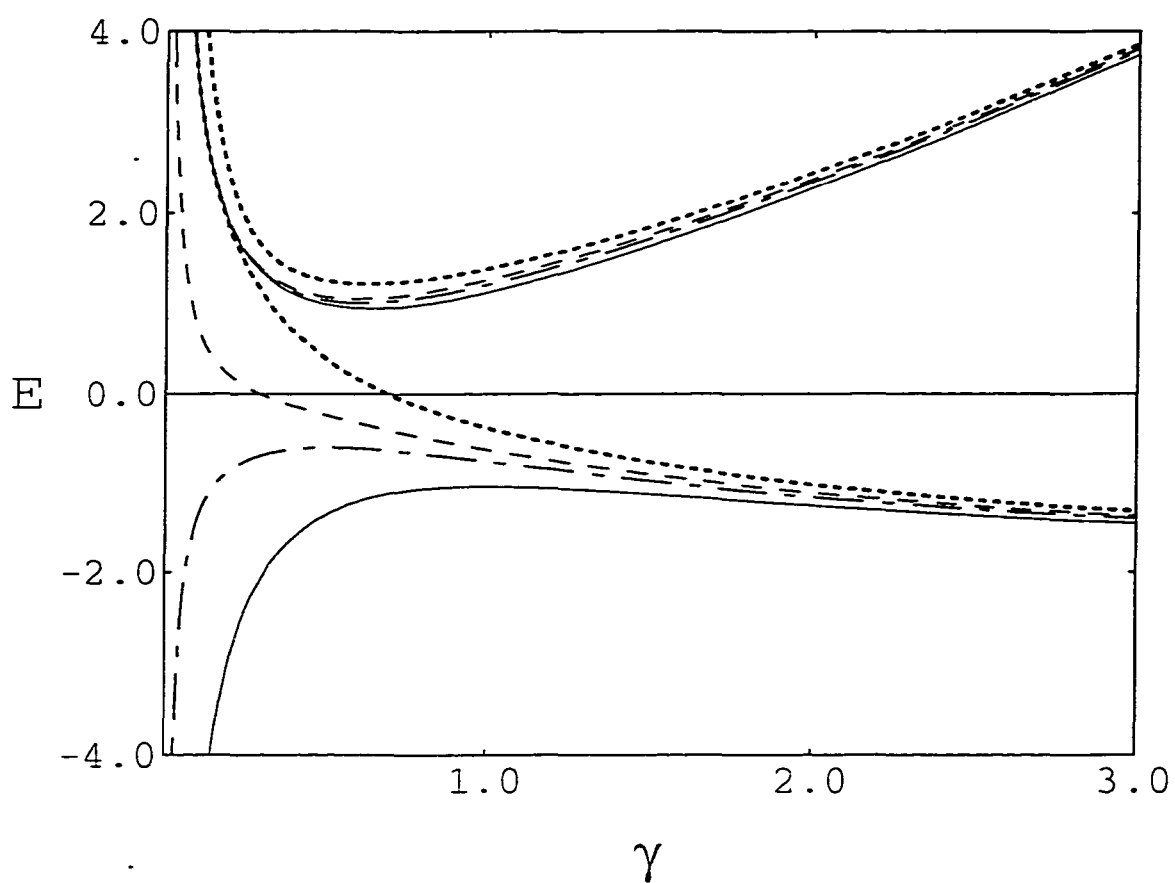


Figure 5.5: The 1CS energy $E = E_B$ as a function of the variational parameter γ for different mixing ratios $y = 0$ (solid line), $y = 0.4$ (dot-dashed), $y = 0.6$ (dashed), and $y = 1.0$ (dotted). In all cases $m_1/m_2 = 10$.

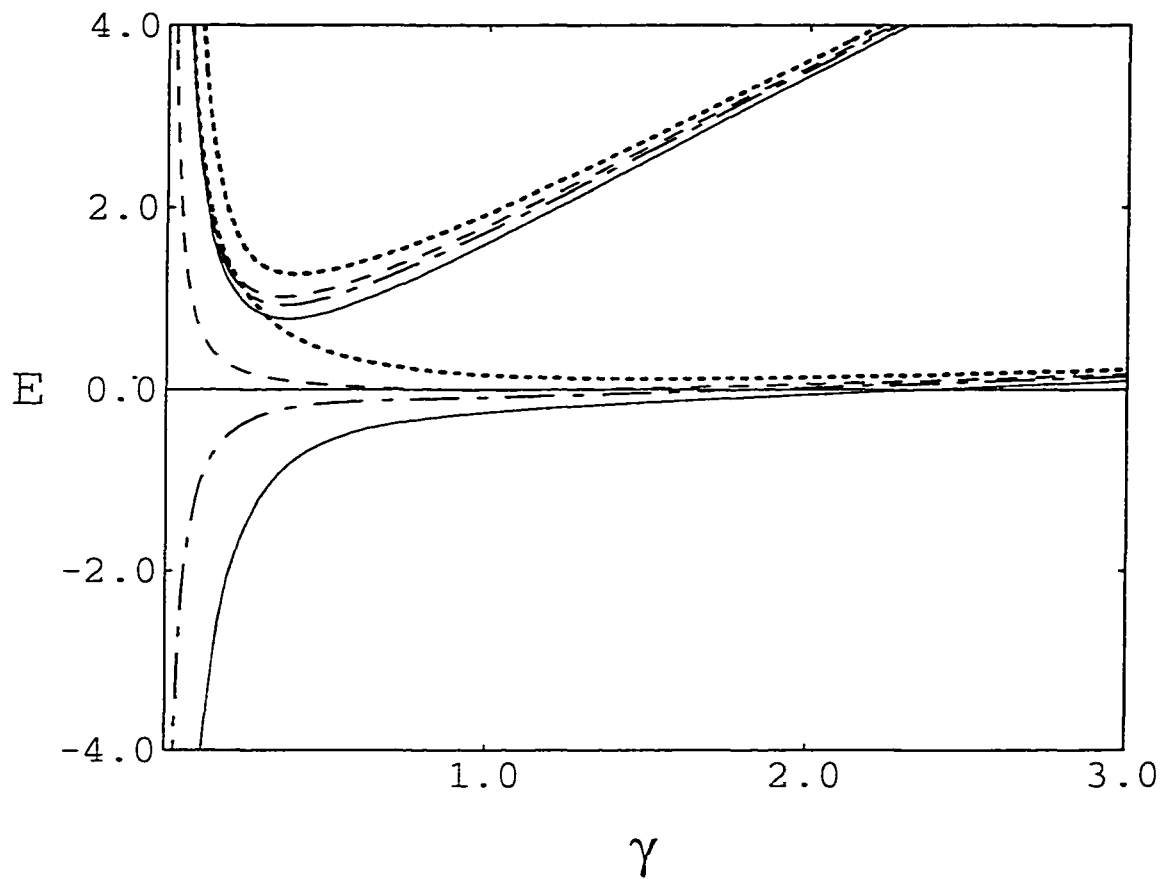


Figure 5.6: The ICS energy $E = E_B$ as a function of the variational parameter γ for different mixing ratios $y = 0$ (solid line), $y = 0.4$ (dot-dashed), $y = 0.6$ (dashed), and $y = 1.0$ (dotted). In all cases $m_1/m_2 = 1$.

Chapter 6

Conclusions

The results of the stability analysis when the time-like vector and the full four vector Lorentz structures are examined are given by Table 6.1 and Table 6.2 respectively.

- The Dirac equation is completely stable when the potential vertex Lorentz structure is scalar dominant. ($y < 1/2$).
- The one channel spectator equation with time-like vector structure γ^0 is completely stable when the mass ratio $\kappa=10$ with $y=0.0$ and 0.4 systems, or when $\kappa=5.0$ for the pure scalar system. As the mass ratio is decreased for the pure scalar system the negative energy states become unstable, as is the case when $\kappa=2.0$ and 1.0 . For the system with $y=0.4$ this happens sooner, at $\kappa=5.0$, and below this mass ratio the

Table 6.1: Stability Results for scalar versus time-like vector mixed Lorentz structures (the table lists the region of stability or the first of the four tests that the system fails).

	$y = 0.0$	$y = 0.4$	$y = 0.6$	$y = 1.0$
Dirac	stable	stable	Cond 3	Cond 2
1CS $\kappa=1.0$	positive	Cond 3	Cond 2	Cond 2
1CS $\kappa=2.0$	positive	Cond 3	Cond 2	Cond 2
1CS $\kappa=5.0$	stable	positive	Cond 2	Cond 2
1CS $\kappa=10.0$	stable	stable	Cond 2	Cond 2
Salpeter	$m \geq 0.85$	stable	stable	stable

Table 6.2: Stability Results for scalar versus full four vector mixed Lorentz structures (the table lists the region of stability or the first of the four tests that the system fails).

	$y = 0.0$	$y = 0.4$	$y = 0.6$	$y = 1.0$
1CS $\kappa=1.0$	positive	stable	Cond 2	Cond 2
1CS $\kappa=2.0$	positive	stable	Cond 2	Cond 2
1CS $\kappa=5.0$	stable	stable	Cond 2	Cond 2
1CS $\kappa=10.0$	stable	stable	Cond 2	Cond 2
Salpeter	$m \geq 0.85$	$m \geq 1.625$	unstable	unstable

systems are completely unstable. This means that the 1CS equation becomes more stable as the vector strength decreases and the mass ratio increases. In other words the equation has the proper Dirac equation limit when $y < 1/2$.

- The 1CS with full four vector structure γ^μ is completely stable for all mass ratios when the vector strength is scalar dominant, as in the case when $y=0.4$, but not pure scalar. The pure scalar case is the same as in the γ^0 analysis. For the vector dominant cases the systems are totally

unstable. When $y=0.4$ the 1CS system has the correct Dirac limit for that vector strength.

- The Salpeter equation with vector structure γ^0 and equal quark-antiquark masses are completely stable for all vector strengths except for $y=0.0$. When the pure scalar system is examined it was discovered that by increasing the quark masses the system becomes stable. Unstable states are still present in the system, however they do not affect neighboring states and may be rejected. As the masses are increased from approximately 0.85 GeV the systems become more stable, higher excited states retain their proper characteristics. Unlike the cases where the negative states of the 1CS equation were unstable, the negative states of the pure scalar systems are also stable if their positive counterparts are stable.
- The Salpeter equation with vector structure γ^μ with $m_1 = m_2$ is unstable for all vector strengths except for scalar dominant cases, such as $y=0.4$. For this vector strength the system is unstable until the quark masses are increased to approximately 1.625 GeV. The system then has the same properties as the pure scalar case explained above.

The usefulness of a system where only part of the spectrum is stable is still open to question. Others have had to deal with such partially stable systems. Through their research Tiemeijer and Tjon [20] have found such systems for the Blankenbecler-Sugar-Logunov-Tavkhelidze equation. They found that the unstable states could be isolated and removed from the systems, stability condition 3 presented in this thesis is satisfied. These remaining stable states produced good results for the meson mass spectra and the Regge trajectories. As mentioned earlier, so long as the unstable states can be isolated in the system, and energy levels you are interested in are within the remaining stable states, these partially stable states may be used with caution.

The answer to the fundamental question presented by this research has therefore been found. The stability of the linear combination of scalar and vector Lorentz structures of the confining potential directly depends on the relativistic equation used to model the meson.

The study of the spectator equation is still preliminary at this time for two reasons. First, only the 1CS equation has been studied which is invalid when the quark and antiquark masses are equal. For a bound state with equal masses the *two* channel spectator equation must be utilized after being explicitly symmetrized. Second, the study of the 1CS equation was limited to the quasirelativistic approximation, which means that retardation

is neglected. However, leaving out retardation leads to the Salpeter equation. This undermines the purpose of the LCS equation so investigation of the equation with retardation is very important. In addition, the regularization term and form factors were also left out. In order to reproduce the meson spectrum both properties must be replaced, which of course means their stability must be investigated.

The results from the Salpeter equation with a time-like vector structure agree with those found in Ref. [10]. However they disagree with the conclusions of Parramore and Piekarewicz [8]. They found the Salpeter equation to be unstable for any scalar dominant confining potential regardless of the quark mass. This is contradictory to the results we found, the $y=0.4$ was stable and the pure scalar case was stable for a high enough quark mass. To confirm these results we examined a specific case they had also looked at, $\sigma=0.29 \text{ GeV}^2$, $m=0.9 \text{ GeV}$, $y=0.0$ for a pseudoscalar system, and 25 basis states. They found such a system to be unstable, were as we found it to be partially stable and valid due to stability condition 3. One possible explanation for this discrepancy concerns the choice of basis functions. They used nonrelativistic harmonic oscillator functions, and we used cubic splines for our wave functions. While it is true that they might not consider a partially

stable system as being valid, this would not explain our different views of the system with $y=0.4$.

We have introduced four stability conditions which must be satisfied for a system to be stable. It was also determined that the stability of these relativistic equations demand the examination of the eigensystems on both an individual eigenstate level and the system as a whole. It was shown through these stability criteria that the Lorentz structure of the confining potential and the relativistic equation utilized to model the meson bound state are both critical in determining the stability of the system.

Clearly this topic requires further investigation. The ICS equation with a fully relativistic potential needs to be investigated as does the two channel spectator equation. The expansion of the potential to include a one gluon exchange would also need to be addressed. Of course the ultimate objective of this research is to properly reproduce the meson phenonema and enable predictions to be made.

Appendix A

Derivation of the Form of the Negative Energy Dirac Spinor

The purpose of this appendix is to show how $v(-\mathbf{p}, \lambda)$ is calculated, since it is not just a matter of replacing \mathbf{p} with $-\mathbf{p}$. Recall that the Lorentz transformations on the Dirac space can be written[13]

$$S(\Lambda) = e^{\frac{1}{2}\boldsymbol{\xi}\cdot\boldsymbol{\alpha} - \frac{i}{2}\boldsymbol{\gamma}^5\boldsymbol{\theta}\cdot\boldsymbol{\alpha}}, \quad (\text{A.1})$$

where $\boldsymbol{\alpha}$ are the generators of the boosts (not needed here) and $\boldsymbol{\gamma}^5\boldsymbol{\alpha}$ are the generators of rotations. The matrices $\boldsymbol{\gamma}^5\boldsymbol{\alpha}_i$ are

$$\boldsymbol{\gamma}^5\boldsymbol{\alpha}_i = \begin{pmatrix} \sigma_i & 0 \\ 0 & \sigma_i \end{pmatrix}, \quad (\text{A.2})$$

where $\sigma_i = (\sigma_1, \sigma_2, \sigma_3)$ are the Pauli matrices.

Now the u and v helicity spinors are

$$u(\mathbf{p}, \lambda_j) = N_{p_j} \begin{pmatrix} 1 \\ 2\lambda_j \bar{p}_j \end{pmatrix} \chi^{\lambda_j} \quad v(\mathbf{p}, \lambda_j) = N_{p_j} \begin{pmatrix} -2\lambda_j \bar{p}_j \\ 1 \end{pmatrix} (-i\sigma_2) \chi^{\lambda_j} \quad (\text{A.3})$$

where the χ^λ are given in Table 2.1. To transform $v(\mathbf{p}, \lambda)$ into $v(-\mathbf{p}, \lambda)$, we rotate $v(\mathbf{p}, \lambda)$ by an angle $\theta = \pi$ about the y axis (in our applications \mathbf{p} lies in the xz plane). This rotation, R_π , reduces to

$$R_\pi = \cos \pi/2 - i\gamma^5 \alpha_2 \sin \pi/2 = -i\sigma_2. \quad (\text{A.4})$$

Hence the v -spinor for $-\mathbf{p}$ becomes

$$v(-\mathbf{p}, \lambda_j) = R_\pi v(\mathbf{p}, \lambda_j) = -N_{p_j} \begin{pmatrix} -2\lambda_j \bar{p}_j \\ 1 \end{pmatrix} \chi^{\lambda_j}. \quad (\text{A.5})$$

This is the v spinor utilized in this paper; note that it has the *same* two-component spinor as u . The minus sign is a phase factor which has no effect on the results.

Appendix B

Spectator Equation in the Limit when $m_1 \rightarrow \infty$

In this Appendix we will derive the Dirac equation from the single channel spectator equation by taking the mass of the quark, m_1 , to infinity. The Dirac equation we obtain then describes an antiquark in the presence of a potential generated by the heavy quark. The same equation was obtained from first principles in Chapter 2 and we will see that the result obtained in this way is identical.

The spectator equation describes two particles interacting with one another, while the Dirac equation describes a single particle interacting with a potential. In order to reduce the two-body system to a one-body system, the

mass of the quark must be taken to be extremely large compared to the anti-quark. Taking the quark (particle 1) mass to infinity will cause it to behave as a simple potential source. Evidence that this source is actually caused by another fermion will follow from the helicity properties of the effective potential. It should be noted that taking the quark mass to be large is not arbitrary. In Fig. 3.2 we chose to close the contour in the lower half plane, thereby placing the *quark* on its positive energy mass shell (this choice is appropriate only if $m_1 \geq m_2$). Since the $m \rightarrow \infty$ limit corresponds physically to removing a particle from the influence of the interaction, which includes putting it on its mass shell, it is the quark mass which must be set to infinity in this case.

Taking the $m_1 \rightarrow \infty$ limit will lead to $\tilde{p}_1 \rightarrow 0$, $\tilde{k}_1 \rightarrow 0$, $E_{p_1} \rightarrow m_1$, and $E_{k_1} \rightarrow m_1$. The quantities given in Eq. (3.17) reduce to

$$\begin{aligned} Q &\rightarrow 1 & T_2 &\rightarrow \tilde{k}_2 & S_2 &\rightarrow \tilde{p}_2 \\ R &\rightarrow \tilde{p}_2 \tilde{k}_2 & N_{p_1} &\rightarrow \sqrt{2m_1} \end{aligned} \quad . \quad (\text{B.1})$$

As $m_1 \rightarrow \infty$, the mass of the bound state also approaches infinity [Eq. (3.25)], but so does the kinetic energy of particle one, $E_{p_1} \rightarrow m_1 \rightarrow \infty$. Cancelling out the m_1 terms the system is now solved for the binding energy. Assuming the wave functions are finite as $m_1 \rightarrow \infty$ and inserting the identities of

Eq. (B.1) into Eq. (3.16) generates the following set of coupled equations

$$\begin{pmatrix} (E_B - E_p)\psi_{1a}(p) \\ (E_B + E_p)\psi_{1b}(p) \end{pmatrix} = - \int_{\bar{k}} \frac{V_{11} N_p N_k}{2\sqrt{E_p E_k}} \begin{pmatrix} (\mp 1 + \bar{k}\bar{p} \cos \theta) & (\mp \bar{k} - \bar{p} \cos \theta) \\ (\mp \bar{p} - \bar{k} \cos \theta) & (\mp \bar{k}\bar{p} + \cos \theta) \end{pmatrix} \begin{pmatrix} \psi_{1a}(k) \\ \psi_{1b}(k) \end{pmatrix}. \quad (\text{B.2})$$

Since all terms above are with regards to particle 2 the subscript has been dropped. This is exactly the same equation as found through direct derivation of the Dirac equation.

Appendix C

Definition of the Spline Function

The solution to the wave functions used in this paper are based on a set of third order polynomial functions called cubic splines. Used previously in papers such as Ref. [16], they have proven versatile enough to model all of the wave functions examined in this paper. The definition of the wave function is

$$\psi_i(p) = \sum_{j=1}^{SN} \alpha_{ij} \beta_j(p) \quad (\text{C.1})$$

where SN is the spline rank, β is the spline function, and α is the eigenvector which is solved for along with the eigenvalues. A spline rank of 20 was chosen as the standard which means that 20 spline curves are added together to

model a given wave function structure. Each of these spline curves is defined according to four separate functions listed below. The function or functions used depends on the argument and the spline index j . The spline indices goes from 1 to SN and while the sum over all spline index is taken to define the wave function, each spline curve j is defined seperately.

$$4\beta_j(x) = \begin{cases} \frac{(x-x_{j-2})^3}{h^3}, & x \in [x_{j-2}, x_{j-1}] \\ 1 + 3\frac{(x-x_{j-1})}{h} + 3\frac{(x-x_{j-1})^2}{h^2} - 3\frac{(x-x_{j-1})^3}{h^3}, & x \in [x_{j-1}, x_j] \\ 1 + 3\frac{(x_{j+1}-x)}{h} + 3\frac{(x_{j+1}-x)^2}{h^2} - 3\frac{(x_{j+1}-x)^3}{h^3}, & x \in [x_j, x_{j+1}] \\ \frac{(x_{j+2}-x)^3}{h^3}, & x \in [x_{j+1}, x_{j+2}] \\ 0 & \text{otherwise.} \end{cases} \quad (\text{C.2})$$

The argument of the splines ranges from zero to one. This range is divided into sectors whose size, $h = 1/(SN + 1)$, depends on the spline rank chosen. Each sector is defined by nodes, x_j , with the number of nodes equal to $SN + 2$. The first node is always located at zero, called x_1 , and the last at one, called x_{SN+2} . An example of the spline curves for a spline rank of 4 is given in Fig. C.1. None of the nodes are labeled less than 1 so for $j = 1$ the first sector is defined by the third function of Eq. (C.2). The first sector of $j = 2$ is a special case, and is defined as the second function with node x_1 plus the fourth function with node x_2 .

Now some important points must be addressed. First, the value of the spline function of one sector matches that of the next function in any adjoining sector at the node. However, these values do not match up for all orders of differentiation of the functions. Therefore, in order to obtain convergence the integrals must be divided into pieces, between the nodes and then summed up afterwards. Special care must be used since the numerical integration is accomplished by Gaussian quadrature. For the double integral of the potential the subintegral which possesses the pole must be split in two. Now the pole can be isolated such that an equal spacing on either side of it is present. This is an essential concept when numerically integrating, since convergence is found by approaching the pole from both sides but never reaching it. The remainder of the subintegral is then handled alone and added to the first piece.

The second point is that the spline argument ranges from zero to one, however, the integrals go from zero to infinity. The versatility of specifying the wave function identity is utilized to overcome this. A subroutine is used to generate Gauss points from zero to one along with the corresponding weights. These values are then tangent mapped so that the range now extends to the limit of infinity. Essentially, the argument of the spline is defined as the

inverse tangent of the momentum. In other words,

$$x = \frac{2}{\pi} \arctan(p). \quad (\text{C.3})$$

The result of this mapping is shown in Fig. C.2.

When the spline rank is increased the sectors become smaller resulting in a higher density of spline curves for a set range. This also means that the distance in momentum space the last spline curve reaches before leveling out to zero increases. Thus, a more accurate modeling of the actual wave function curve is obtained. Of course this higher precision must be balanced by consideration of computation time.

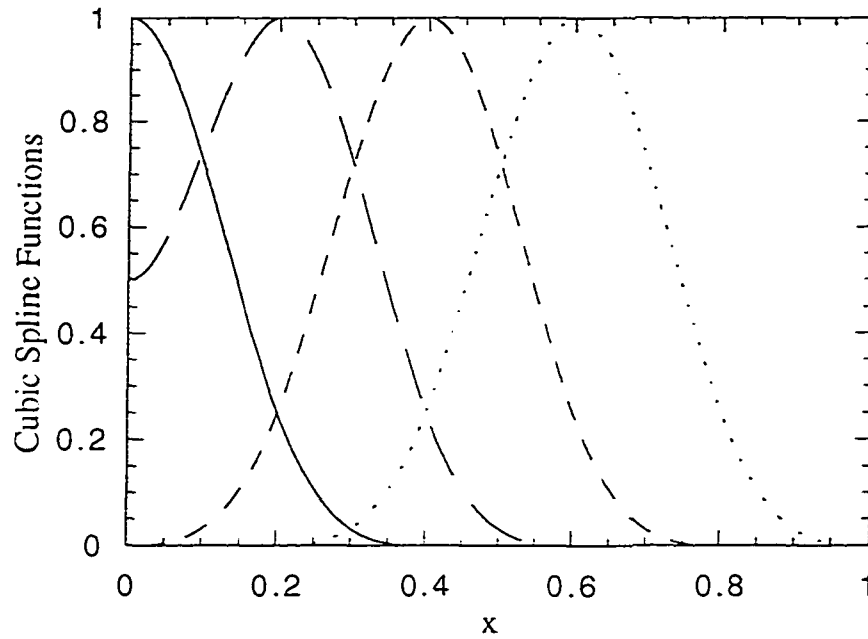


Figure C.1: Spline Rank 4 Curves (Index 1 Solid, 2 Long Dash, 3 Short Dash, and 4 Dot).

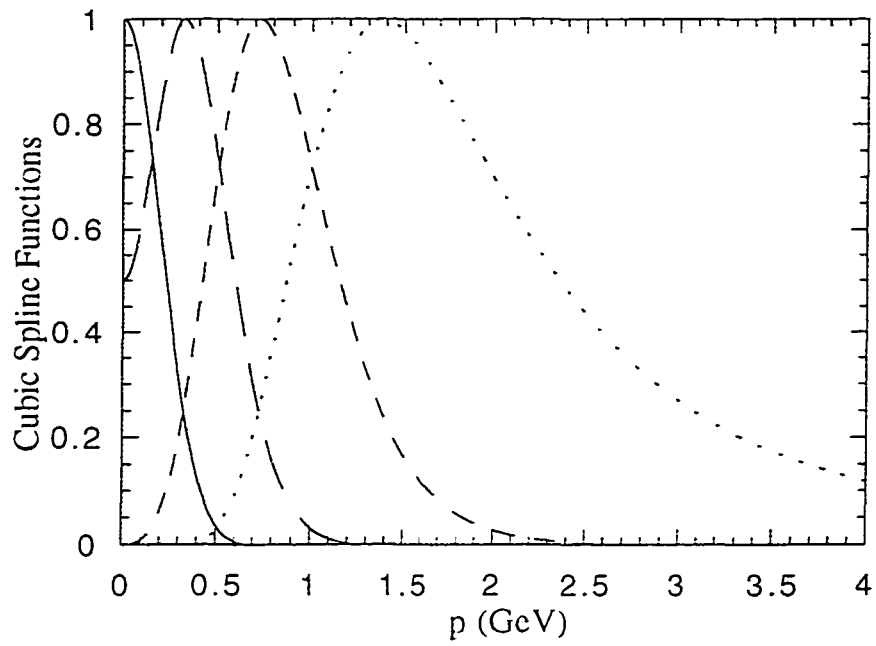


Figure C.2: Spline Rank 4 Curves (Index 1 Solid, 2 Long Dash, 3 Short Dash, and 4 Dot) with Momentum Argument.

Appendix D

Momentum Space Wave

Function Structures

The fourth stability condition says the structure of the wave function must be correct for the specific state being considered. The question is, how do we know what the appropriate structure should be? One argument points out the fact that certain structures keep reappearing for specific energy states which have already passed the first three stability conditions. These wave functions are what one would expect from a position space solution. They have the correct number of nodes and behavior for the specific energy level wave function. In addition, their structures vary little when the spline rank is changed.

The problem is that these solutions are in momentum space, not position space. Another issue is the fact that other papers which deal with stability do not have such wave function structures for their stable solutions, for example Ref. [20]. It is therefore necessary to confirm our conclusions concerning what stable momentum space wave functions should look like.

The best way to determine what the structure of stable momentum space wave functions are, is to return to the basics. The equation for a non-relativistic linear potential is

$$-\frac{\hbar^2}{2M} \frac{d^2\psi(x)}{dx^2} + \sigma x\psi(x) = E\psi(x). \quad (\text{D.1})$$

This is the one-dimensional *Schrödinger* equation in position space. The solutions to this system, detailed in Ref [21], are the Airy functions. Because this is a non-relativistic system there are no negative energy states, however we can examine the ground and excited states with positive energy. By conducting a Fourier transform, the momentum space wave functions for the ground, first, and second excited states can be found, Fig. D.1 to Fig. D.3 respectively.

This is more than enough to determine the correct wave function structure, however, let us add one more component to this investigation. The system can be solved directly in momentum space using cubic splines to

model the solutions. The *Schrödinger* equation in momentum space is

$$\frac{1}{2}p_0^2\psi(p_0) - E_0\psi(p_0) = 8\pi\sigma_0 \int \frac{d^3k_0}{(2\pi)^3} \frac{\psi(k_0) - \psi(p_0)}{(\vec{p}_0 - \vec{k}_0)^4}, \quad (\text{D.2})$$

where the terms with the subscript naught have been rescaled by the reduced mass. For a complete account of this three-dimensional linear potential equation see Ref. [15].

The ground, first, and second excited states resulting from Eq. D.2 are shown in Fig. D.1 to Fig. D.3 respectively along with their Fourier transformed Airy solution counterparts. This is confirmed by the close agreement between the solutions derived from the Airy versus spline functions. The energy levels found for the Airy, spline rank 20, and spline rank 16 cases are given in the caption of the appropriate figure. Their agreement, and that of the momentum space wave functions, confirm the validity of using splines to model the solutions for a confining potential. They also validate our conclusions concerning the expected structure of stable momentum space wave functions. The figures shown in this study demonstrate the same characteristics as those deemed stable in the quasi-relativistic stability analysis.

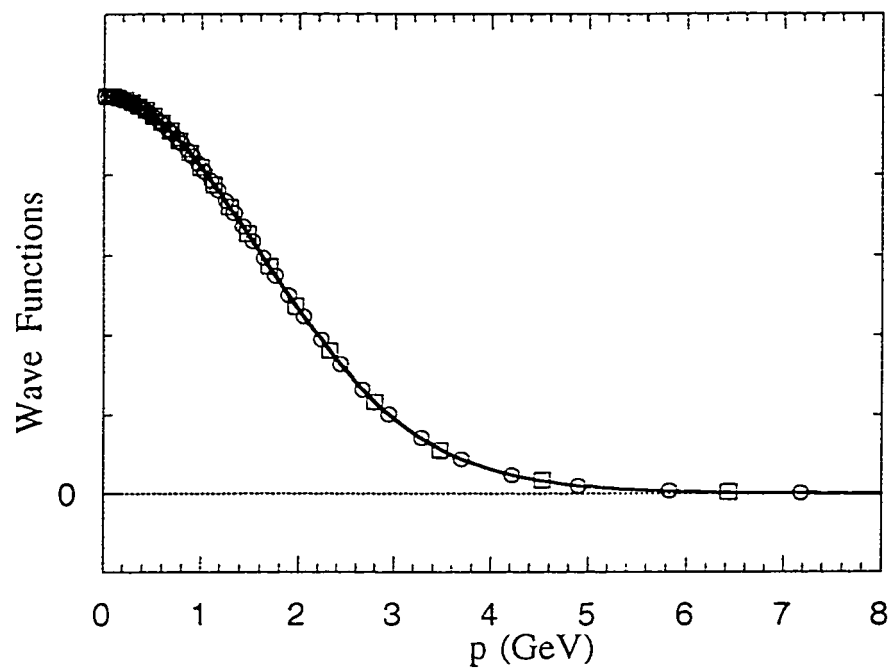


Figure D.1: Non-Relativistic linear potential ground state wave functions, Airy solution $E_1=6.483$ GeV (Solid Line), Spline Rank 20 $E_1=6.485$ GeV (Circle), Spline Rank 16 $E_1=6.486$ (Square).

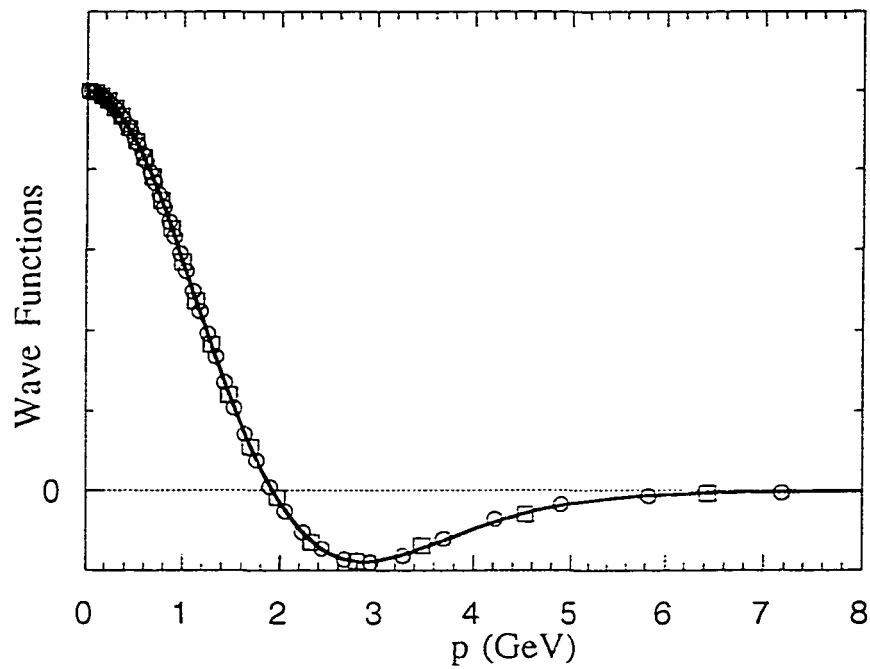


Figure D.2: Non-Relativistic linear potential first excited state wave functions, Airy solution $E_2=11.337$ GeV (Solid Line), Spline Rank 20 $E_2=11.356$ GeV (Circle), Spline Rank 16 $E_2=11.355$ (Square).

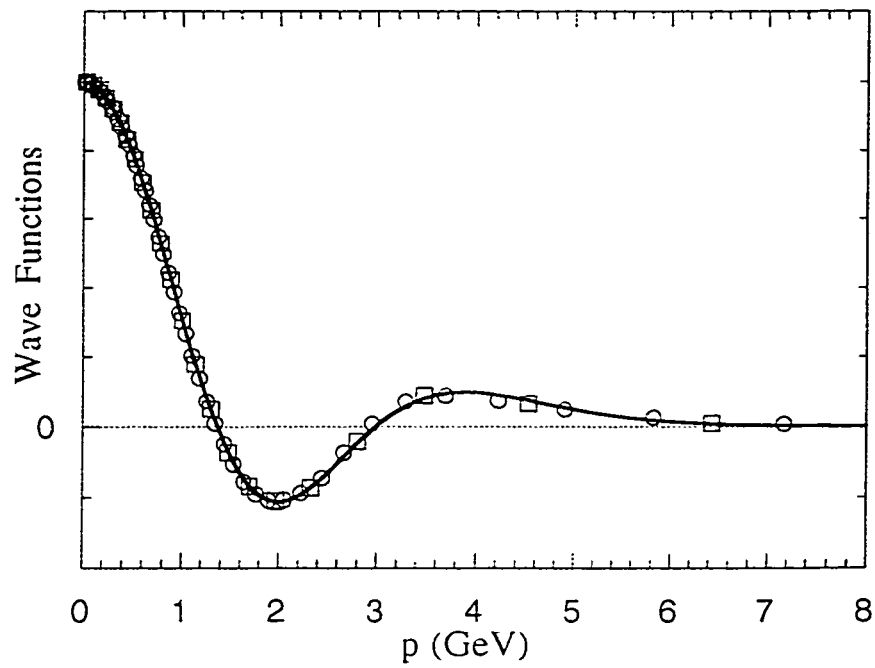


Figure D.3: Non-Relativistic linear potential second excited state wave functions, Airy solution $E_3=15.309$ GeV (Solid Line), Spline Rank 20 $E_3=15.464$ GeV (Circle), Spline Rank 16 $E_3=15.341$ (Square).

References

- [1] R. Eisberg and R. Resnick. *Quantum Physics of Atoms, Molecules, Solids, Nuclei, and Particles* (John Wiley and Sons, Inc., New York, 1974).
- [2] S. Schweber, H. Bethe, and F. de Hoffmann. *Mesons and Fields Volume I Fields* (Row, Peterson, and Company, New York, 1956).
- [3] C. Lattes, C. Occhialini, and C. Powell. *Nature*, **160**, 453, 486 (1947).
- [4] F. Halzen and A. Martin, *Quarks and Leptons: An Introductory Course in Modern Particle Physics* (John Wiley and Sons, New York, 1984).
- [5] S. Godfrey and N. Isgur, *Phys. Rev. D.* **32**. 189 (1985).
- [6] D. Gromes. Institut für Theoretische Physik. Fed. Rep. Germany. Nov. 3, 1987.

- [7] J. L. Lagaë, Service de Physique Théorique, Université Libre de Bruxelles, Belgium, Jan. 26, 1990.
- [8] J. Parramore and J. Piekarewicz, Nucl. Phys. A **585**, 705 (1995).
- [9] S. Wallace, C. Bell, M. Ortalano, and R. Thayyullathil, submitted paper for publication at this time.
- [10] J. Resag, C. R. Münz, B. C. Metsch, and H. R. Petry, Nuclear Physics A **A578**, 397 (1994); C. R. Münz, J. Resag, B. C. Metsch, and H. R. Petry, Nuclear Physics A **A578**, 418 (1994).
- [11] J. D. Bjorken and S. D. Drell. *Relativistic Quantum Mechanics* (McGraw-Hill Inc., New York, 1964).
- [12] E. E. Salpeter and H. A. Bethe, Phys. Rev. **84**, 1232 (1951).
- [13] F. Gross, *Relativistic Quantum Mechanics and Field Theory* (John Wiley and Sons Inc., New York, 1993).
- [14] F. Gross, J. W. Van Orden, and K. Holinde, Phys. Rev. C **45**, 2094 (1992).
- [15] F. Gross and J. Milana. Phys. Rev. D **43**, 2401 (1991).
- [16] F. Gross and J. Milana, Phys. Rev. D **50**, 3332 (1994).

- [17] E. E. Salpeter, *Phys. Rev.* **87**, 328 (1952).
- [18] F. Gross, *Phys. Rev.* **186**, 1448 (1969).
- [19] M. Uzzo and F. Gross, submitted paper to *Phys. Rev. C*.
- [20] P. C. Tiemeijer and J. A. Tjon, *Phys. Rev. C* **49**, 494 (1994).
- [21] R. Winter, *Quantum Physics* (Faculty Publishing, Inc., California, 1986).

.

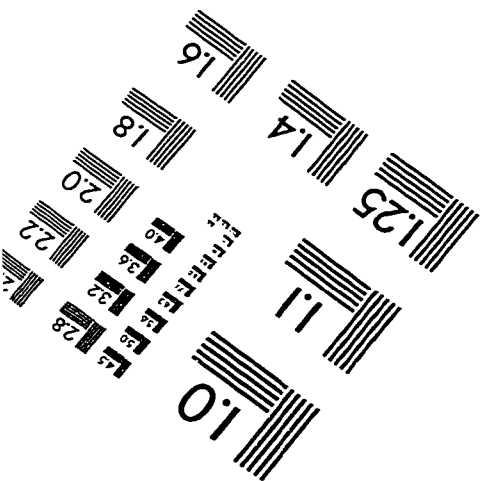
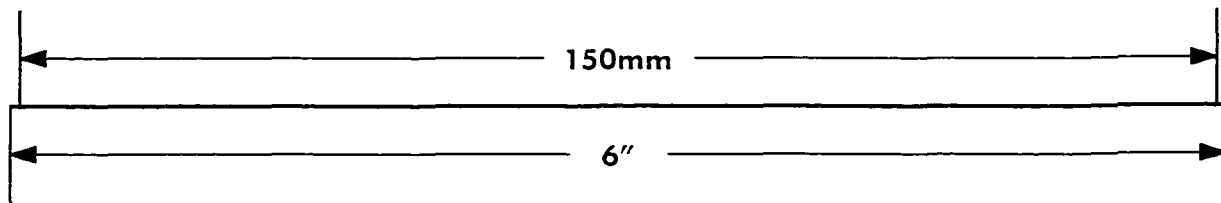
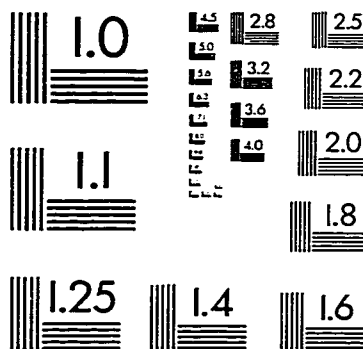
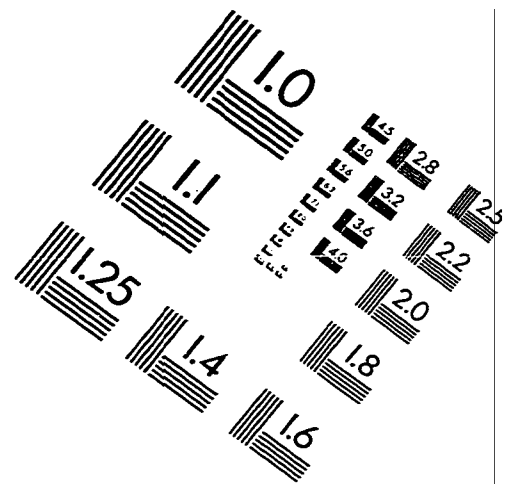
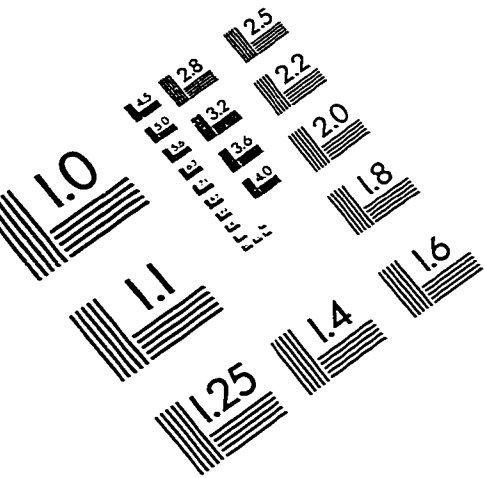
.

VITA

Michael Uzzo

Michael Uzzo was born in The Bronx, New York on January 6, 1970. He attended Salesian High School in New Rochelle, New York. He then attended Manhattan College, in Riverdale, New York, where he was a member of the Epsilon Sigma Pi Honor Society. He received his B. S. in physics in May of 1992, graduating Cum Laude. He began graduate studies at the College of William and Mary in Williamsburg, Virginia in August of 1992. He received his M. S. in Physics in May 1994, and anticipates receiving the Ph. D. in 1998.

IMAGE EVALUATION TEST TARGET (QA-3)



APPLIED IMAGE, Inc
 1653 East Main Street
 Rochester, NY 14609 USA
 Phone: 716/482-0300
 Fax: 716/288-5989

© 1993, Applied Image, Inc., All Rights Reserved

